A study of dynamics in microscopic systems using optical tweezers: dynamical stabilisation, cell stretching and thermal fluctuations

Thomas James Smart

Thesis submitted for the degree of
Doctor of Philosophy

Department of Physics & Astronomy
University College London (UCL)
November 2017

Declaration

I, Thomas James Smart, confirm that the work presented in this thesis is my own. Where information has been derived from other sources, I confirm that this has been indicated in the thesis.

Thomas James Smart .....

Abstract

This thesis presents an investigation into the dynamics of three distinct microscopic systems: dynamical stabilisation in a finitely-rigid over-damped microscopic pendulum; deformability in red blood cells; and thermodynamic fluctuations in a system of hydrodynamically coupled colloidal particles. Each system is studied using optical tweezers.

Part I provides an introduction to the development and operation of optical tweezers and gives an overview of the particle dynamics concepts that are built upon later in the thesis.

Part II contains the work on dynamical stabilisation. The starting point for this work is the well-known Kapitza pendulum: a rigid pendulum whose suspension point is oscillated in such a way that the pendulum becomes stable in the upright position. Here I consider a pendulum that is finitely rigidity (i.e. a pendulum that is not mathematically infinitely rigid) and subjected to heavy damping. I present a model based on a scanning time-averaged ring-shaped optical trap in which a colloidal particle is trapped. The pendulum is localised by viscous fluid flow and oscillated by modulation of the ring-centre. A mathematical treatment of the model reveals a regime in which the pendulum explores different stability positions based on the modulation amplitude and frequency. These predictions are tested in simulations and experiments.

In part III optical tweezers are used to stretch red blood cells (RBCs) in order to measure their deformability. The measured deformability of RBCs from patients suffering from diabetic retinopathy is measured and compared to the deformability of RBCs from healthy patients to investigate a link between DR and reduced RBC deformability.

Finally, in part IV an investigation into the fluctuations of work applied to a hydrodynamically coupled system is presented. In a thermodynamically noisy system, the heat and work do not have exact values. Rather, they are represented by a probability distribution. Here, I present simulations and experiments that aim to measure the work distribution in a system consisting of two colloidal particles that are coupled by their aqueous environment.

Publications

Peer-reviewed Journal Articles

- C. J. Richards*, **T. J. Smart***, P. H. Jones and D. Cubero, 'Kapitza's pendulum at the micrometre scale', *Manuscript under review.* *Authors contributed equally to this manuscript.

- R. Agrawal, **T. Smart**, J. Nobre-Cardoso, C. Richards, A. Tufail, D. Shima, P. H. Jones and C. Pavesio, 'Assessment of red blood cell deformability in type 2 diabetes mellitus and diabetic retinopathy by dual optical tweezers stretching technique', *Scientific Reports*, 6(15873), 2016.

Conference proceedings

- P. H. Jones, **T. J. Smart**, C. J. Richards and Cubero, D. 'Optical kapitza pendulum', *Proc. SPIE*, 9922(992202), 2016.

- C. J. Richards, **T. J. Smart**, P. H. Jones and Cubero, D. 'Low frequency dynamical stabilisation in optical tweezers', *Proc. SPIE*, 9548(954820), 2015.

- **T. J. Smart**, C. J. Richards, X. Han, S. Siwiak-Jaszek and P. H. Jones, 'Correlated fluctuations of optically trapped particles, *Proc. SPIE*, 9548(954823), 2015.

- **T. J. Smart**, C. J. Richards, R. Bhatnagar, R. Pavesio, R. Agrawal and P. H. Jones, 'A study of red blood cell deformability in diabetic retinopathy using optical tweezers', *Proc. SPIE*, 9548(954825), 2015.

- P. H. Jones, C. J. Richards, **T. J. Smart** and D. Cubero, 'Dynamical stabilisation in optical tweezers', *Proc. SPIE*, 9378(9370L),2015.

Acknowledgements

I would like to thank my doctoral supervisor Professor Philip Jones for the patient guidance that he has offered me during the completion of this work. I would also like to thank Christopher Richards, with whom I spent many hours working in the laboratory, for his help and friendship. My thanks must also go to all those with whom I have collaborated in this work. In particular to Dr Rupesh Agrawal, whose tenacity ensured the progress of the work on red blood cells in part III of this thesis, and to Dr David Cubero, who provided the theoretical framework for the work on dynamical stabilisation in part II. I would finally like to thank my family and girlfriend, Elinor, for their endless support and encouragement.

Contents

List of Figures

List of Tables

Listings

Part I

Introduction

Chapter 1

Optical Tweezers

1.1 Historical background

A single-beam optical trap, or an 'optical tweezers' (the terms optical tweezers and optical trap will be used interchangeably in this thesis), utilises light's momentum to non-invasively trap and manipulate microscopic objects in three-dimensions. The fact that light carries momentum, and thus exerts a pressure on any surface exposed to it, was predicted by Maxwell in 1873 [2]. The effect was experimentally verified in 1901 using thermal light sources and torsion balances [3]. The force exerted by light is minuscule and has a very limited effect on the macroscale objects of everyday life. With the development of the laser in the middle of the twentieth century, however, it became possible to focus light into very small volumes, where these optical forces are of sufficient magnitude to impart motion to micrometre-sized objects. It was this advancement in technology that led to the invention of optical tweezers.

Optical tweezers were devised and developed in a series of seminal papers by Arthur Ashkin and co-workers at the Bell Laboratories in the USA. Ashkin's original paper demonstrated that the force generated by a single focussed laser could be used to displace a micron-sized latex sphere suspended in water [4]. Ashkin wrote that particles were drawn towards the axis of the beam and accelerated along it. In the same paper, he showed that two counter-propagating laser beams could be used to trap a sphere at the point at which the radiation forces of the two lasers balanced. The following year, Ashkin demonstrated that a single, vertically-directed

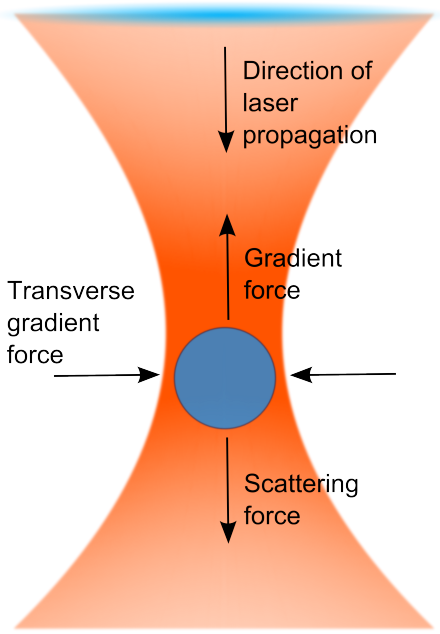

Figure 1.1: Illustration of a particle trapped close to the waist of a focussed laser beam. The 'gradient force' in the beam works against the scattering force of the photons to constrain the particle in three dimensions.

laser could be used to trap a particle if the radiation force of the laser was balanced by the downward force of gravity (optical levitation) [5]. Later, in 1986, Ashkin and colleagues succeeded in creating an 'all-optical' single beam trap [6]. Their breakthrough realisation was that the 'gradient force' in the beam (the force that drew particles towards the axis) could actually be used to constrain the particle in three dimensions. If the laser was focussed very sharply the gradient force would produce a substantial net backward force that would balance the forward-directed radiation force of the laser. Ashkin showed how this gives rise to a particle becaming trapped close to the focal point of the beam, see figure 1.1.

1.2 Typical optical tweezers set-up

A schematic diagram of a simple optical tweezers set-up is shown in figure 1.2. The trap is generated by focussing a laser beam to a diffraction-limited spot using a high-numerical-aperture objective lens. Placed before the objective lens are a pair of telescoping lenses positioned to expand the beam in such a way that the back aperture of the objective is overfilled. Overfilling of the objective is usually a

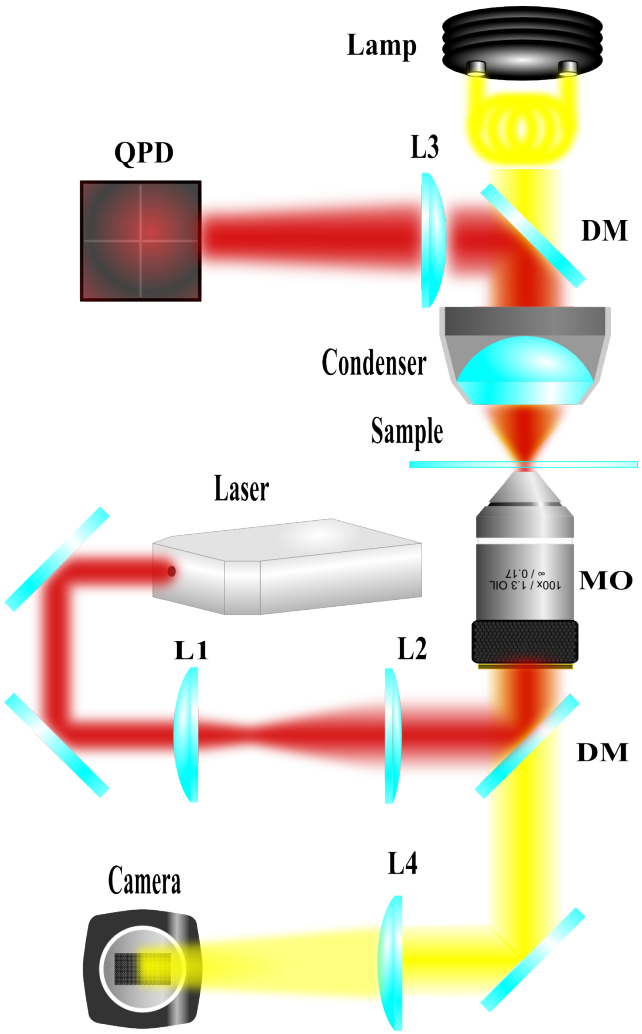

Figure 1.2: Typical optical tweezers set-up. A laser is expanded by a pair of telescoping lenses (L1 & L2) to overfill the back aperture of a high-numerical-aperture microscope objective (MO). The objective lens focusses the beam to a diffraction limited spot at the focal plane, where the sample is place. Laser light forward-scattered from the sample is reflected from a dichroic mirror (DM) and focussed (lens L3) onto a quadrant photo-diode (QPD), which is used to track the trapped particle's position. The sample is illuminated and the same objective used to focus the laser is used, in conjunction with lens L4, to image the sample onto a camera.

requirement of a stable trap. A ray focussed from a large angle contributes more to the trapping efficiency of a beam, compared to a beam focussed from a lesser angle. Overfilling the aperture increases the number of rays hitting the aperture at large angles, thus helping to ensure that stable trapping is achieved both transversely and axially in the beam.

The sample, which is typically contained within a microfluidic chamber with a volume on the order of tens of microlitres, is placed in the plane containing the beam waist of the laser. In the experiments discussed below, a bright-field illumination scheme is implemented. Light from a lamp is collected by a condenser lens and focussed onto the sample. The objective lens that focusses the trapping laser also serves to magnifying the image of the trapped object. The magnified image can then be focussed (by lens L4 in figure 1.2) onto a camera to allow visualisation of the sample.

It is very useful to be able to monitor the position of a trapped object. For example, one might want to calibrate the harmonic potential created by the optical tweezers. In order to do so, it is vital that one is able to monitor the position fluctuations of the particle. Two commonly used position detection methods when working with optical tweezers are video microscopy and optical interferometry. Video microscopy involves frame-by-frame image analysis of videos recorded on a digital camera. This may be done on the fly or as a post-experimental procedure. Optical interferometry involves the use of a photodetector, such as a quadrant photo-diode (QPD), as seen in figure 1.2. The forward-scattered light, either from the trapping beam or a probe beam, is imaged onto the QPD and the intensity distribution on the sensor is analysed to yield three-dimensional position information. Interferometry tracking techniques are generally more precise than video microscopy and are able work at very high speeds (up to several MHz). However, video microscopy is far more convenient if one is interested in tracking multiple particles simultaneously or if the position of the trap(s) moves significantly during an experiment.

The choice of trapping laser is an important consideration. The power of the laser should be sufficient to generate a trap of an appropriate stiffness (see section 2.3) for the planned experiments. A laser with a power of between 10 and 100 mW is usually

sufficient [7]. When considering the wavelength of the laser it is necessary to consider the possibility of causing photodamage to the sample, especially biological samples [8, 9]. The potential damage to a biological specimen may be readily appreciated by considering that a 100mW laser focussed to a diffraction-limited spot has an intensity close to $10^7 \mathrm{W} \cdot \mathrm{cm}^{-2}$. The effects of photodamage may be reduced by selecting a laser wavelength close to a minimum in the absorption coefficient of water. For this reason it is common to select a laser with wavelength in the near-infrared.

1.3 Applications and advances in optical tweezers

Since their introduction to the scientific community [6], optical tweezers have proven a versatile tool for probing the micro- and nano-scale world. In this section I give some examples of the way optical tweezers have been used in experiments.

The inherently small forces and length-scales associated with optical tweezers make them an ideal tool for investigations in molecular and cell biology. Ashkin immediately saw the potential for the application of optical tweezers to biological particles, publishing two papers in 1987 that described the trapping of cells, viruses and bacteria [8, 10]. Since then optical tweezers have, for example, been used to observe the action of the stepping motors kinesin [11] and myosin [12, 13], to measure the force required to stretch DNA [14], the transcription velocity of RNA [15], and to probe the mechanisms of cellular adhesion [16]. Many of these experiments use optical tweezers as a type of force microscope. Given the elastic restoring force of optical tweezers, it is possible to find the force acting on a trapped object by simply multiplying the displacement of the object by the known trap stiffness. For example, in reference [12] the ends of an actin filament were attached to two beads, each held in optical tweezers. The filament was brought close to a third bead anchored to a surface and coated in myosin. Myosin binds to actin and translocates in a step-like manner along it. This caused the trapped beads to be displaced from their equilibrium position and the magnitude of their displacement was used to determine the force generated by each step of the myosin.

Optical tweezers allow colloidal particles to be positioned and held in close prox-

imity to one another, allowing observation of the interaction between the particles. This has meant that optical tweezers have been used extensively in colloidal science experiments. For example, in 1999 Meiners and Quake [1] carried out an experiment to probe the hydrodynamic interaction between two aqueously-suspended colloidal particles held in individual optical tweezers, in which they were able to show that the particles' position fluctuations were anti-correlated at short times. With advances in holographic beam shaping [17, 18] it has been possible to create arrays of traps, in which hydrodynamic coupling can be investigated in more complex geometries, e.g. [19, 20, 21]. Beam shaping has also led to the application of beams that carry orbital angular momentum in optical trapping [22], which enables one to impart angular momentum to trapped objects, causing them to rotate [23].

Optically trapped colloidal particles, whose dynamics are determined by a combination of deterministic trapping forces and a noisy background due to Brownian motion, prove an ideal environment for the study of concepts in thermodynamics and statistical mechanics. For example, McCann et al. [24] used a pair of optical tweezers to create a double well potential for a colloidal particle, with which they experimentally verified Kramer's escape rate theorem [25]. Berut et al. [26] used a modulated double well potential to provide experimental verification of Landauer's principle [27] which links information and heat production, and Wang et al. [28] used a single trap to drag a particle through its viscous surroundings and used the measured trajectories to provide experimental proof for the fluctuation theorem [29].

Chapter 2

Optical Forces

2.1 Introduction

The essential component of an optical tweezers experiment is a tightly-focused laser beam. The beam will exert a force on an object placed in its path via two components, known as the *scattering* force and the *gradient* force. The effect of the scattering force is to push the object in the direction of the beam's propagation, whilst the gradient force pulls the object toward the region of highest intensity in the beam (so long as the refractive index of the medium is greater than that of the surrounding medium). Optical trapping occurs where the two forces are balanced: in optical tweezers this is usually close to the laser's focal point, where the beam is most intense. It is the aim of this section to explain the origins of these optical forces.

A typical optical tweezers experiment takes place in a spatial regime in which the characteristic length-scale of the trapped particle, a, is comparable to the wavelength of the trapping laser ($a \approx \lambda \approx 1\mu\text{m}$). To accurately calculate the optical forces under such conditions requires a complete wave-optical modelling of the particle-light interaction based on electromagnetic scattering theory. However, approximations that greatly simplify the problem and aid understanding can be made in two extreme cases: firstly, a trapped sphere with a radius that is much larger than the wavelength of the trapping laser ($a \gg \lambda$); secondly, a sphere with a radius that is much smaller than the wavelength ($a \ll \lambda$). In the first of these cases the optical forces can be

Figure 2.1: Ray optics model of transverse trapping. Rays (1) and (2) are incident on a sphere. Scattering events lead to a deflection of the beams, which results in a change of momentum to each beam, $\delta p^{(1)}$ and $\delta p^{(2)}$. The geometry of the system depicted means that the change in momentum of ray (2) is larger than ray (1), so the net force points to the right as depicted by the arrow. Image taken from [30]

derived from a simple ray optics picture. In the second case, the particle may be treated as an induced point dipole and the optical forces derived from the dipole's interaction with the oscillating electromagnetic field of a laser.

Despite these approximations being strictly inapplicable to most optical tweezers experiments, the physical insight gained from the ray optics and dipole scattering pictures is very useful. Furthermore, given the large computational demands of a full scattering treatment and the fact that such calculations are influenced by difficult-to-quantify optical properties (such as spherical aberrations) it is rarely practical to carry out theoretical calculations in order to determine the optical forces at play in a given experiment. In practice, if one wants to know the force acting on a particle held in optical tweezers, a direct calibration of the trap's spring constant (via one of the methods described in the next section) is likely to be the most convenient approach. Indeed, that is the approach taken in the experiments described in this thesis and for this reason I will not give details of wave-optical modelling here.

2.2 Ray optics

A ray optics approach is applicable to a regime in which the characteristic length-scale of the trapped particle is much larger than the wavelength of the trapping laser ($a \gg \lambda$). Figure 2.1 shows two parallel rays of light, (1) and (2), incident on the outer surface of a sphere. For a small angle of incidence most of the power

carried by the rays is transmitted by the surface. If the sphere has a refractive index greater than that of its surrounding medium - such as the latex spheres suspended in water used in Ashkin's experiments ($n_\mathrm{s} = 1.58$ and $n_\mathrm{m} = 1.33$, respectively) - the angle of transmission will be smaller than the angle of incidence, i.e. the direction of the rays' propagation changes upon entering the sphere. The transmitted rays are then incident on the opposing inner surface of the sphere. Most of the power is transmitted and, again, there is a change to the direction of the rays' propagation. After passing through the sphere there has been a change in the momentum to both rays, $\boldsymbol{\delta p}^{(1)}$ and $\boldsymbol{\delta p}^{(2)}$. By conservation of momentum, an equal and opposite momentum is imparted to the sphere.

A ray that is incident on a planar surface at a normal incidence will be perfectly reflected. The force exerted on the surface is equal to the change in momentum of the ray, which is given by $(2P/c)\hat{\boldsymbol{r}}$, where P is the power of the ray (equal to the number of photons carried by the ray N multiplied by the of energy u of each photon), c is the speed of light in a vacuum and $\hat{\boldsymbol{r}}$ is the unit vector in the direction of the ray's propagation. In the more general case of a ray that strikes a non-planar surface (such as a sphere) at an angle away from the normal, part of the ray will be reflected and part will be transmitted. In this case the force exerted on the sphere is given by the following equation [7]:

$$\boldsymbol{F} = \frac{n_\mathrm{i} P_\mathrm{i}}{c}\hat{\boldsymbol{r}}_\mathrm{i} - \frac{n_\mathrm{i} P_\mathrm{r}}{c}\hat{\boldsymbol{r}}_\mathrm{r} - \frac{n_\mathrm{t} P_\mathrm{t}}{c}\hat{\boldsymbol{r}}_\mathrm{t}, \tag{2.1}$$

where n_i and n_t are the refractive indices of the media in which the incident and transmitted rays propagate, P_i, P_r and P_t are the powers of the incident, reflected and transmitted rays and $\hat{\boldsymbol{r}}_i$, $\hat{\boldsymbol{r}}_r$ and $\hat{\boldsymbol{r}}_t$ are the unit vectors parallel to the incident, reflected and transmitted rays direction of travel.

In the case of a sphere, the part of the ray that is transmitted by the first surface travels through the sphere to strike the opposing surface. A part of the ray will be transmitted by this surface and a part of the ray will be reflected back inside the sphere. This process continues until all the light has left the sphere. In order to work out the total force acting on the sphere we can implement equation (2.1)

repeatedly. However, the largest contributions to the force exerted by the ray are the first two scattering events, that is, the first reflection of the incident light and the first transmission out of the sphere. Therefore, it is often sufficient to neglect all later scattering events thereby significantly simplifying calculations.

It is possible to split the force $\boldsymbol{F}$ into the scattering force $\boldsymbol{F}_{\mathrm{s}}$ that pushes the sphere in direction of the incident ray $\hat{\boldsymbol{r}}_{\mathrm{i}}$ and the gradient force $\boldsymbol{F}_{\mathrm{g}}$ that pulls the particle in a direction perpendicular to the incident ray $\boldsymbol{r}_{\perp}$:

$$\boldsymbol{F} = F_s\hat{\boldsymbol{r}}_i + F_g\boldsymbol{r}_{\perp}. \tag{2.2}$$

The scattering force is due to the reflection at the sphere's surface and the gradient force is due to refraction of the light inside the sphere.

If the number of rays striking a sphere on either side of its vertical axis is equal, the forces acting on that sphere to the left and to the right cancel each other out. If an intensity gradient is present (such as the typical Gaussian profile of a laser beam), however, the sphere will feel a net force towards the point of greatest intensity. In a collimated Gaussian beam the gradient force will pull a particle towards the axis of the beam but the scattering force will push it along the beam.

In the case of a strongly focused beam, as in Figure 2.2, it is possible that the gradient force will be of such magnitude and direction that it is sufficient to overcome the scattering force and trap the sphere close to the focal point of the beam. This balancing of the two forces is the underlying concept of how optical tweezers operate.

Figure 2.2: Ray optics model of axial trapping. $\boldsymbol{\delta p}_{\mathrm{scat}}$ and $\boldsymbol{\delta p}_{\mathrm{grad}}$ represent changes in the momentum of the rays due the scattering and gradient forces respectively. Image taken from [30].

2.3 Dipole approximation

The dipole approximation is applicable to a regime in which the characteristic length-scale of the trapped object is much smaller than the wavelength of the trapping laser ($a \ll \lambda$). It allows us to treat the behaviour of a small dielectric sphere in an electric field as that of an electric dipole. An electric dipole is a separation of positive and negative charges; the extent of the separation is characterised by a dipole moment $\boldsymbol{p}$. In a monochromatic electric field, which is not too large, the dipole moment of the sphere will be linearly proportional to the electric field $\boldsymbol{E}$:

$$\boldsymbol{p} = \alpha \boldsymbol{E}. \tag{2.3}$$

Both the electric field and the dipole moment are expressed here in terms of their phasors, i.e. their time-invariant complex amplitude. The term of proportionality, α, is the polarisability of the sphere, which is a measure of the sphere's ability to form a dipole. In an oscillating electromagnetic field (such as a laser beam) the polarisability [31] is given by

$$\alpha = \alpha_{CM} \left[1 - i \frac{k_0^3 \alpha_{CM}}{6\pi\epsilon_0} \right]^{-1} \tag{2.4}$$

where ϵ_0 is the dielectric permittivity of a vacuum, k_0 is the wavevector of the electric field, a is the radius of the sphere, V is the volume of the sphere ($V = \frac{4}{3}\pi a^3$) and α_{CM} is the Clausius-Mossotti (CM) polarisability:

$$\alpha_{CM} = 3V\epsilon_0 \frac{m^2 - 1}{m^2 + 2}, \tag{2.5}$$

where m is the ratio of the refractive indices of the sphere n_s and the surrounding medium n_m. The CM polarisability is correct for a dipole in a static field. In an oscillating field, the dipole will oscillate and radiated a scattered field. The polarisability of the dipole depends on both the external oscillating field and the dipole's own scattered field. The second term within the brackets in equation (2.4) can be thought of as a correction to the CM polarisability that accounts for the

interaction with its own scattered field.

Under the dipole approximation, the time-averaged force acting on a dielectric sphere in a monochromatic, harmonic electromagnetic field of frequency ω is [32]

$$\langle \boldsymbol{F} \rangle = \frac{1}{4} Re\{\alpha\} \boldsymbol{\nabla} |E|^2 + \frac{\sigma}{2} Re \left\{ \frac{1}{c} \boldsymbol{E} \times \boldsymbol{H}^* \right\} - \sigma c \boldsymbol{\nabla} \times \left[\frac{\epsilon_0}{4i\omega} (\boldsymbol{E} \times \boldsymbol{E}^*) \right] \tag{2.6}$$

where $\sigma = k_0 Im\{\alpha\}/\epsilon_0$ is the scattering cross-section of the sphere, $\boldsymbol{H}$ represents the phasor of the magnetic field and an asterisk represents the complex conjugate. Equation 2.6 may be split into three parts: the first term describes the gradient force exerted on the sphere; the sum of the second and third terms, which are proportional to the scattering cross-section, describe the scattering force exerted on the sphere.

2.3.1 Gradient force

The gradient force is responsible for confinement in optical tweezers. Since the intensity of the electric field is given by $I = \frac{1}{2} c \epsilon_0 |E|^2$, the gradient force can be written in terms of the gradient of the field intensity,

$$\boldsymbol{F}_{grad} = \frac{1}{2} \frac{Re\{\alpha\}}{c\epsilon_0} \nabla I = \frac{3}{2} \frac{V}{c} \left(\frac{m^2 - 1}{m^2 + 2} \right) \nabla I. \tag{2.7}$$

We see that a sphere with a positive polarisabiltiy, i.e. a sphere with refractive index greater than that of its surroundings ($m > 1$), is attracted to the region of greatest intensity.

To a first approximation, the intensity distribution at the focus of a laser beam can be considered to be Gaussian. At small displacements from the axis, working in one-dimension for simplicity, the intensity is given by

$$I(x) = I_0 e^{-2\frac{x^2}{\omega_0^2}} \approx I_0 \left(1 - 2\frac{x^2}{\omega_0^2} \right), \tag{2.8}$$

where I_0 is the maximum intensity and ω_0 is the beam waist. The gradient force can then be approximated as a restoring force,

$$F = -\kappa x, \tag{2.9}$$

where the constant of proportionality κ is given by

$$\kappa = 6\frac{V}{c\omega_0^2}\left(\frac{m^2-1}{m^2+2}\right)I_0. \tag{2.10}$$

Thus we have a potential of a harmonic form

$$U(x) = -\int_{x_0}^{x} F dx = \frac{1}{2}\kappa x^2 + U(x_0). \tag{2.11}$$

2.3.2 Scattering force

The second term in equation (2.6) is proportional to $Re\{\boldsymbol{E}\times\boldsymbol{H}^*\}$, which is known as the Poynting vector, $\boldsymbol{S}$. The Poynting vector represents the rate of energy transfer per unit area, or the flux of energy density, in the wave. The momentum carried by an electromagnetic wave is given by the energy divided by its speed, c. Therefore, the $Re\{\boldsymbol{E}\times\boldsymbol{H}^*\}/c$ term in equation 2.6 represents the momentum density of the wave. In the case of a plane wave it acts in the same direction as the Poynting vector, that is, along the direction of the beam's propagation.

The third term in equation (2.6) is proportional to the curl of $(\epsilon_0/4i\omega)(\boldsymbol{E}\times\boldsymbol{E}^*)$, which can be identified as the time-averaged spin density of the electromagnetic field, $\langle\boldsymbol{L}_s\rangle$. This 'spin-curl' force term is small in comparison with the first two terms of equation (2.6) and does not usually play a significant role in optical tweezers experiments. It is associated with non-homogeneous distribution of polarisation in the field. For a plane wave this term is zero, but it does play a more significant role when a non-uniform helicity spatial distribution is present in the light field [32].

Figure 2.3 shows how the gradient and scattering components act on a dipole at the focus of a laser. The gradient force points towards the region of highest intensity in the focus, whereas the scattering force points in the direction of the beam propagation. The net result is trapping just beyond the beam waist.

Figure 2.3: Illustration of the forces acting on a dipole in a focused laser beam. The beam propagates in the z-direction. The gradient forces are shown in (a), acting towards the region of greatest intensity. The scattering forces are shown in (b), acting in the direction of the laser's propagation. The sum of the two forces are shown in (c). NB the scattering force in (b) is doubled in magnitude for clarity. The zero points of the gradient are total force are shown as circle. Image taken from [33].

Chapter 3

Particle Dynamics

3.1 Introduction

Optical tweezers are commonly employed to spatially confine suspended colloidal particles. Particles in a fluid suspension will perpetually change their position due to the thermal agitation of the surrounding molecules. This random motion is known as *Brownian motion*, after Robert Brown [34], and is an ever-present opponent to the confining forces of optical tweezers. Although optical tweezers can restrict the amplitude of a particle's motion, Brownian motion cannot be totally subdued in an optical tweezers experiment. Even at thermal equilibrium a trapped colloid will not come to complete rest in the tweezers. Whilst this fact may initially appear to be an irritation to experimentalists, we will see that we can in fact utilise this restless behaviour to harvest useful information about the potential energy landscape created by the tweezers. Figure 3.1 compares the trajectories of an unconstrained particle and a particle constrained by an optical potential (the data shown was produced in a finite-difference simulation, details of this are given later in section 3.8). In both cases the random nature of the motion is apparent, although of course it is somewhat curtailed in the trapped particle. The tendency for an unconstrained particle to move away from its initial position is also apparent; Brownian motion is a dominant factor in particle diffusion.

In order to understand the motion of a trapped colloid we introduce in this chapter an appropriate mathematical framework. It is possible to write down and

solve equations for every molecule in the fluid in order to predict the motion of the larger colloidal particle. However this is a prohibitively arduous task given the vast number of molecules involved. Instead, we can recast the many degrees of freedom associated with the fluid into a single variable that represents the viscosity of the fluid, γ, and the buffeting action of the fluid molecules into a randomly fluctuating force term, $\boldsymbol{\xi}(t)$. This approach leads to an equation of motion for the particle, referred to as a *Langevin equation*. It is named for the French physicist Paul Langevin, who introduced it in the early twentieth century [35].

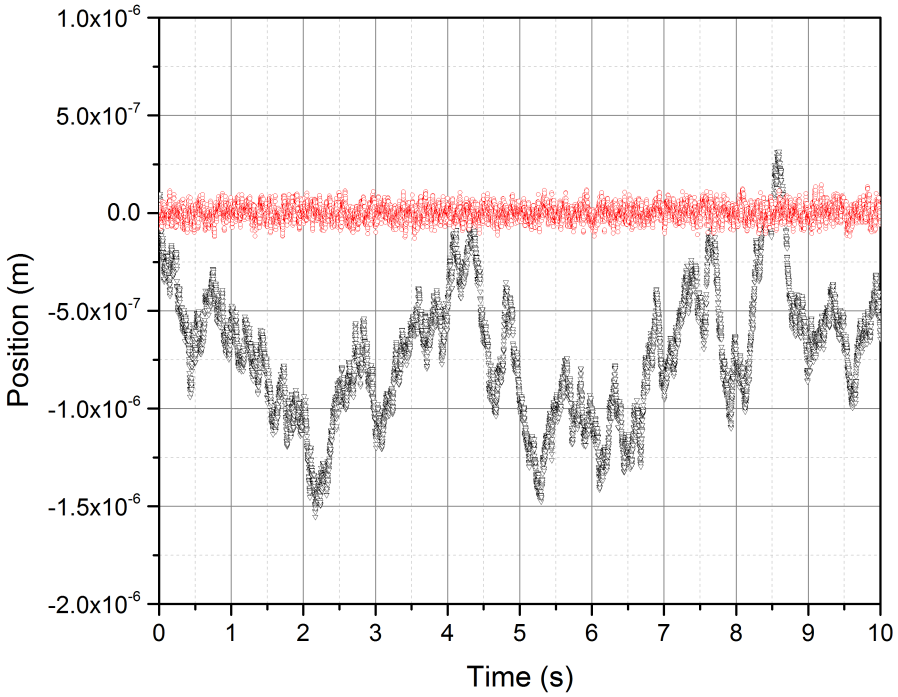

Figure 3.1: Trajectories of a trapped (red circles) and non-trapped (black triangles) particle subject to Brownian motion.

3.2 The Langevin equation

Brownian particles are subject to Newton's second law of motion which states that the total force acting on an object is equal to the sum of the individual forces acting

on it:

$$\boldsymbol{F} = m\dot{\boldsymbol{v}} = \sum_{i=1}^{N} \boldsymbol{f}_i. \tag{3.1}$$

If we take mass to be unity, equation (3.1) for a Brownian particle is equivalent to

$$\dot{\boldsymbol{v}}(t) = -\gamma \boldsymbol{v}(t) + \boldsymbol{\xi}(t). \tag{3.2}$$

The right hand side of equation (3.2) is the force exerted on the particle by the molecules of the surrounding fluid. The force is unknown at this point but we postulate three physical properties of it [36].

1. The force consists of a damping term linear in $\boldsymbol{v}$, with a constant coefficient γ, plus a remaining term $\boldsymbol{\xi}(t)$. The $\boldsymbol{\xi}(t)$ force is irregular and unpredictable, but its averaged properties over an ensemble of similar systems are simple.

2. The average of $\boldsymbol{\xi}(t)$ vanishes,

$$\langle \boldsymbol{\xi}(t) \rangle = 0. \tag{3.3}$$

3. The force $\boldsymbol{\xi}(t)$ is caused by the collisions of the individual molecules of the surrounding fluid and varies rapidly. This is expressed by postulating for its autocorrelation function

$$\langle \boldsymbol{\xi}(t_1)\boldsymbol{\xi}(t_2) \rangle = \Gamma \delta(t_1 - t_2), \tag{3.4}$$

where Γ is a constant and δ is the Dirac delta function with the following properties,

$$\delta(t_1 - t_2) = \begin{cases} \infty, & t_1 = t_2 \\ 0, & t_1 \neq t_2. \end{cases} \tag{3.5}$$

The idea is that each collision is practically instantaneous and that successive collisions are uncorrelated. A term that satisfies the three above properties is called a Langevin force and equation (3.2) is a Langevin equation.

3.3 The fluctuation-dissipation relation

We cannot know the precise time-dependence of the stochastic force term $\boldsymbol{\xi}(t)$, so we assume it is a stochastic variable with some plausible distribution [37]. We can find a solution to equation (3.2) in terms of $\boldsymbol{\xi}(t)$, allowing us to characterise the mean and the variance of the velocity, and to derive a relationship that describes the magnitude of the fluctuating term. We solve equation (3.2) with the use of integration factor $e^{\gamma t}$ [38].

$$\boldsymbol{v}(t) = \boldsymbol{v}_0 e^{-\gamma t} + \int_0^t e^{-\gamma(t-s)} \boldsymbol{\xi}(s) ds, \tag{3.6}$$

where $\boldsymbol{v}_0$ is the velocity at $t = 0$. Taking the average of the velocity over an ensemble of trajectories and employing equation (3.3), we find that

$$\langle \boldsymbol{v}(t) \rangle = \boldsymbol{v}_0 e^{-\gamma t}, \tag{3.7}$$

which implies that the average velocity of a Brownian particle decays exponentially with a characteristic timescale of $1/\gamma$. This timescale $(1/\gamma)$ is referred to as the mobility of the system. We may also take the variance of the velocity:

$$\langle \boldsymbol{v}^2(t) \rangle = e^{-2\gamma t} \boldsymbol{v}_0^2 + \int_0^t \int_0^t e^{-\gamma(t-s_1)} e^{-\gamma(t-s_2)} \langle \boldsymbol{\xi}(s_1) \boldsymbol{\xi}(s_2) \rangle ds_1 ds_2. \tag{3.8}$$

Given equation (3.4) and the properties of the delta function, the only contribution to the integral in equation (3.8) is when $s_1 = s_2$. Therefore,

$$\begin{aligned} \langle \boldsymbol{v}^2(t) \rangle &= e^{-2\gamma t} \boldsymbol{v}_0^2 + \Gamma \int_0^t e^{-2\gamma(t-s_1)} ds_1 \\ &= e^{-2\gamma t} \boldsymbol{v}_0^2 + \frac{\Gamma}{2\gamma} \left(1 + e^{-2\gamma t}\right). \end{aligned} \tag{3.9}$$

At long times, $t \to \infty$, the mean squared velocity has the known thermal value $k_B T$, by the equipartition theorem, and we see that

$$\langle \boldsymbol{v}^2(\infty) \rangle = \frac{\Gamma}{2\gamma} = k_B T. \tag{3.10}$$

We have now found a value for the constant Γ that describes the size of the fluctuating term in equation (3.4):

$$\Gamma = 2\gamma k_B T. \tag{3.11}$$

We see that the size of the fluctuations is governed only by temperature and the damping coefficient γ. Stoke's law tells us that for a spherical particle of radius a the drag coefficient is $\gamma = 6\pi\eta a$, where η is the viscosity of the surrounding fluid. Equation 3.11 is an expression of the fluctuation-dissipation theorem, which relates the size of fluctuations to the rate of dissipation, γ. Equation (3.4) may now be written in full:

$$\langle \boldsymbol{\xi}(t_1)\boldsymbol{\xi}(t_2)\rangle = 2\gamma k_B T\delta(t_1 - t_2). \tag{3.12}$$

3.4 Over-damped motion in a harmonic potential

So far we have considered a Langevin equation that describes the free diffusion of a Brownian particle. We now include an additional force term to account for the constraining effect of an optical trapping potential, $\boldsymbol{U}(x)$:

$$m\dot{\boldsymbol{v}}(t) = -\gamma\boldsymbol{v}(t) + \boldsymbol{\xi}(t) - \frac{d\boldsymbol{U}(x)}{dx}. \tag{3.13}$$

Earlier, for algebraic ease, we set the mass term in our Langevin equation equal to unity. However, we will now see that in specific circumstances it is more appropriate to set the mass equal to zero. The experiments described in this thesis take place in an aqueous environment, which is a *low-Reynolds-number* regime. The Reynolds number, $Re = av\rho/\eta$ (where ρ is the density of the fluid), is the ratio of inertial and viscous forces acting on a particle moving through a fluid. When we are in the low-Reynolds-number regime ($Re \lesssim 100$) viscosity dominates over inertia, which means that the inertial term in equation (3.13) - $m\dot{\boldsymbol{v}}(t)$ - is negligible and may be omitted [7]:

$$0 = -\gamma\boldsymbol{v}(t) + \boldsymbol{\xi}(t) - \frac{d\boldsymbol{U}(x)}{dx}. \tag{3.14}$$

We are interested in the trapping potential provided by optical tweezers so we consider a potential with an appropriate form, i.e. a harmonic potential with the form

of equation (2.11). The force produced by the optical tweezers behaves like the force produced by a Hookean spring, as seen in equation (2.9). Equation (3.14), in terms of position, becomes

$$\gamma\dot{\boldsymbol{x}}(t) = -\kappa\boldsymbol{x}(t) + \boldsymbol{\xi}(t), \tag{3.15}$$

where κ is the trap stiffness and $\boldsymbol{x}(t)$ is the position of the particle relative to the minimum of the harmonic potential. The solution to equation (3.15), with initial condition $x(0) = x'$,

$$\boldsymbol{x}(t) = x' \exp(-t/\tau) + \frac{1}{\gamma}\int dt' \exp(-(t-t')/\tau)\boldsymbol{\xi}(t), \tag{3.16}$$

is an exponential decay towards equilibrium, telling us that the system is an *over-damped* oscillator. The decay constant is given by $\tau = \gamma/\kappa$.

3.4.1 Constant fluid flow

If the trapped particle is subjected to a fluid flow of constant velocity, the particle will move to a new equilibrium position that is displaced from the minimum of the potential. In such a case, equation (3.15) is modified by the addition of a fluid velocity term, $\boldsymbol{\nu}_f$:

$$\gamma(\dot{\boldsymbol{x}}(t) + \boldsymbol{\nu}_f) = -\kappa\boldsymbol{x}(t) + \boldsymbol{\xi}(t). \tag{3.17}$$

It will prove useful later in this thesis to have a mathematical form that describes the average, or expected, trajectory of the particle as it relaxes to its new equilibrium position. We proceed by taking the ensemble average of equation (3.17):

$$\langle\dot{\boldsymbol{x}}(t) + \boldsymbol{\nu}_f + \kappa\boldsymbol{x}(t)\rangle = \langle\boldsymbol{\xi}(t)\rangle = 0. \tag{3.18}$$

Similarly to equation (3.6), this equation can be solved with the use of an integrating factor to find

$$\langle\boldsymbol{x}(t)\rangle = \tau\boldsymbol{\nu}_f(1 - \exp(-t/\tau), \tag{3.19}$$

where the time constant $\tau = \gamma/\kappa$ is the relaxation period of the particle in a trap with spring constant κ. The form of equation (3.19) tells us that the particle's

position will relax exponentially over time towards a displacement of $\tau\boldsymbol{\nu}_f$.

3.5 Position auto-correlation function

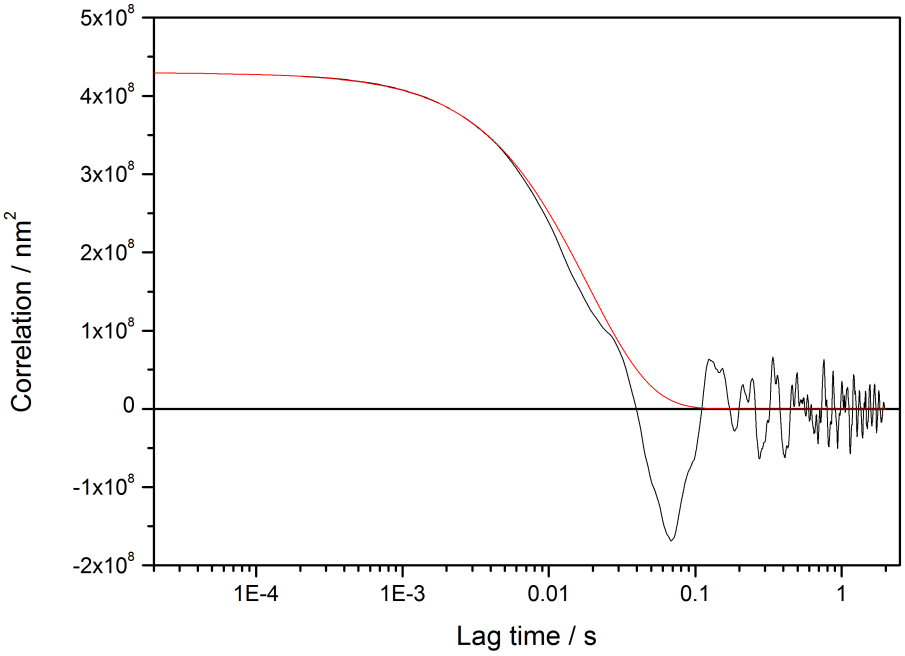

Figure 3.2: Autocorrelation of position for a (simulated) particle trapped in a harmonic potential along with a fit of the form in equation (3.24). Particle radius is $1\mu m$. The spring constant given by the fit is $\kappa = 1.02pN\mu m^{-1}$.

A useful tool for the characterisation of a harmonic trapping potential is the auto-correlation function (ACF). The ACF gives the correlation of a signal with itself as a function of lag-time [37]; in terms of the position of a trapped particle, the ACF provides a measure of how similar a particle's position is to some initial position. At short times, the particle is unlikely to have moved far from its initial position, so will be highly correlated. At later times the particle is unlikely to have remained in that initial position and its position becomes uncorrelated with the initial position. The temporal transition from correlation to non-correlation is described by the ACF. This can also be thought of as the time taken for the particle

to 'forget' its original position. The position ACF is defined as

$$C_{xx}(t) = \langle \boldsymbol{x}(0) \cdot \boldsymbol{x}(t) \rangle. \tag{3.20}$$

If we take the time derivative of the auto-correlation,

$$\dot{C}_{xx}(t) = \langle \boldsymbol{x}(0) \cdot \dot{\boldsymbol{x}}(t) \rangle, \tag{3.21}$$

and substitute for the time-derivative term in the Langevin equation, equation (3.15), we find that

$$\dot{C}_{xx}(t) = \frac{1}{\gamma} \langle \boldsymbol{x}(0) \cdot (-\kappa \boldsymbol{x}(t) + \boldsymbol{\xi}(t)) \rangle. \tag{3.22}$$

Now, because $\boldsymbol{x}(t)$ and $\boldsymbol{\xi}(t)$ are uncorrelated at all times other than $t = 0$, the $\langle \boldsymbol{x}(0)\boldsymbol{\xi}(t) \rangle$ term is zero and

$$\dot{C}_{xx}(t) = -\frac{\kappa}{\gamma} \langle \boldsymbol{x}(0)\boldsymbol{x}(t) \rangle = -\frac{\kappa}{\gamma} C_{xx}(t), \tag{3.23}$$

which has the simple solution

$$C_{xx}(t) = C_{xx}(0) \exp\left(-\frac{\kappa}{\gamma} t\right). \tag{3.24}$$

We see that the transition from correlation to non-correlation is described by an exponential decay with a characteristic time that depends on the trap spring constant and the drag coefficient. Let us define this value

$$\tau = \frac{\gamma}{\kappa}. \tag{3.25}$$

At zero lag-time, the energy stored in the trap is

$$U = \frac{\kappa}{2} \langle \boldsymbol{x}^2(0) \rangle = \frac{\kappa}{2} C_{xx}(0). \tag{3.26}$$

We can equate this to $k_BT/2$ via the equipartition theorem, allowing us to write

$$C_{xx}(t) = \frac{k_BT}{\kappa} \exp\left(-\frac{\kappa}{\gamma}t\right). \tag{3.27}$$

We have made several approximations in arriving at this equality. Firstly, in order to approximate the potential energy as harmonic we have assumed that the particle makes only small deviations from its equilibrium. Accordingly we assume that the restoring force is linear in the displacement of the particle from equilibrium. Secondly, we have approximated the force field as conservative. Whilst the forces due to the optical gradient are certainly conservative, the optical pressure due to the scattering is not. Experiments have reported manifestations of the non-conservative forces, showing that the a spherical particle in an optical tweezers does not come to equilibrium but instead performs a circulating motion in the axial direction [39] (see also [40]). However, these experiments were performed at very low trapping power and the effects of the non-conservative forces can safely be neglected in most optical tweezers experiments [41].

3.5.1 Optical trap calibration

Equation (3.27) allows us to characterise the potential landscape of the optical trap. If we know the sequence of positions of a particle in the trap, we can calculate the autocorrelation. A fit to the autocorrelation will reveal the value of the trapping constant κ. An example of the autocorrelation calculated for a particle in a harmonic potential is shown in figure 3.2 along with a fit of the form of equation (3.24). This is a very useful technique when calibrating an optical trap: a short recording of the particle's position can be easily analysed to yield the trapping constant κ, provided that γ is known.

3.6 Probability distributions

It is useful to be able to make predictions about the position of a trapped particle at some time in the future. The Green's function, $G(x_t, x_0; t, \kappa)$, gives the probability

that a particle in a trap of stiffness κ is at position x_t at time t, given that it was at position x_0 when $t = 0$. In order to write the Green's function explicitly we must assume a form for the random variable $\boldsymbol{\xi}(t)$. There are several possible forms for the distribution, but we will assume a Gaussian distribution with moments $\langle \boldsymbol{\xi}(t) \rangle = 0$ and $\langle \boldsymbol{\xi}(t_1)\boldsymbol{\xi}(t_2) \rangle = 2\gamma k_B T \delta(t_1 - t_2)$. Equation (3.16) implies that the position $x(t)$ is a combination of Gaussian random variables $\boldsymbol{\xi}(t)$. In turn, this implies that the Green's function, a probability distribution of position, also takes a Gaussian form [37]:

$$G(x_t, x_0; t, \kappa) = \frac{1}{\sqrt{2\pi B(t)}} \exp\left(-\frac{(x - A(t))^2}{2B(t)} \right), \tag{3.28}$$

where

$$A(t) = \langle x(t) \rangle, \qquad B(t) = \langle (x(t) - A(t))^2 \rangle. \tag{3.29}$$

Using equation (3.16), $A(t)$ and $B(t)$ may be calculated:

$$\begin{aligned} A(t) &= \langle x' \exp(-t/\tau) + \frac{1}{\gamma} \int dt' \exp(-(t - t')/\tau) \boldsymbol{\xi}(t) \rangle \\ &= x' \exp(-t/\tau), \end{aligned} \tag{3.30}$$

since $\langle \boldsymbol{\xi}(t) \rangle = 0$; and

$$\begin{aligned} B(t) &= \frac{1}{\gamma^2} \int_0^{t_1} dt_1 \int_0^{t_2} dt_2 \exp\left[-(t - t_1 + t - t_2)/\tau \right] \langle \boldsymbol{\xi}(t_1)\boldsymbol{\xi}(t_2) \rangle \\ &= \frac{k_B T}{\kappa} \left(1 - \exp(-2t/\tau) \right). \end{aligned} \tag{3.31}$$

Hence the Green's function is

$$G(x_t, x_0; t, \kappa) = \left(\frac{\kappa}{2\pi k_B T \left[1 - \exp\left(\frac{-2t}{\tau} \right) \right]} \right)^{\frac{1}{2}} \times \exp\left(-\frac{\kappa [x - x_0 \exp\left(\frac{-t}{\tau} \right)]^2}{2k_B T [1 - \exp\left(\frac{-2t}{\tau} \right)]} \right). \tag{3.32}$$

At long times, the Green's function becomes simply the Boltzmann distribution,

$$G(x_t, x_0; t \to \infty, \kappa) = P_B(x, \kappa) = \left(\frac{\kappa}{2\pi k_B T} \right)^{\frac{1}{2}} \exp\left(-\frac{\kappa}{2k_B T} x^2 \right), \tag{3.33}$$

as predicted by thermodynamics [42]. Figure 3.3 illustrates a distribution of particle positions in a harmonic potential. The blue bars are a histgoram of particle positions and the red curve represents the Boltzmann distribution of equation (3.33).

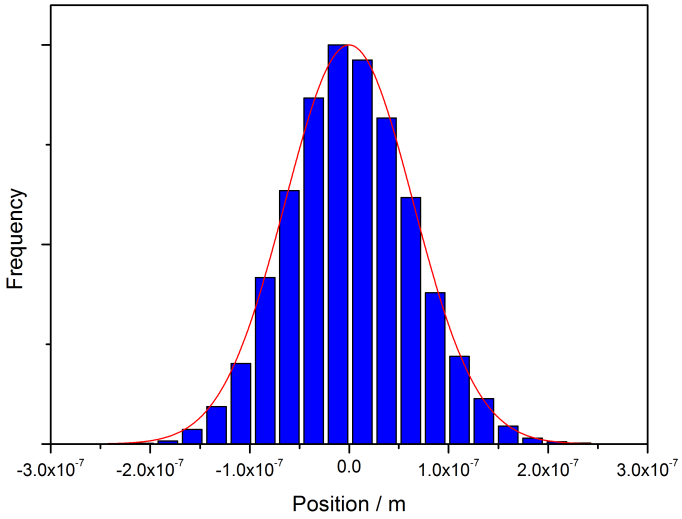

Figure 3.3: The bars are a histogram of the positions of a particle in a harmonic potential of stiffness $\kappa = 1\text{pN} \cdot \mu\text{m}^{-1}$. The red curve is the Boltzmann distribution which predicts the distribution of the particle's positions.

If we wanted to know the probability density $p(x_0, x_t)$ associated with the trajectory of a particle that begins at equilibrium in a trap at position x_0 at $t = 0$ before the trap centre is translated with some constant velocity v_{trap} so that the particle moves to position x_t, we would need to find the product of the Boltzmann distribution and the Green's function:

$$P(x_0, x_t) = P_B(x, \kappa)G(x_0, x_t; t, \kappa). \tag{3.34}$$

3.6.1 Optical trap calibration

Equation (3.33), which describes the shape of the distribution in figure 3.3, is a Gaussian distribution with a standard deviation of

$$\sigma^2 = \frac{k_B T}{\kappa}. \tag{3.35}$$

We can see that the standard deviation σ^2 is inversely proportional to the spring constant of the harmonic potential, κ. If we measure the position of a trapped particle N number of times, we can estimate the standard deviation as

$$\sigma^2 = \frac{1}{N}\sum_{n=1}^{N}(x_n - \bar{x})^2, \tag{3.36}$$

where $\bar{x}$ is the mean of position. If we know the temperature, T, we can use equation (3.35) to give a simple calculation of the spring constant of a harmonic potential.

3.7 The Langevin equation for multiple particles

As we have seen, the Langevin equation for a single particle held in a harmonic optical trap in an over-damped regime can be written as

$$\dot{\boldsymbol{x}} = \frac{1}{\gamma}\left(-\kappa\boldsymbol{x} + \boldsymbol{\xi}(t)\right). \tag{3.37}$$

If we want to extend this formulation to multiple interacting particles held in individual adjacent traps, we can replace the mobility term $1/\gamma$ with a mobility tensor $\boldsymbol{H}_{ij}$:

$$\dot{\boldsymbol{x}}_i = \sum_{j=1}^{N}\boldsymbol{H}_{ij}\left(-\kappa_j\boldsymbol{x}_j + \boldsymbol{\xi}_j(t)\right), \tag{3.38}$$

where κ_j represents the spring constant associated with the j^{th} trap and $\boldsymbol{\xi}_j(t)$ is the random Brownian force acting on the j^{th} particle. We note that more generally, equation (3.38) can be written

$$\dot{\boldsymbol{x}}_i = \sum_{j=1}^{N}\boldsymbol{H}_{ij}\boldsymbol{F}_j, \tag{3.39}$$

where $\boldsymbol{F}_j$ represents the total force acting on particle j.

The mobility tensor is derived from the Navier-Stokes equations, which describe the flow of incompressible Newtonian fluids, and is often referred to as the Oseen tensor or the Stokeslet [43]. The tensor couples the motion of particle i with the

motion of every other particle ($j = 1, ..., N$) in the system. It is defined as

$$\boldsymbol{H}_{ij} = \frac{\boldsymbol{I}}{\gamma}\delta_{ij} + \frac{3a}{4\gamma r_{ij}}(\boldsymbol{I} + \hat{\boldsymbol{r}}_{ij} \otimes \hat{\boldsymbol{r}}_{ij})(1 - \delta_{ij}), \tag{3.40}$$

where $\boldsymbol{I}$ is a 3×3 identity matrix, $\boldsymbol{r}_{ij} = \boldsymbol{r}_i - \boldsymbol{r}_j$, $r_{ij} = |\boldsymbol{r}_{ij}|$, δ_{ij} is the Kronecker delta function and $\otimes$ denotes the tensor product.

We should note here that the Oseen tensor is an approximation that only truly holds if the particles are well separated, such that they can be considered as point-like particles. In order to include in our model particles that are close to one another, we would need to incorporate the effects of the fluid flow induced by one particle on its neigbouring particles and the reciprocal flow caused by the induced motion. The effects are described by Faxen's Theorems; by incorporating these effects into the Stokes equations one arrives at the Rodne-Prager tensor [44]. The Rodne-Prager tensor is the first result in an iterative process known as the method of reflections in which one calculates the interaction between the particles to increasing orders. Once the fluid flow at particle j due to particle i has been calculated, the flow due to the induced motion of particle j is used to calculate the fluid flow at particle i. One has to make a choice about the accuracy at which one is willing to work. One immediate implication of using higher order approximations is that Brownian motion simulations, see section 3.8, will take much longer to run if they are required to calculate more complex tensors at each step.

If the particles are well confined by their traps, i.e. their position fluctuations are small in comparison to trap separation, we can replace the time dependent vectors $\boldsymbol{r}_{ij}$ with the locations of their trap centres $\boldsymbol{R}_i$ to obtain a time-independent approximation to $\boldsymbol{H}_{ij}$. This approximation has been applied in several studies [1, 20, 45] and was found to provide good agreement with experiment. The noise terms in equation (3.38) have the following characteristics:

$$\langle \boldsymbol{\xi}_i(t) \rangle = 0; \qquad \langle \boldsymbol{\xi}_i(t)\boldsymbol{\xi}_j(t) \rangle = 2k_B T \boldsymbol{H}_{ij}^{-1}\delta(t - t'). \tag{3.41}$$

If the system in question consists of a regular arrays of traps, we can decompose the Oseen tensor into longitudinal ($||$) and transverse ($\perp$) components relative to the

array's axis:

$$\gamma \boldsymbol{H}_{ij}^{||} = \begin{cases} \frac{1}{\gamma}, & i = j \\ \frac{3}{2}\frac{a}{L}\frac{1}{|i-j|}, & i \neq j \end{cases} \qquad \gamma \boldsymbol{H}_{ij}^{\perp} = \begin{cases} \frac{1}{\gamma}, & i = j \\ \frac{3}{4}\frac{a}{L}\frac{1}{|i-j|}. & i \neq j \end{cases} \tag{3.42}$$

The normal modes of the system, $\boldsymbol{X}_i^{||}(t)$ and $\boldsymbol{X}_i^{\perp}(t)$, are the eigenvectors of the

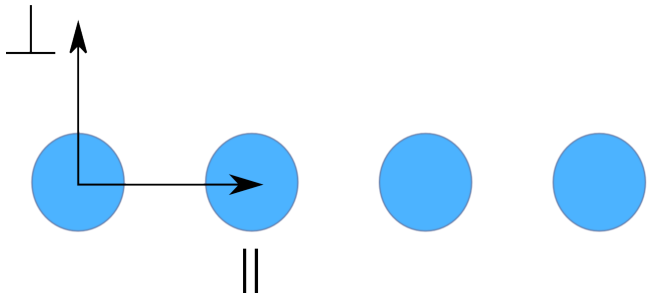

Figure 3.4: Illustration of particles held in an array of optical tweezers. The longitudinal (||) and transverse ($\perp$) components are shown.

above matrices and Λ_i are the associated eigenvalues. Each mode satisfies the Langevin equation:

$$\dot{\boldsymbol{X}}_i = -\kappa \Lambda_i \boldsymbol{X}_i + \boldsymbol{\Phi}_i(t), \tag{3.43}$$

where the random force term has zero mean and covariance

$$\langle \boldsymbol{\Phi}_i(t) \boldsymbol{\Phi}_j(t') \rangle = 2k_B T \gamma \Lambda_i \delta_{ij} \delta(t - t'). \tag{3.44}$$

We showed in sections 3.3 and 3.4 how motion of this kind is characterised.

In the two particle system that we are currently concerned with, the two normal modes are a *correlated* motion of the particles (in which both particles move in the same direction) and an *anti-correlated* motion (in which the particles move with in opposing directions). Any arbitrary motion of the system may be described as a superposition of the normal modes [38].

3.7.1 Cross-correlation of adjacent particles

In an influential paper, published in 1999, Meiners and Quake [1] showed that the Oseen coupling tensor leads to a pronounced anti-correlation in the fluctuating po-

Figure 3.5: Measured auto- and cross correlation of two particles in adjacent traps, as mesaured by Meiners and Quake [1]

sitions of two particles held in adjacent optical tweezers. In order to describe the system it is helpful to think about the underlying modes of the system (we will only concern ourselves with the longitudinal motion of the particles here):

$$X_1 = \frac{1}{\sqrt{2}}(x_1 + x_2); \qquad X_2 = \frac{1}{\sqrt{2}}(x_1 - x_2). \tag{3.45}$$

Each mode has an associated eigenvalue, Λ_i:

$$\Lambda_{1,2} = \boldsymbol{H}^{||}_{11} \pm \boldsymbol{H}^{||}_{12}. \tag{3.46}$$

Analogously to the auto-correlation of a single particle (equation (3.27)), the auto-correlation of each mode is given by

$$C_{X_iX_j}(t) = \langle X_i(0)X_j(t)\rangle = \delta_{ij}\frac{k_BT}{\kappa}\exp(-\kappa\Lambda_i t). \tag{3.47}$$

In their paper, Meiners and Quake show that the cross-correlation of the particles' positions can be derived from the mode autocorrelation:

$$\begin{aligned} C_{x_1x_2} &= \langle x_1(0)x_2(t)\rangle \\ &= \frac{1}{2}\langle (X_1(0) + X_2(0)(X_1(t) - X_2(t))\rangle \\ &= \frac{k_BT}{2\kappa}\left[\exp(-\kappa\Lambda_1 t) - \exp(-\kappa\Lambda_2 t)\right] \\ &= \frac{k_BT}{2\kappa}\left[\exp\left(-\frac{t}{\tau_1}\right) - \exp\left(-\frac{t}{\tau_2}\right)\right], \end{aligned} \tag{3.48}$$

where the decay constants, τ_i, are given by

$$\tau_{1,2} = (\kappa\Lambda_{1,2})^{-1}. \tag{3.49}$$

The difference in the decay constants in the last line of equation (3.48) gives rise to the anti-correlated behaviour evident in figure 3.5. Physically, this is due to the fact that mode X_1 (the correlated mode) decays faster than mode X_2 (the anti-correlated mode); it is easier for two particles to relax in the same direction than it is in opposite directions. In order for the particles to move in opposite directions fluid must be squeezed into the gap between the particles, whilst the fluid flow generated by the movement of one particle tends to entrain the second particle [46].

3.8 Brownian dynamics simulations

The Langevin equation can be solved numerically to give the positional evolution of a Brownian particle through use of a finite-difference algorithm [47]. This provides a useful method for simulating experimental trajectories. The idea is to approximate the continuous-time solution, $x(t)$, of the Langevin equation with a discrete time sequence, x_i. The terms of the discrete time sequence are found by recursively solving the Langevin equation at finite time steps, $t_i = i\Delta t$. If Δt is sufficiently small, then x_i is a good approximation for $x(t)$.

The over-damped Langevin equation for a trapped particle can be written

$$\dot{\boldsymbol{x}}(t) = -\frac{\kappa}{\gamma}\boldsymbol{x} + \sqrt{\frac{2k_BT}{\gamma}}W(t), \tag{3.50}$$

if $W(t)$ is a white noise signal with the following characteristics:

1. the mean of $W(t)$ is zero for each value of time, $\langle W(t)\rangle = 0$;
2. the variance of $W(t)$ is unitary for each value of time, $\langle W(t)^2\rangle = 1$;
3. $W(t_1)$ and $W(t_2)$ are independent of each other for $t_1 \neq t_2$.

In order to write the finite-difference equation, the particle position, $x(t)$, and its

time derivative are replaced in equation (3.50) with the following:

$$\boldsymbol{x}(t) \to \boldsymbol{x}_i; \qquad \dot{\boldsymbol{x}}(t) \to \frac{\boldsymbol{x}_i - \boldsymbol{x}_{i-1}}{\Delta t}. \tag{3.51}$$

In order to include the noise term in the finite-difference equation, a sequence of random numbers, W_i, that will mimic the properties of $W(t)$, is needed:

1. W_i must be a sequence of random numbers with zero mean;
2. W_i must satisfy the condition that $\langle (W_i \Delta t)^2 \rangle / \Delta t = 1$, thus ensuring that the variance per unit time, Δt, is unitary;
3. W_i and W_j must be independent for $i \neq j$.

Some consideration should be given to the choice of time step used in this type of simulation. The time step should be signicacntly shorter than the relaxation time of the trapped particle, $\tau = \gamma/\kappa$. If $\Delta t \gtrsim \tau$ the simulation will show unphysical behaviour: the particle's position in the trap may appear to oscillate [47] or the particle may escape the trap. Additionally, the time step should be significanly longer than the momentum relaxation time, $\tau_m = m/\gamma$. If $\Delta t \lesssim \tau_m$, ballistic motion of the particle becomes important and the dynamics can no longer be accuratley described by the over-damped Langevin equation.

The simulations presented in this thesis are carried out in *MATLAB*, which contains a function called `randn` [48] that returns a random scalar, w_i, drawn from the standard normal distribution of zero mean and unitary variance. In order to satisfy the condition $\langle (W_i \Delta t)^2 \rangle / \Delta t = 1$, the generated sequence of numbers w_i are scaled by $\sqrt{\Delta t}$, i.e.

$$W(t) \to W_i = w_i / \sqrt{\Delta t}. \tag{3.52}$$

This ensures that the variance of W_i is $1/\Delta t$. Following these substitutions, equation (3.50) becomes

$$x_i = x_{i-1} - \underbrace{\frac{\kappa}{\gamma} x_{i-1} \Delta t}_{\text{deterministic}} + \underbrace{\sqrt{\frac{2 k_B T \Delta t}{\gamma}} w_i}_{\text{diffusive}}, \tag{3.53}$$

where I have labelled the second term on the right-hand side as the deterministic

contribution to the particle's motion and the third term as the random diffusive contribution for comparison with the example code shown below. In this example I have employed typical values for constants such as the spring constant and particle radius. The initial position of the particle, `x(1)`, is sampled from the Boltzmann distribution. Lines 12 to 16 execute the iterative expression in equation (3.53). Line 15 takes care of the deterministic part of equation (3.53) whilst line 17 is responsible for the diffusive step.

Listing 3.1: An example of a finite difference algorithm used to simulate Brownian trajectories based on the Langevin equation

```
% physical constants
kB = 1.38e-23;              % Boltzmann constant, J/K
T = 300;                    % temperature, K
eta = 0.88e-3;              % viscosity of water, Pa*s
a = 1e-6;                   % particle radius
gamma = 6*pi*eta*a;         % friction coefficient, Pa*s*m
kappa = 1e-6;               % spring constant, N/m
% simulation parameters
n = 1e5;                    % number of steps
dt = 1e-3;                  % time step, s
x(1) = sqrt(kB*T/kappa)*randn();
% simulation
for i = 2 : n
    % deterministic step
    x(i) = x(i-1) - (kappa/gamma)*x(i-1)*dt;
    % diffusive step
    x(i) = x(i) + sqrt(2*kB*T*dt/gamma)*randn();
end
```

Outline of Thesis

Following the introductory part of this thesis I will briefly outline the content of the remaining parts.

In part II, I present work on dynamical stabilisation in optical tweezers. Dynamical stabilisation describes a phenomena in which stability is induced in an inherently unstable system, due to an applied oscillatory force. A well know example of dynamic stabilisation is the inverted pendulum [49], in which a harmonic oscillation is applied to the vertical position of the suspension point of a rigid pendulum with no damping, causing the pendulum to stand upright. Here I present a microscopic, optical-pendulum that operates in a regime of strong damping and finite rigidity. The pendulum is realised using scanning optical tweezers to create a time-averaged ring shaped potential in which a colloidal particle is trapped. As an analogy to gravity, fluid flow across the ring drives the pendulum towards the bottom of its swing. Due to the over-damped nature of the pendulum, it does not oscillate, or 'swing' like a macroscopic pendulum. The pendulum's position is harmonically modulated in the direction of the fluid flow. A mathematical treatment of this system reveals a regime of behaviour in which the pendulum will explore a range of stability positions depending on the modulation amplitude and frequency. This regime is then explored through simulations and experiments.

In part III, I present experimental results from a study of red blood cell (RBC) deformability in patients with diabetic retinopathy (DR). It is well known that diabetes mellitus (DM) reduces the deformability of RBCs [50] and this has been linked to microvascular complications of diabetes such as nethropathy [51] (disease of the kidney). Here I investigate a link between RBC deformability and DR, a condition associated with the micro-vessels of the retina. A dual-beam optical tweezers set-up

is used to stretch individual RBCs. Using shape-analysis algorithms I calculate a *deformability index* based on the initial and maximum lengths of the cell during a standard stretching routine. I compare the deformability index of RBCs from patients with DR and a healthy control group.

In part IV, I present the results of experiments and simulations designed to test the applicability of the fluctuation theorem (FT) [52, 29] to coupled systems. The FT is a generalisation of the second-law of thermodynamics that can be applied to small systems far from equilibrium. Traditional concepts of thermodynamics such as the second-law, which governs the direction in which a system will proceed in time, only truly apply in the limit of large systems (or the average over an ensemble of states) close to equilibrium. For a small machine - a molecular motor, for example - where the work performed during the duty-cycle is comparable to the thermal energy per degree of freedom, it is possible for the machine to run in reverse over short time-scales. For a large machine this would be considered a violation of the second law. Experimental verification of the FT was achieved in 2002 by Wang *et al* [28]. Their experiment involved monitoring the trajectory of a single colloidal particle constrained by an optical trap that was translated at a small uniform velocity. Here I extend this idea to multiple hydrodynamically-coupled particles in adjacent optical traps.

Part II

Dynamical stabilisation in optical tweezers

Chapter 4

Dynamical stabilisation: introduction and theory

4.1 Introduction

It is intuitively understood that a simple pendulum - consisting of a mass suspended from a fixed point by a light, rigid rod - is in stable equilibrium at the lowest point of its swing, when the mass hangs vertically below the suspension point. The pendulum is also in equilibrium at the highest point of its swing, when the mass is vertically above the suspension point, although this *inverted* equilibrium position is not stable. It is possible to induce stability in the inverted position, however, by subjecting the suspension point to a vertical harmonic oscillation of sufficient frequency and amplitude. This phenomenon is referred to as the inverted pendulum or as *Kapitza's pendulum* after the Russian scientist Pyotr Kapitza who first provided an analytic explanation in 1951 [49]. The inverted pendulum is an example of a broader phenomenon known as dynamical stabilisation, in which stability arises in an intrinsically unstable system due to an oscillating force.

Here I present a study of dynamical stabilisation in an over-damped pendulum of finite rigidity, realised using optical tweezers. This model goes beyond the usual assumptions made about friction and pendulum rigidity when considering the in-

verted pendulum. The work described here illustrates a rich new regime of dynamic behaviour in which stability of the pendulum is dependent on not only driving frequency and amplitude, but also the friction coefficient of the system. Furthermore, the induced stability is not necessarily found at the inverted position: stability can be found on a spectrum of positions around the pendulum, dependent on the dynamical parameters.

Beyond the intrinsic interest of the system under study here, an understanding of dyanamical stabilisation in a colloidal system may lead to useful applications in particle-sorting. Given, as it will be shown, that the position of stabilisation is dependent on the fricition coefficient associated with a particle and hence the particle's size, it is conceivable that by introducing a periodic oscilation to a potential that contains a number of particles of different sizes, the particles will be sorted into regions depending on their size.

4.1.1 Outline of part II

In the remainder of chapter 4, I provide a theoretical framework for the experimental work described in chapter 5. In section 4.2 I give a brief physical explanation for inverted stability in a typical simple pendulum. In section 4.3 I give some detail on how optical tweezers are used to realise our pendulum. Finally, in section 4.4 I look analytically at stability in the pendulum. In the following chapter, chapter 5, I present simulations and experiments that test the predictions of the analytic analysis.

4.2 Physical explanation for inverted stability

Following the pedagogic description by Butikov [**?**], we can establish an understanding of the physical reasons for inverted stability of a typical rigid macroscopic pendulum by considering the torque acting on the mass during the oscillation of the suspension point.

Let us define the motion of the suspension point, which is restricted to the vertical direction, as $z(t) = a\sin(\omega t)$, where a is the amplitude of the oscillation and

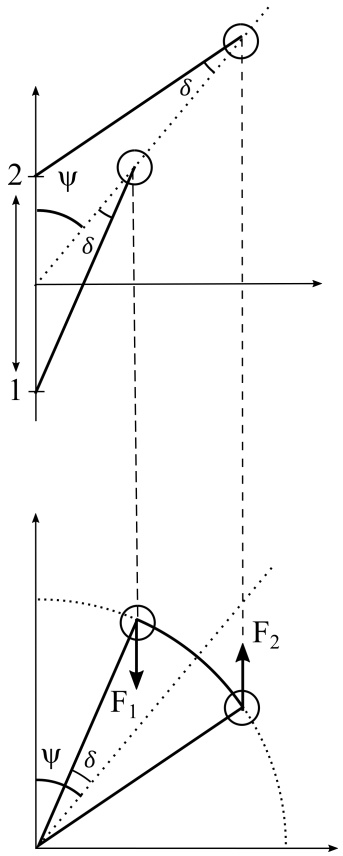

Figure 4.1: Upper image illustrates the effect of an oscillating suspension point on the instantaneous position of a rigid pendulum in an inertial reference frame. Lower image illustrates that in a non-inertial reference frame (that moves with the suspension oscillation) the mass moves along the arc of a circle centred at the pendulum axis. This image is an imitation of a figure in reference [**?**].

ω is its frequency. This oscillation provides a force that acts on the mass for equal times in the positive and negative vertical directions. The upper image in figure 4.1 illustrates how the oscillations affect the instantaneous angle of the rod in an inertial reference frame.

We assume the rod is at some arbitrary initial angle from the vertical, ψ, and that the oscillation of the suspension point provides an additional, rapidly changing anglular displacement, $\delta(t)$. As the suspension point is driven downward toward position 1 (where the suspension point is at its minimum, $-a$) the torque acting on the mass works to align the rod with the direction of oscillation - to position the mass above the suspension point. When the direction of the drive is reversed so that the suspension point is moving upward toward position 2 (where the suspension point is at its maximum, $+a$), the direction of the torque acting on the mass is also

reversed - the torque now works to position the mass below the suspension point.

The magnitude of the torque is proportional to the perpendicular distance between the axis of rotation and the line of action of a force. If we now consider a non-inertial frame of reference that moves according to $z(t)$, we will find the situation illustrated in the lower image in figure 4.1. In this reference frame the mass moves along the arc of a circle whose centre coincides with the axis of the pendulum. We can clearly see now that for an acute initial angle ψ the perpendicular distance between the axis of rotation and the line of action is greater at position 2 than it is in position 1. Although the force acting on the mass, averaged over the period of oscillation, is zero, the torque is not. If the initial angular displacement from the vertical is acute, the net torque tends to push the pendulum into an inverted position.

4.3 Microscopic optical-pendulum

In the work presented here, the induced stability of a pendulum that operates outside of typical idealisations is investigated. That is, a pendulum of a finite stiffness that interacts in a dissipative manner with its environment. The pendulum is realised as follows. An aqueously-suspended silica micro-bead is constrained within a ring-shaped potential created by rapidly scanning the beam-waist of a focussed Gaussian laser beam to trace out a circle. The beams position is ca

The beam waist is scanned by a pair of orthogonally-mounted galvanometer mirrors. The mirrors allow control of the beam position in the trapping plane in two dimensions. The positions of the mirrors are controlled by a computer; by simply sending a cosine wave to one of the mirrors and a sine wave to the other, it is possible to drive the beam waist in a circle.

Unless any additional force is applied to the system at this point, the bead will diffuse freely about the ring, i.e. the angular probability density function (PDF) will appear flat as $t \to \infty$. The circulation frequency of the scanning laser is orders of magnitude larger than the relaxation frequency of the bead, so the bead is not dragged around the ring. An additional force can be 'switched on' by initiating a

translation of the piezo stage that cradles the sample. This causes fluid to flow across the ring and provides a tunable analog to gravity in the system. The fluid flow will cause the angular PDF to become peaked around the 'bottom' of the ring, that is, at the point on the ring furthest in the direction of fluid flow. Given the over-damped nature of the bead's environment, the bead will come rapidly to equilibrium, unlike the diminishing oscillations about equilibrium that one would expect to see in a typical lightly-damped macroscopic pendulum. In order to add a modulation to the 'suspension point' of the pendulum, a sine wave is superimposed on the position of the centre of the circle, in a direction parallel to the direction of fluid flow.

4.4 Equations of motion

In this section the equations of motion for the over-damped finitely-rigid pendulum are analysed in order to find the conditions of dynamical stability. Firstly, let us consider the four frequencies by which the pendulum can be characterised. We will also discuss how these frequencies are controlled in the experiment.

Pendulum oscillation frequency

The oscillation frequency describes the frequency at which a simple pendulum oscillates about its equilibrium position (i.e. the bottom of the pendulum). As illustrated in figure 4.2, a simple pendulum consists of a mass m suspended by a rigid rod of length L from a pivot point P. We will assume for now that the pendulum is undamped. Newton's second law as applied to a rotating system states

$$\boldsymbol{T} = I\boldsymbol{\alpha}, \tag{4.1}$$

where $\boldsymbol{T}$ is the torque applied to the system, I is the moment of inertia and $\boldsymbol{\alpha}$ is the angular acceleration. The torque is given by

$$\boldsymbol{T} = \boldsymbol{r} \times \boldsymbol{F} \tag{4.2}$$

$$= -FL\sin\theta. \tag{4.3}$$

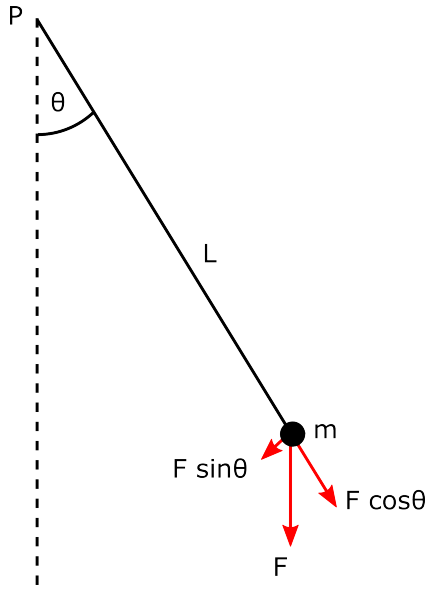

Figure 4.2: A simple pendulum consists of a mass m suspended by a rigid rod of length L from a pivot point P. A force F which acts in the vertical direction can de decomposed into components that act in radial and azimuthal directions.

$F \sin\theta$ is the azimuthal component of the vertically directed force, F. The moment of inertia is $I = mL^2$. Thus, according to equation (4.1),

$$-FL\sin\theta = mL^2\ddot{\theta}, \tag{4.4}$$

which can be re-arranged to show

$$\ddot{\theta} = -\frac{F}{mL}\sin\theta. \tag{4.5}$$

By making the small angle approximation ($\sin\theta \approx \theta$) we can write equation (4.2) as $\ddot{\theta} = -\frac{F}{mL}$, which has the solution

$$\theta = \theta_0 \cos(\Omega t), \tag{4.6}$$

with $\Omega = \sqrt{\frac{F}{mL}}$. We see from equation (4.6) that the angular coordinate of the pendulum θ oscillates with a frequency Ω. We will refer to this frequency as the pendulum's oscillation frequency.

For a typical macroscopic pendulum the force F is the force due to gravity, i.e. $F = mg$. In our system, however, this force is due to the translation of the piezo

stage. The force is proportional to the fluid velocity v_f which, close to the stage, is equal to the velocity at which the stage translates:

$$F = m\gamma_m v_f. \tag{4.7}$$

Experimental control over the oscillation frequency, for a pendulum of given length L, is thus provided by control of the stage translation velocity:

$$\Omega = \sqrt{\frac{\gamma_m v_f}{L}} \tag{4.8}$$

Pendulum modulation frequency

As discussed above, inverted stability can be achieved by modulating the pivot point of the pendulum. The frequency at which this moduluation occurs is the modulation frequency, ω. The modulation frequency is controlled by the galvanometer mirrors that scan the beam waist. The range of frequencies is limited by the operational limits of the mirrors; the upper limit of the mirrors' scan rate is about 1.5 kHz.

N.B. the modulation frequency should be well separated from the scanning frequency of the mirrors (the frequency at which the beam waist is scanned around the circumference of the circular potential). This is to avoid the shape of the potential appearring as a Lissajous curve. In the following analysis we do not consider the scanning frequency of the mirrors. We assume that the potential is an evenly-illumainted ring.

Pendulum proper frequency

If the pendulum rod is not assumed to be infinitely rigid, the radial coordiante of the pendulum's mass can be compared to a mass on a spring, see figure 4.3. The equation of motion for the radial coordinate, assuming the absence of any external forces, is

$$m\ddot{\boldsymbol{r}} = -\gamma\dot{\boldsymbol{r}} - \kappa\boldsymbol{r}, \tag{4.9}$$

where γ is the drag coefficient and κ is the spring constant. If the drag is negligible ($\gamma \to 0$) equation 4.9 has the simple solution $\boldsymbol{r} = \boldsymbol{r}_0 \cos(\omega_0 t)$, where $\omega_0 = \sqrt{\kappa/m}$;

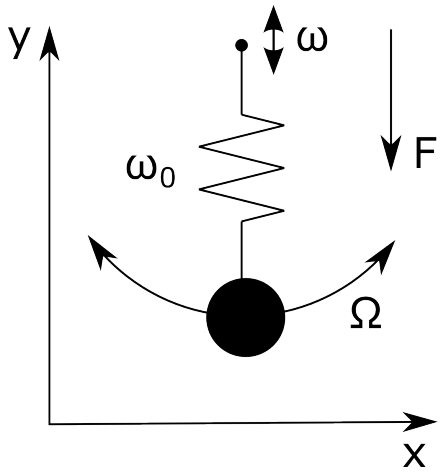

Figure 4.3: In the case of a pendulum with a finitely-rigid rod, the radial coordinate behaves like a mass on a spring with a characteristic 'proper frequency' $\omega_0^2 = \kappa/m$. Also shown are the force F, the oscillation frequency Ω which characterises motion in the azimuthal direction and the modulation frequency ω which characterises the modulation of the pivot point in the y direction.

the radial coordinate oscillates at frequency ω_0. Here this frequency will be referred to as the proper frequency, elsewhere this frequency is sometime referred to as the undamped oscillation frequency. We have experimental control over this frequency via the spring contstant which is proportional to the power of the laser.

Pendulum relaxation frequency

The proper frequency describes the radial motion of the pendulum when damping of the system is negligible. If the damping becomes very large, however, the radial coordinate is unable to oscillate at the proper frequency. Indeed, if the damping becomes large enough the radial coordinate will not oscillate at all: if displaced it will relax exponentially to equilibrium over a characteristic time scale.

To see this, let us return to equation (4.9). In a heavily overdamped system the timescale over which inertial effects take place, $\tau_m = m/\gamma$, is very short. It is therefore reasonable to drop the inertial term $m\ddot{\boldsymbol{r}}$. This leaves us with

$$\dot{\boldsymbol{r}} - \frac{\kappa}{\gamma}\boldsymbol{r}, \tag{4.10}$$

which has the solution

$$\boldsymbol{r} = \boldsymbol{r}_0 \exp(-\tau_0^{-1} t), \tag{4.11}$$

where τ_0^{-1} is the relaxation frequency (or the inverse of the relaxation period) and is given by

$$\tau_0^{-1} = \frac{\kappa}{\gamma} = \frac{m\omega_0^2}{\gamma}. \tag{4.12}$$

The relaxation frequency of the pendulum in our experiment can be controlled through the spring constant κ which, as was mentioned above, is proportional to the power of the laser.

4.4.1 High-frequency regime

Here we consider dynamical stability of the pendulum in a regime where the driving frequency of the suspension point is the largest characteristic frequency of the system:

$$\omega \gg \omega_0; \qquad \omega \gg \tau_0^{-1}; \qquad \omega \gg \Omega. \tag{4.13}$$

In order to maintain pendulum-like behaviour I will assume throughout that $\omega_0 \gg \Omega$. In cartesian co-ordinates, the pendulum's equation of motion is

$$\begin{aligned} m\ddot{x} &= -m\gamma_m\dot{x} - \frac{\partial U}{\partial x}(x, y - y_s(t)), \\ m\ddot{y} &= -m\gamma_m\dot{x} - \frac{\partial U}{\partial y}(x, y - y_s(t)) - F, \end{aligned} \tag{4.14}$$

where $\gamma_m = 6\pi\eta r/m$ is the mass-normalised friction coefficient (we will later see that it is convenient to have friction expressed in units of frequency), $U(x, y)$ is the pendulum potential, F is the pendulum confining force (i.e. gravity in a typical pendulum or the viscous drag force, $F = m\gamma_m v$, in our experiment) and y_s represents the vibration of the pendulum suspension point:

$$y_s(t) = -a\cos(\omega t + \varphi_0), \tag{4.15}$$

where a, ω and φ_0 are the driving amplitude, frequency and phase respectively. I will assume a quartic form for the pendulum potential,

$$U(x,y) = \frac{U_0}{L^4}(x^2+y^2)(x^2+y^2-2L^2), \tag{4.16}$$

where L represents the length of the pendulum's 'rod', or in our experiment the radius of the circular potential. I choose this form because it captures the main features of the pendulum whilst being amenable to analytic manipulation. The potential is illustrated in figure 4.4 for a length $L = 1$. The circular symmetry of the potential is apparent.

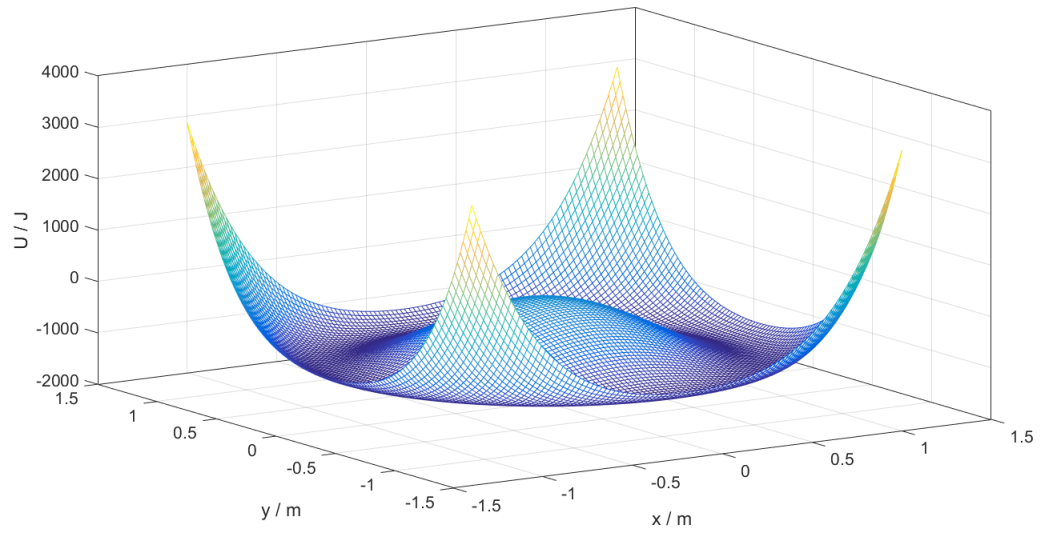

Figure 4.4: Three-dimensional plot of the pendulum potential described by equation (4.16) for $a = 0$ and $L = 1$. The potential is circularly symmetric in the $x - y$ plane, with a minimum at $x = y = L$.

It would be helpful at this point to analyse the potential terms in equation (4.14) in order to find the equilibrium positions of the pendulum. We would find, however, that this task is complicated by the explicit time-dependence of the $y_s(t)$ terms. One way to overcome this difficulty is to consider separately the different time-scales of the system. Since I am assuming the driving frequency to be large in comparison with all other frequencies in the system we can expect the overall motion of the pendulum to be a combination of two separate motions: one that is a small-amplitude, high-frequency oscillation; and another that is slower and smoother.

Separating the time-scales and averaging over the period of the fast oscillation will lead us to an approximate, time-independent, *effective* potential for the smooth motion of pendulum, whose equilibrium points can be more easily calculated. This approach is credited to Kapitza by Landau & Lifshitz in their textbook of 1960 [**?**] (Kapitza's original paper is in Russian [49]).

Let us proceed by calculating the average of equation (4.14) by integrating over the period of the driving frequency, $T = 2\pi/\omega$ and dividing by that period. The co-ordinates $x(t)$ and $y(t)$ change on a much longer timescale than the driving frequency and can considered constant over the period, T. The integration yields the following equation

$$\begin{aligned} m\ddot{x} &= -m\gamma\dot{x} - \frac{\partial U_{eff}}{\partial x}(x,y), \\ m\ddot{y} &= -m\gamma\dot{y} - \frac{\partial U_{eff}}{\partial y}(x,y) - F, \end{aligned} \tag{4.17}$$

where

$$U_{eff}(x,y) = \langle U(x, y - y_s(t))\rangle = \frac{1}{T}\int_0^T U(x, y - y_s(t))dt. \tag{4.18}$$

Written out in full, $U(x, y - y_s(t))$ is equal to

$$\frac{U_0}{L^4}\left[x^4 + (y - y_s(t))^4 + 2x^2(y - y_s(t))^2 - 2x^2L^2 - 2(y - y_s(t))^2L^2\right]. \tag{4.19}$$

We need, therefore, to find the time-average of this equation. The average of the $(y - y_s(t))^2$ term is

$$\begin{aligned} \langle (y - y_s)^2\rangle &= \langle y^2 - 2ya\cos(\omega t + \varphi_0) + a^2\cos^2(\omega t + \varphi_0)\rangle, \\ &= y^2 + \frac{a^2}{2}, \end{aligned} \tag{4.20}$$

since

$$\langle\cos(t)\rangle = \frac{1}{T}\int_0^T \cos^n(t)dt = 0, \tag{4.21}$$

when n is odd, and

$$\langle\cos^2(t)\rangle = \frac{1}{T}\int_0^T \cos^2(t)dt = \frac{1}{2}. \tag{4.22}$$

The average of the $(y - y_s(t))^4$ term is

$$\begin{aligned}\langle (y-y_s)^4 \rangle &= \langle y^4 + 4y^3 a\cos(\omega t+\varphi_0) + 6y^2a^2\cos^2(\omega t+\varphi_0) \\ &\quad + 4ya^3\cos^3(\omega t+\varphi_0) + a^4\cos^4(\omega t+\varphi_0)\rangle, \\ &= y^4 + 3y^2a^2 + \frac{3a^4}{8},\end{aligned} \tag{4.23}$$

since

$$\langle \cos^4(x)\rangle = \frac{1}{T}\int_0^T \cos^4(t)dt = \frac{3}{8}. \tag{4.24}$$

Therefore, the effective potential is

$$\begin{aligned}U_{eff} &= \frac{U_0}{L^4}\left[x^4 + y^4 + 3y^2a^2 + \frac{3a^4}{8} + 2x^2y^2 + x^2a^2 - 2x^2L^2 - 2y^2L^2 - a^2L^2\right] \\ &= \frac{U_0}{L^4}\left[(x^2+y^2)(x^2+y^2-2L^2) + a^2(x^2+3y^2) + \frac{3a^4}{8} - a^2L^2\right] \\ &= U(x,y) + \frac{U_0}{L^4}\left[a^2(x^2+3y^2) + \frac{3a^4}{8} - a^2L^2\right].\end{aligned} \tag{4.25}$$

Defining $\omega_0^2 = (8U_0)/(mL^2)$, where ω_0 is the pendulum's proper frequency, we can write equation (4.25) as

$$U_{eff} = U(x,y) + \frac{1}{8}m\omega_0^2\left(\frac{a}{L}\right)^2(x^2+3y^2), \tag{4.26}$$

where I have discarded the constant terms $3a^4/8$ and a^2L^2 since they do not contribute to the equation of motion of the system, which concerns the gradient of this potential.

As we set out to achieve, we have found a time independent form of the system's potential. Now, I calculate the positions of the potential minima following the standard approach: by taking derivatives with respect to x and y, setting the result equal to zero and re-arranging for the position. Doing so first with respect to y we have

$$\frac{\partial}{\partial y}(U_{eff} - Fy) = m\omega_0^2 y\left[1 - \frac{L}{\sqrt{x^2+y^2}} + \frac{3a^2}{4L^2}\right] - F = 0, \tag{4.27}$$

which can be re-arranged to show

$$y = \frac{2F}{m\omega_0^2}\frac{L^2}{a^2} = 2L\frac{\Omega^2}{\omega_0^2}\frac{L^2}{a^2}, \tag{4.28}$$

where I have defined the pendulum's oscillation frequency $\Omega = \sqrt{F/(mL)}$. The derivative with respect to x is

$$\frac{\partial U_{eff}}{\partial x} = m\omega_0^2 x\left[1 - \frac{L}{\sqrt{x^2+y^2}} + \frac{a^2}{4L^2}\right] = 0, \tag{4.29}$$

which can be re-arranged as

$$x = \left[\frac{1}{1+a^2/(4L^2)}\right]^2 - y^2 \simeq \pm L\sqrt{1 - \frac{a^2}{2L^2} + 4\frac{\Omega^4}{\omega_0^4}\frac{L^4}{a^4}}, \tag{4.30}$$

where the term in square brackets has been expanded up to the second order in Taylor series. For a pendulum of fixed length, L, stiffness, ω_0, and oscillation frequency, Ω, the position of stability is dependent upon the driving amplitude a. The bottom of the pendulum $(0, L)$ is stable for driving amplitudes in the range $0 < a < a_1$ where

$$a_1 = \sqrt{2}L\frac{\Omega}{\omega_0}. \tag{4.31}$$

This can be seen in figure 4.5 where a closed contour indicates a minimum in the potential. In the range $a_1 < a < a_2$ the equilibrium positions are given by equations (4.30) and (4.28), where $a_2 = \sqrt{2}L$. These equilibrium positions can be expressed in terms of an angular coordinate θ whose origin is at the suspension point of the pendulum:

$$\theta = \arccos\left(2\frac{\Omega^2}{\omega_0^2}\frac{L^2}{a^2}\frac{1}{\sqrt{1-\frac{a^2}{2L^2}}}\right). \tag{4.32}$$

Figure 4.6 illustrates stability in the effective potential for this range of driving amplitude. If $a > a_2$ the equilibrium point is where $x = y = L\Omega^2/\omega_0^2 \simeq 0$, since $\omega_0^2 \gg \Omega^2$. This is illustrated in figure 4.7.

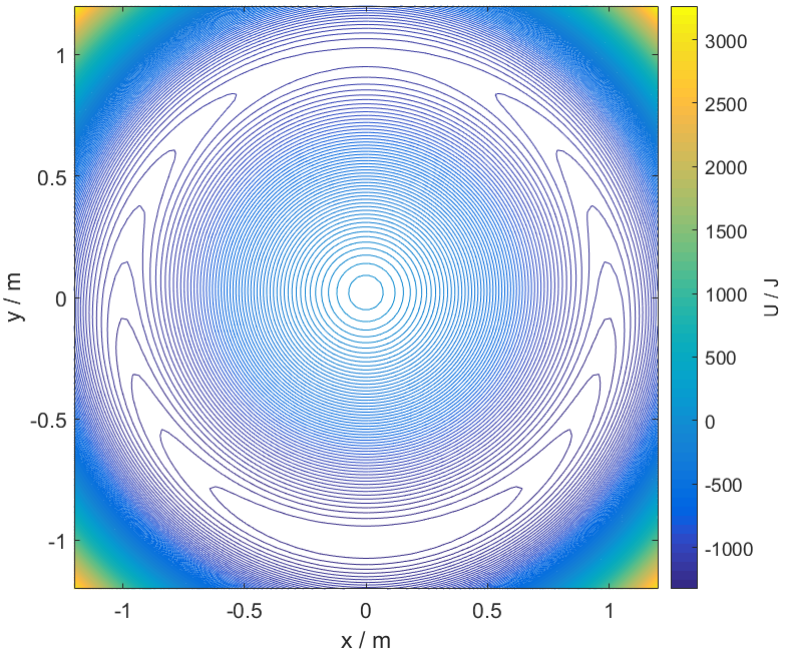

Figure 4.5: Contour plot of U_{eff} when $0 < a < a_1$. Fluid flow is in the negative y direction. The parameters of the potential in this figure are as follows: $a = 0$; $L = 1$; $F = 100$; $\Omega = 10$; $\omega_0 = 100$.

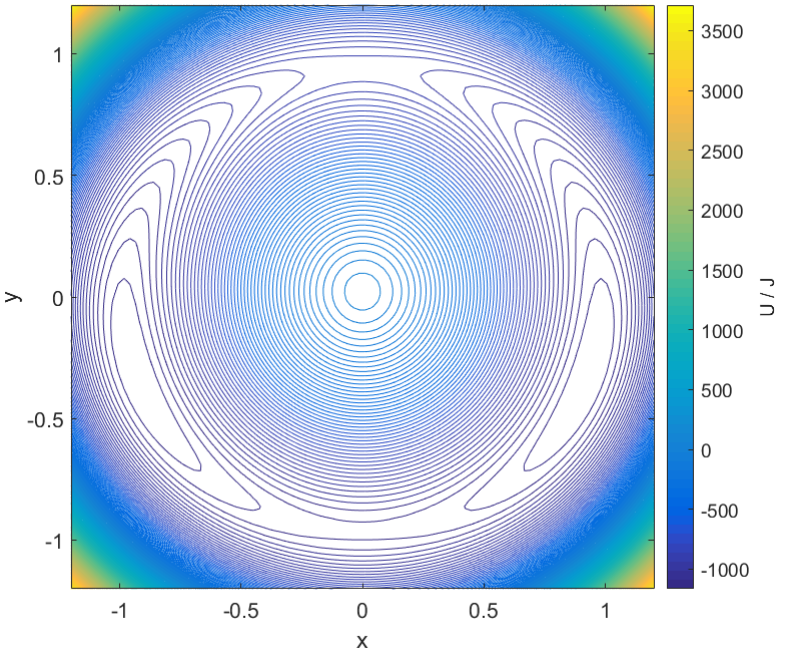

Figure 4.6: Contour plot of U_{eff} when $a_1 < a < a_2$. Fluid flow is in the negative y direction. The parameters of the potential are as in figure 4.5, but $a = 0.25$.

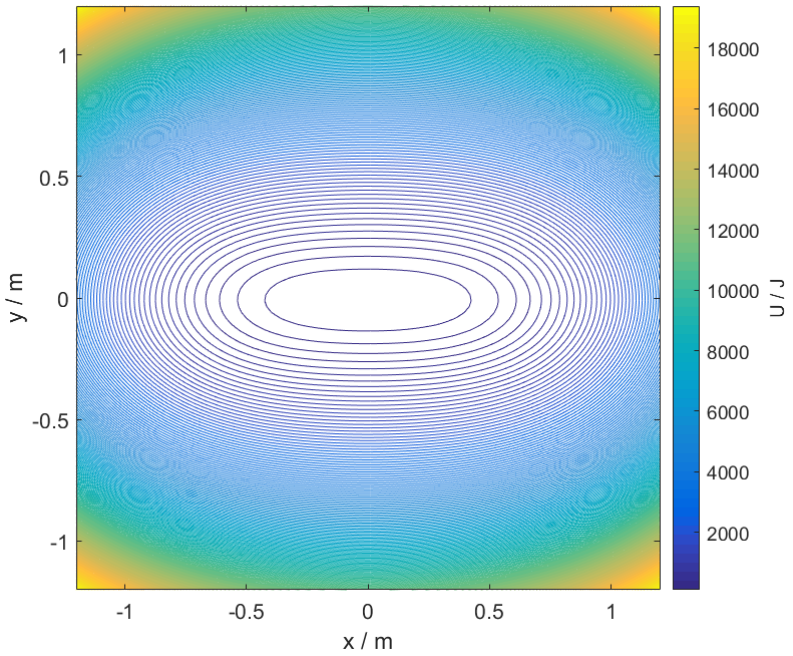

Figure 4.7: Contour plot of U_{eff} when $a > a_2$

Conceptual understanding

A conceptual understanding of the different equilibrium positions can be developed by considering the balance of intensity gradients and the drag force due to fluid flow in the experiment. Let us the following scenarios:

(i) Without fluid flow or ring modulation, a particle trapped in the ring shaped potential will diffuse freely around the ring. This is illustrated in figure 4.4, where the minimum in potential (or the peak in optical intensity) is located about the circumference of the ring.

(ii) With fluid flow but no ring modulation, a particle trapped at the ring's circumference will become localised in the downstream direction. This is illustrated in figure 4.5.

(iii) Without fluid flow but with ring modulation, the time-averaged potential will has spots of greatest intensity at $\pi/2$, either side of the bottom of the pendulum. This is illustrated in figure 4.8.

(iv) With both fluid flow and ring modulation, the equilibrium position is found

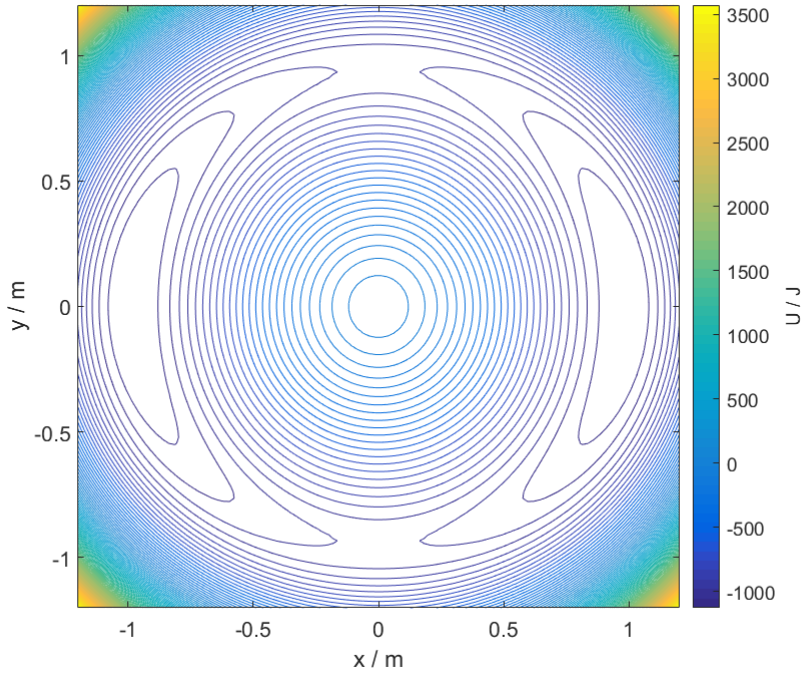

Figure 4.8: Contour plot of U_{eff} when $a_1 < a < a_2$ with no fluid flow

where the force due to the peaks in intensity are balanced by the force due to the fluid flow. As the velocity of the fluid flow increases, the point at which the forces balance mover further downstream.

Limits on pendulum rigidity

It should be noted that none of the equilibrium points discussed above are associated with the inverted stability discussed in the introduction. In the following section we place a limit on the rigidity of the pendulum in relation to the other characteristic frequencies of the system. We will see that doing so allows the pendulum to enter equilibrium in the inverted position.

4.4.2 Low-frequency regime

Now I consider dynamical stability of the pendulum in a regime where the proper frequency of the pendulum is larger than the modulation frequency.

Imposing the condition that the proper frequency is larger than the modulation frequency necessarily implies that the relaxation frequency is also larger than

modulation frequency (if γ_m/ω_0 is constant):

$$\omega \ll \omega_0; \qquad\qquad \omega \ll \tau_0^{-1} = \frac{\omega_0^2}{\gamma_m}. \tag{4.33}$$

This is equivalent to $\omega_0 \to \infty$ while keeping γ_m/ω_0 constant.

It is convenient to convert our equations of motion in the previous section (equation 4.14) to polar coordinates (see Appendix A):

$$r\ddot{\theta} + 2\dot{r}\dot{\theta} + \gamma_m r\dot{\theta} = -\frac{F}{m}\sin\theta - \ddot{y}_s \sin\theta - \gamma_m \dot{y}_s \sin\theta \tag{4.34}$$

$$\ddot{r} + \gamma\dot{r} + \omega_0^2 r = \omega_0^2 L + r\dot{\theta}^2 + \frac{F}{m}\cos\theta + \ddot{y}_s\cos\theta + \gamma\dot{y}_s\cos\theta \tag{4.35}$$

where θ is measured from the bottom of the pendulum (i.e. $\theta = 0 = 2\pi$ is the bottom of the pendulum, $\theta = \pi$ is the top).

Assuming that changes to r are small, we can approximate the potential term in equation (4.35) by its linear form (given by the first term in the Taylor expansion):

$$\frac{m\omega_0^2 r}{2L^2}(r^2 - L^2) \simeq -m\omega_0^2(r - L). \tag{4.36}$$

Then, following the details given in appendix B, we can write an approximate solution to equation (4.35):

$$r(t) \approx L + \frac{1}{\omega_0^2}\left(\ddot{y}_s + \gamma_m\dot{y}_s\right)\cos\theta. \tag{4.37}$$

Our next step is to substitute equation (4.37) into equation (4.34):

$$\begin{aligned}\left(L + \frac{1}{\omega_0^2}\left(\ddot{y}_s + \gamma_m\dot{y}_s\right)\cos\theta\right)\left(\ddot{\theta} + \gamma_m\dot{\theta}\right)& \\ +2\dot{\theta}\frac{\partial}{\partial t}\left(L + \frac{1}{\omega_0^2}\left(\ddot{y}_s + \gamma_m\dot{y}_s\right)\cos\theta\right)& \\ = -\frac{F}{m}\sin\theta - \ddot{y}_s\sin\theta - \gamma_m\dot{y}_s\sin\theta.&\end{aligned} \tag{4.38}$$

In the limit $\omega_0 \to \infty$, while keeping γ_m/ω_0 constant, equation 4.38 reduces to

$$\ddot{\theta} = -\gamma_m\dot{\theta} - \left(\frac{\gamma_m}{\omega_0}\right)^2 \frac{\dot{y}_s}{L}\dot{\theta}\cos\theta - \Omega^2\sin\theta - \frac{\dot{y}_s}{L}\sin\theta - \frac{\gamma_m\ddot{y}_s}{L}\sin\theta, \tag{4.39}$$

where we have employed the fact that $\Omega^2 = F/(mL)$. Next, we will average over the timescale of the fast moving oscillations. To facilitate this, I write our angular variable $\theta(t)$ as a combination of a 'fast' variable $\delta(t)$ and a 'smooth' variable $\psi(t)$: $\theta(t) = \psi(t) + \delta(t)$. The fast variable is due to the oscillation of the pivot point, thus $\delta(t) = -(y_s/L)\sin\psi$. We assume that the angular deflection $\delta(t)$ is small and that over the period of the fast oscillation the change to the slow variable is negligible. After substituting these new variables into equation (4.39) and expanding $\sin(\psi+\delta)$ and $\cos(\psi+\delta)$ under the small-angle approximation, we find:

$$\begin{aligned}\ddot{\psi} + \ddot{\delta} + \gamma_m(\dot{\psi}+\dot{\delta}) = &-\left(\gamma_m\frac{\dot{y}_s}{L} + \Omega^2 + \frac{\ddot{y}_s}{L}\right)(\sin\psi + \delta\cos\psi) \\ &-\left(\frac{\gamma_m}{\omega_0}\right)^2\frac{\dot{y}_s}{L}(\dot{\psi}+\dot{\delta})(\cos\psi - \delta\sin\psi).\end{aligned} \tag{4.40}$$

Several of the terms on the left- and right-hand side of equation (4.40) are equal:

$$\ddot{\delta} = -\frac{\ddot{y}_s}{L}\sin\psi;$$
$$\gamma_m\dot{\delta} = -\frac{\gamma\dot{y}_s}{L}\sin\,.$$

After removing these terms, we average over the period of δ (see appendix C for details) to find:

$$\ddot{\psi} + \gamma_m\dot{\psi} = -\Omega^2\sin\psi - \frac{a^2\omega^2}{4L^2}\sin 2\psi\left(1 - \frac{\gamma_m^2}{\omega_0^2}\right). \tag{4.41}$$

The right-hand-side of this equation can be equated to the gradient of the effective potential

$$\frac{1}{m}\frac{dV_{eff}}{d\psi} = -\Omega^2\sin\psi - \frac{a^2\omega^2}{4L^2}\sin 2\psi\left(1 - \frac{\gamma_m^2}{\omega_0^2}\right). \tag{4.42}$$

Integrating, we find

$$V_{\text{eff}}(\psi) = -m\Omega^2 \left[\cos\psi - \frac{1}{8}\left(\frac{\omega}{\Omega}\right)^2 \left(\frac{a}{L}\right)^2 \left(\frac{\gamma_m^2}{\omega_0^2} - 1\right) \cos 2\psi\right], \tag{4.43}$$

We can write this in a more succinct form,

$$V_{\text{eff}}(\psi) = -m\Omega^2 \left[\cos\psi + \frac{\Lambda}{4}\cos 2\psi\right], \tag{4.44}$$

by defining

$$\Lambda = \frac{1}{2}\left(\frac{a}{L}\right)^2 \left(\frac{\omega}{\Omega}\right)^2 \left(1 - \frac{\gamma_m^2}{\omega_0^2}\right). \tag{4.45}$$

Analysis of the potential reveals three distinct sub-regimes of stability.

- If $\Lambda > 1$, potential minima are present at 0, π and 2π, i.e. both the top (true inverted stability) and bottom of the pendulum are stable. The inequality $\Lambda > 1$ that defines this regime may also be written with respect to the friction coefficient: $0 < \gamma_m < \gamma_{m,1}$, where

$$\gamma_{m,1} = \omega_0 \sqrt{1 - 2\left(\frac{\Omega/\omega}{a/L}\right)}. \tag{4.46}$$

- If $-1 < \Lambda < 1$, the minimum at π is no longer present, i.e. only the bottom of the pendulum is stable. Again, the requirements for this regime can be written with respect to the friction coefficient: $\gamma_{m,1} < \gamma_m < \gamma_{m,2}$, where

$$\gamma_{m,2} = \omega_0 \sqrt{1 + 2\left(\frac{\Omega/\omega}{a/L}\right)}. \tag{4.47}$$

- If $\Lambda < -1$, the position of the potential minimum is given by

$$\psi = \arccos(-1/\Lambda). \tag{4.48}$$

  In terms of the friction coefficient, this regime is defined as $\gamma_{m,2} < \gamma_m$.

The three regimes of stability are illustrated in figure (4.9). The condition for the

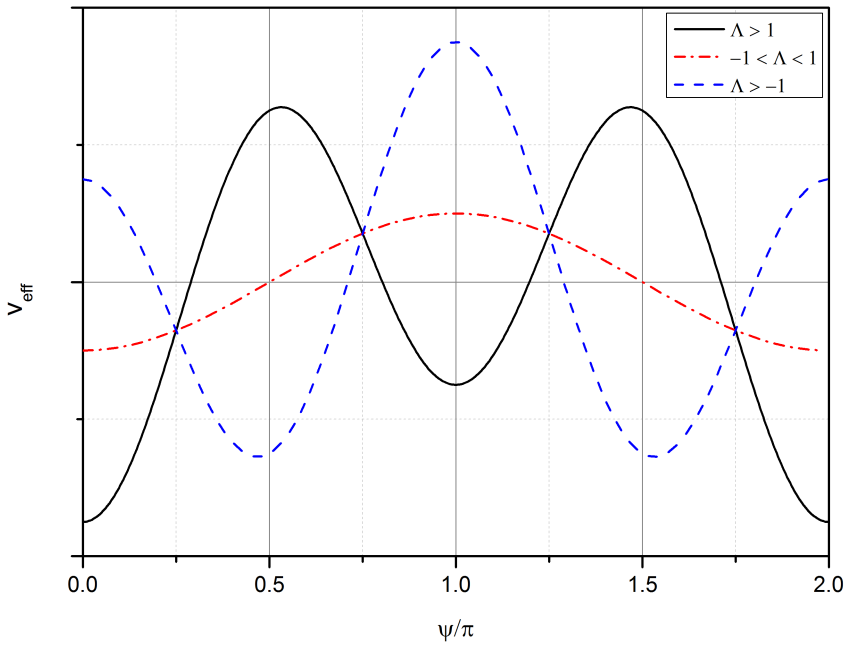

Figure 4.9: Effective potential in the low-frequency regime as a function of angle (meausred from upright position). For $\Lambda > 1$, there are potential minima at 0, π and 2π. For $-1 < \Lambda < 1$, there are potential minima only at 0 and 2π. For $\Lambda < -1$, 0, π and 2π are all unstable. In this sub-regime, stability angle is given by equation (4.48).

last of these sub-regimes ($\Lambda < -1$) can be expressed as

$$a > -\sqrt{2}L\frac{\Omega}{\omega}\left(\frac{\gamma_m^2}{\omega_0^2} - 1\right)^{-1/2}, \tag{4.49}$$

and we see that for a given pendulum - with a fixed Ω, ω, γ_m, ω_0 and L - there is a threshold for driving amplitude above which the stability position is given by equation (4.48). This equation for stability angle in the low-frequency regime bears some similarity to the corresponding equation in the high-frequency regime, equation (4.32). In both regimes the stability angle is dependent on the driving amplitude a. However, in the low-frequency regime the stability angle is additionally dependent on the driving frequency ω and the friction coefficient γ_m.

4.5 Chapter summary

To summarise this chapter, I have described a microscopic optical pendulum and presented a mathematical analysis of dynamical stability in such a pendulum. The pendulum is based on a ring-shaped potential that is created by the rapid scanning of an optical tweezers; the position of the centre of the ring is then oscillated. A quartic potential was chosen as a model for the potential. In order to assess the potential minima an effective potential was calculated by finding the potential average over a complete cycle of an oscillation. This analysis was undertaken in two regimes: firstly, a regime in which the oscillation frequency is the largest frequency in the system; secondly, a regime in which the proper frequency (the frequency describing the rigidity of the pendulum) exceeds the modulation frequency. In both regimes it is found that, given appropriate amplitude of the oscillation, dynamical stabilisation is possible and that the position of stability depends is a function of the amplitude. In the second regime, it is found that the stability position is also a function of the oscillation frequency. Figure 4.10 illustrates the different regimes of the pendulum as a function of both friction and modulation frequency.

In the following chapter I will present simulations and experiments that test these theoretical predictions.

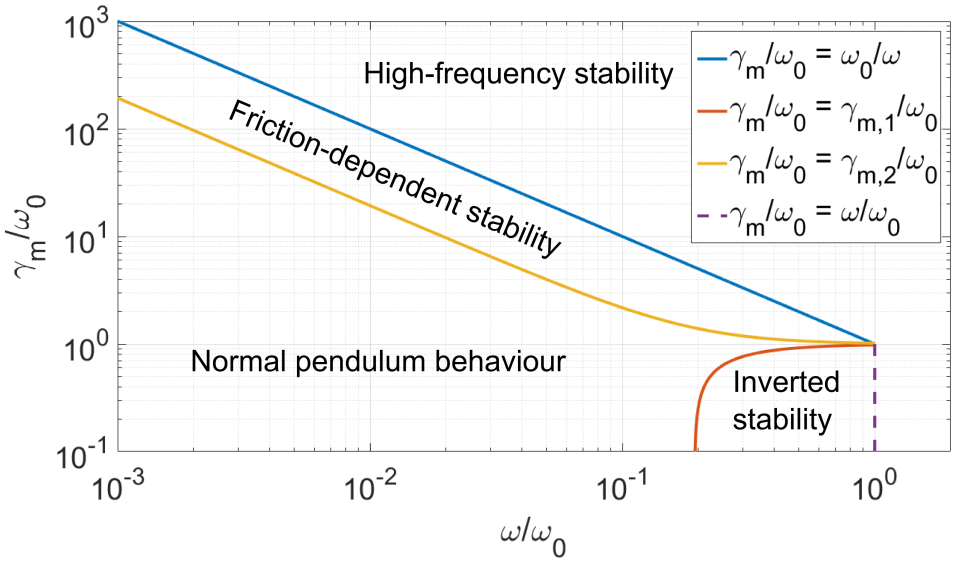

Figure 4.10: A parameter space diagram to illustrate the regimes of stability for a pendulum with varying modulation frequency, ω, and friction coefficient, γ_m. For modulation frequencies larger than ω_0^2/γ_m, the pendulum is in the 'high-frequency' regime and the stability positions are dictated by equation (4.32). For modulation frequencies smaller than ω_0^2/γ_m, the pendulum is in the 'low-frequency' regime. This regime has three sub-regimes: a 'normal pendulum' regime ($\gamma_{m,1} < \gamma_m < \gamma_{m,2}$), in which only the bottom of the pendulum is stable; an 'inverted pendulum' ($0 < \gamma_m < \gamma_{m,1}$), in which the top of the pendulum is also stable; and a 'friction-dependent' regime ($\gamma_{m,2} < \gamma_m$ with $\gamma_m/\omega_0 < \omega_0/\omega$) in which the stability position is dependent on the friction coefficient and the driving frequency and is dictated by equation (4.48).

Chapter 5

Dynamical stabilisation: simulations, experiments and discussion

5.1 Introduction

In this chapter the different regimes of dynamical stability predicted in the previous chapter for an over-damped finitely-rigid pendulum are tested through simulations and experiments. The chapter proceeds as follows: in section 5.2, I describe the experimental set-up and procedure; section 5.3 contains results from finite-difference simulations of the experiment; and section 5.4 contains experimental results.

5.2 Experimental set-up and procedure

An outline of the experimental realisation of the pendulum was given in section 4.3. Here, that outline is filled in with some detail of the apparatus and procedure.

5.2.1 Experimental set-up

Figure 5.1 diagrammatically depicts the set-up. A Nd:YAG 1064nm laser beam is expanded by a pair of telescoping mirrors to overfill the back aperture of a 100x NA

= 1.3 oil-immersion microscope objective (MO), which brings the beam to focus at the trapping plane. A microscope slide, containing silica micro-spheres of 1.5µm diameter suspended in water, is placed in the trapping plane. The spheres (Kisker Biotech) are monodisperse, have a density $2\,\mathrm{g}\cdot\mathrm{cm}^{-1}$ and a refractive index of $1.43-1.46$ at 589 nm [**?**]. A lamp illuminates the trapping plane, whose image is focused onto a digital camera. The laser beam, before being expanded, travels via a pair of orthogonally-mounted galvanometer mirrors (GM). The mirrors allow control of the beam position in the trapping plane in two dimensions. The positions of the mirrors are controlled by a computer, so by simply sending a cosine wave to one of the mirrors and a sine wave to the other it is possible to drive the beam waist in a circle. If the waist is scanned rapidly we create a circular time-averaged potential in the trapping plane for the micro-spheres. The beam is scanned around the circumference of the circle at a rate of 1.2kHz. The largest pendulum relaxation frequency (effectively the relaxation frequency of the bead in the circular potential) used in the experiments is about 24Hz. This being two orders of magnitude smaller than the beam-scanning frequency, we can be quite confident that the scanning-beam does not drag the particle around the circle. The pendulum confining force F is provided by translating the sample relative to the centre of the circular potential, causing fluid to flow across the ring. This is implemented by a computer-controlled piezo-stage. Modulation of the pendulum is achieved by superimposing a sine wave on the centre of the potential, in a direction parallel to the ring.

5.2.2 Control of the system frequencies

In section **??**, the four characteristic frequencies of the pendulum were outlined. Here I explain how these frequencies are controlled in the experiment and how this gives control over the regime that we are working in. The modulation frequency of the suspension point, ω, is controlled by the scanning galvanometer mirrors and can be arbitrarily selected between 0Hz and the largest working frequency of the mirrors, which is about 1.5kHz. The pendulum's oscillation frequency, Ω, is dependent on the ratio of the confining force, F, to the length of the pendulum, L: $\Omega = \sqrt{F/L}$. The confining force in the experiments is equal to the viscous drag force provided

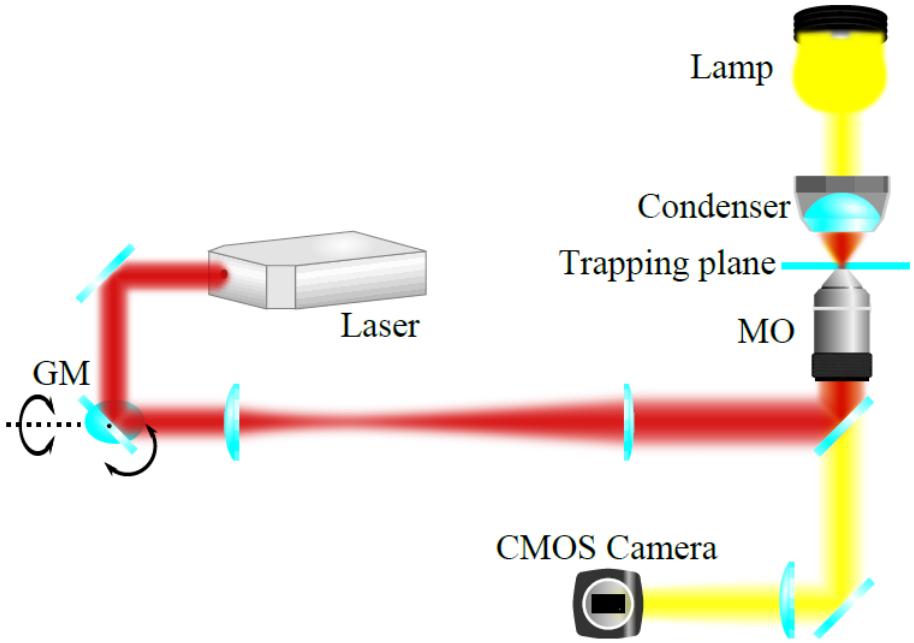

Figure 5.1: Optical tweezers set-up used to experimentally realise an over-damped, finitely-rigid pendulum. Laser is expanded by a pair of telescoping lenses (L1 & L2) to overfill the back aperture of a microscope objective (MO). The objective lens focusses the beam to a diffraction limited spot at the trapping plane, where the sample is placed. The sample is illuminated and its image is focussed onto a digital camera.

by the fluid, thus the oscillation frequency is determined by

$$\Omega = \sqrt{\frac{\gamma_m v_f}{mL}}, \tag{5.1}$$

where v_f is the velocity of the fluid, which is equal to the velocity at which the piezo stage is translated. The pendulum's proper frequency, ω_0, is dependent on the radial spring constant felt by the sphere trapped in the circular potential, κ_ρ, and the mass of the trapped sphere:

$$\omega_0 = \sqrt{\frac{\kappa_\rho}{m}}. \tag{5.2}$$

The pendulum's relaxation frequency is given by

$$\tau_0^{-1} = \frac{\kappa_\rho}{m\gamma_m}. \tag{5.3}$$

The system can be placed into either the high-frequency regime or low-frequency regime by a choice of experimental parameters. If the ratio ω_0^2/γ_m exceeds the modulation frequency, the system is in the low-frequency regime. Conversely, if the modulation frequency exceeds ω_0^2/γ_m, the system is in the high-frequency regime. For a given particle suspended in a given fluid, control over the regime is provided by our choice of modulation frequency and the spring constant κ_ρ which, for a given radius of circle, is set by the laser power.

5.2.3 Procedure and data extraction

In a typical experiment, the micro-sphere is initially held in a static optical trap. The trapping plane is typically positioned about 10µm above the cover slip of the sample to minimise interaction between the sphere and the surface [**?**]. When the experiment begins, the stage translation is initiated and the beam waist begins its rapid scan around the ring of the pendulum (and superimposed modulation). The bead is driven around the ring by the fluid flow and depending on the experimental parameters (modulation amplitude, stage translation velocity, etc.) will come to a stable equilibrium at a particular point on the ring. Video recordings of the exper-

iment are processed by a particle tracking algorithm to reconstruct the trajectory of the bead. The particle tracking works by applying a threshold to each frame of the video, forming a binary image in which objects that stand out against the background (i.e. the micro-sphere) become a region of pixels with value '1' against background pixels which are assigned a value of '0'. The centroid of the regions of '1's can then be taken as the micro-sphere's position.

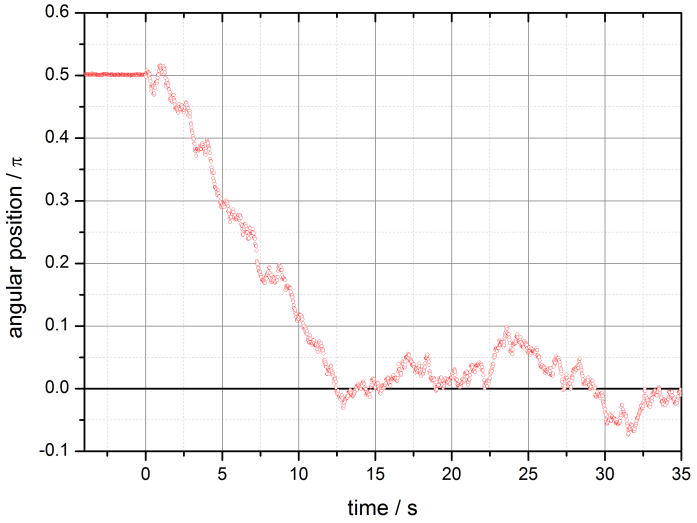

Figure 5.2: Evolution of a particle's angular position in pendulum subjected to no modulation. The particle is clearly in stable equilibrium around $\psi = 0$, represents the 'bottom' of the pendulum.

Figure 5.2 shows the (experimental) trajectory of a micro-sphere when there is no modulation applied to the pendulum. The sphere is initially positioned at $\psi = \pi/2$. At time $t = 0$ the experiment begins and the sphere moves around the circular potential from its initial position to the 'bottom' of the pendulum ($\psi = 0$). Figure 5.3 shows the trajectory of a sphere when the pendulum is subjected to a modulation of $a/L = 0.4$. As can be seen in the figure, the sphere comes to equilibrium away from the bottom of the pendulum. It should be noted that the initial angle of the sphere is greater than in the previous run to allow the relaxation of the sphere toward the equilibrium position to be monitored. In order to extract the stability

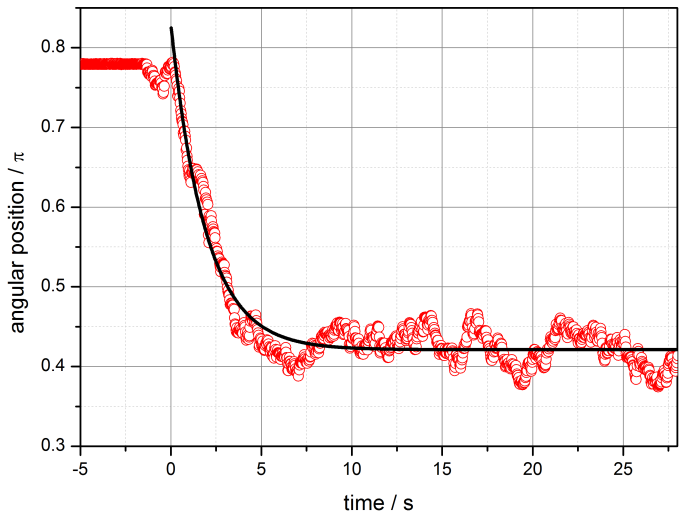

Figure 5.3: Evolution of a particle's angular position in pendulum subjected to a modulation with amplitude above the threshold expressed in equation (4.31). Dashed line represents the stability angle predicted in equation (4.32).

angle from the trajectory, a function with the following form is fitted to it:

$$\psi = \psi_s + \psi_i \exp\left[-t/\tau_\psi\right], \tag{5.4}$$

where ψ_i is the initial angle, ψ_s is the stability angle and τ_ψ is the characteristic relaxation time of the micro-sphere toward the stable position. Such a fit can be seen in figure 5.3. By repeating this procedure at a range of modulation amplitudes values, the dependence of the stability angle on the modulation amplitude can be explored. The results can be compared to the predictions of equations (4.32) in the high-frequency regime and (4.48) in the low-frequency regime.

5.3 Simulations

Carrying out finite-difference simulations of the experiment provides an efficient means for testing the viability of potential experimental parameters. A description of the finite-difference simulation method was given in section 3.8. Here, the circularly shaped potential means that the particle is subjected to a trapping force in the radial direction (with respect to the centre of the potential). This is reflected in the

simulation code used here.

An example of a simulated trajectory, based on the following parameters, can be seen in figure 5.4.

- particle radius, $r = 0.75\mu\text{m}$;
- particle mass, $m = 4.68 \times 10^{-15}\text{m}$;
- fluid viscosity (water), $\eta = 0.088 \times 10^{-3}\text{Pa} \cdot \text{s}$;
- fluid velocity, $v_f = 0.75\mu\text{m} \cdot \text{s}^{-1}$;
- pendulum length (circle radius), $L = 8\mu\text{m}$;
- modulation amplitude, $a/L = 0.3$;
- mass-normalised friction coefficient, $\gamma_m = 6\pi\eta r/m = 2.66\text{MHz}$;
- radial spring constant, $\kappa_\rho = 0.3\text{pN} \cdot \mu\text{m}^{-1}$;
- pendulum proper frequency, $\omega_0 = \sqrt{\kappa_\rho/m} = 2\pi \times 1274\text{Hz}$;
- modulation frequency, $\omega = 2\pi \times 500\text{Hz}$;
- oscillation frequency, $\Omega = \sqrt{\gamma_m v_f/L} = 2\pi \times 79\text{Hz}$;

The plots in figure 5.4 show that the particle finds a stable position away from the bottom of the circle. This follows the predictions made in the previous chapter. For this set of parameters, the ratio ω_0^2/γ_m is equal to $2\pi \times 3.8\text{Hz}$, which is exceeded by the modulation frequency, ω. The system is therefore in the high-frequency regime. In this regime, stability away from the bottom of the pendulum occurs for a modulation amplitude above the threshold amplitude given in equation (4.31):

$$\frac{a_1}{L} = \sqrt{2}\frac{\Omega}{\omega_0} \simeq 0.09. \tag{5.5}$$

The modulation amplitude used in the simulation, $a/L = 0.3$, exceeds this threshold value. Hence, stability away from the bottom of the pendulum is seen.

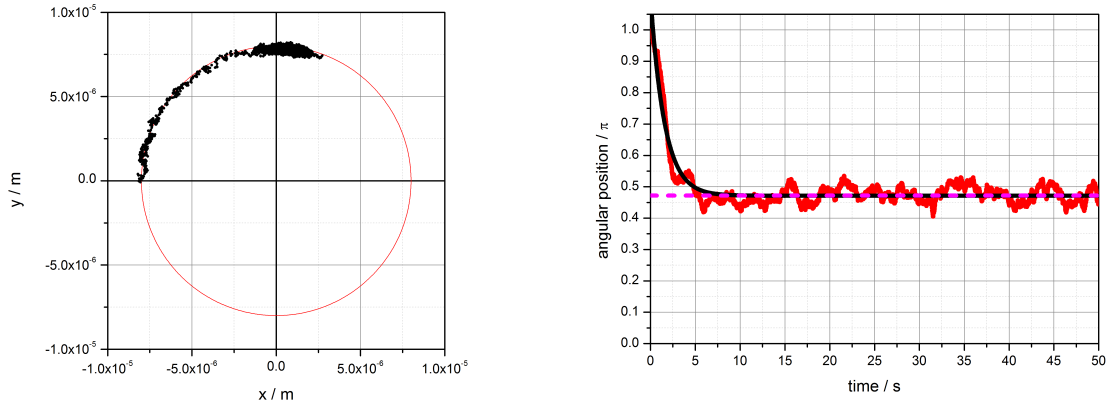

(a) **(b)**

Figure 5.4: Example of a simulated trajectory in the high frequency regime. The modulation amplitude, $a/L = 0.3$, is above the threshold value - see equation (4.31) - so the stability angle is away from zero. **(a)** Black dots represent position of the particle, red line represents the position of the circle at $t = 0$. Fluid flows from left to right. Initial particle position is $(x, y) = (-L, 0)$. The particle moves clockwise around the circle until it finds stability close to $\pi/2$. **(b)** Red dots represents the angular position of the simulated particle against time. Dashed magenta line represents the stability angle predicted by equation (4.32). Solid black line represents a fit, of the type in equation (5.4), to the angular position of the particle.

The dashed magenta line in figure 5.4(b) represents the stability angle predicted by equation (4.32). A good agreement between the simulated trajectory and the prediction is clear. Indeed, equation (4.32) predicts a stability angle of $\psi = 0.4718 \times \pi$ and the stability angle found from a fit - of the form in equation (5.4) - to the trajectory is $\psi_s = 0.48410 \pm 0.00005 \times \pi$.

Figure 5.5 shows the stability angles found for a range of modulation amplitudes: $a/L = 0 \rightarrow 0.5$. Each point is the mean of at least five trajectories and the error bars represent the standard deviation of the mean. The red line represents the stability angle predicted by equation (4.32). The graph illustrates a good agreement between theory and simulated results. Below the threshold modulation, of $a/L = 0.09$, the simulated particles find stability around $\psi = 0$. In this region, the error bars are notably larger than at larger driving amplitudes. This is likely due to the fact that the gradient of the potential increases as the ratio a/L increases; as the ratio increases the confinement of the particle at the stability angle also increases.

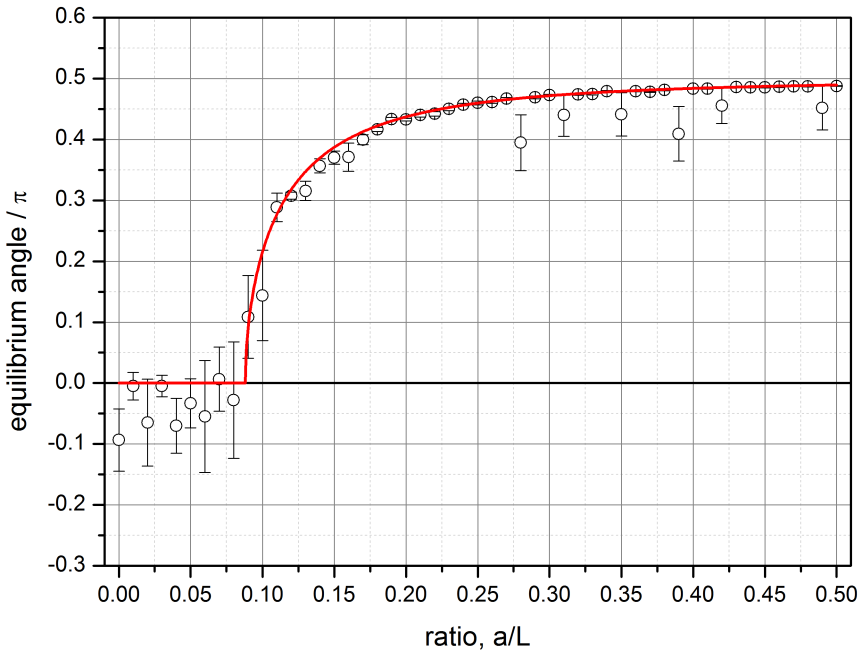

Figure 5.5: Simulated data for stability angle as a function of modulation amplitude in the high frequency regime. Open circles represent the stability angle for a given modulation amplitude (in terms of the ratio a/L). Stability angles are found by fitting an exponential function to simulated angular trajectories. Each point is the mean of at least 5 trajectories; error bars represent the standard deviation of the mean at each point. The red line shows the stability angle predicted by equation (4.32)

5.4 Experiments

Having seen that the predictions made in the previous chapter align with simulated data, we now wish to see if those predictions will also align with experimental data. Firstly, we measure stability angles in the high-frequency regime for a range of modulation amplitudes, using parameters based on the simulation shown above. Next, in order to demonstrate that we can control the dynamic behaviour of the system by altering the characteristic frequencies of the pendulum, we repeat our measurements after having made changes to the pendulum's proper frequency and oscillation frequency. Subsequently, we should see a change in the threshold modulation amplitude. By making further changes to the characteristic frequencies, the pendulum is put into the low-frequency regime. Again, we measure stability angles as a function of modulation amplitude. In the low-frequency regime, it is predicted that the stability angle is also dependent on the driving frequency. The final set of data presented here shows the stability angles measured as a function of the driving frequency.

5.4.1 Calibration

The radial stiffness of the pendulum is calibrated by allowing the particle to diffuse freely in the potential with no fluid drag applied. An example of a histogram of fluctuations in radial position is shown in figure 5.6 (constituting a total of 3×10^4 video frames). Applying the calibration method described in section 3.6.1, the radial spring constant can be found. The histogram also lets us calculate the radius of the potential. The mean radial position tells us the radius is $8.2281 \pm 0.0002\,\mu\text{m}$. This radius is used throughout the experiments.

5.4.2 High-frequency regime

Figure 5.7 shows experimentally measured stability angles as a function of modulation amplitude for two sets of experimental parameters that are within the high-frequency regime. The circles represent stability angles for parameters matching closely to those listed in section 5.3. The proper frequency is $\omega_0 = 2\pi \times 1274\text{Hz}$,

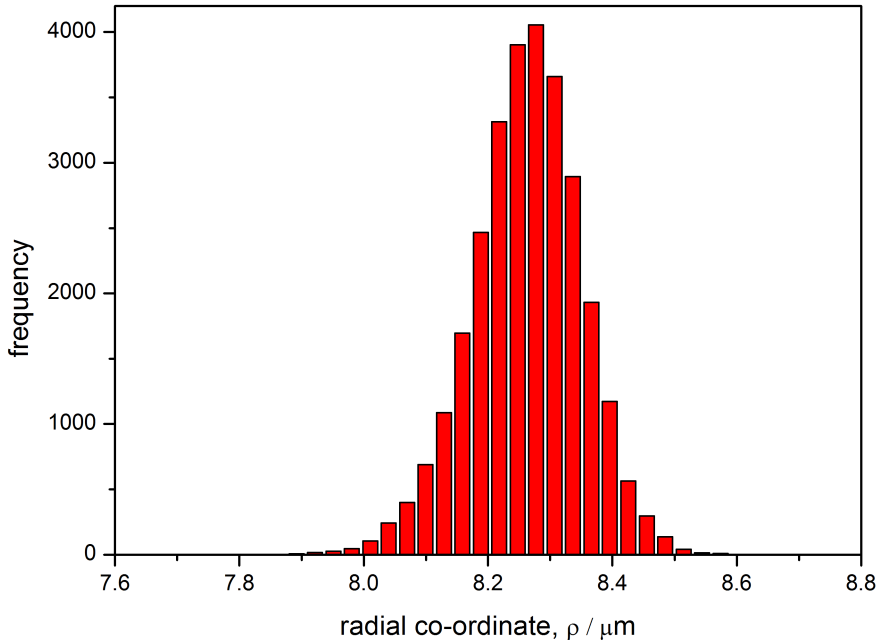

Figure 5.6: Histogram of the radial positions of a particle held in a circular potential with no fluid drag applied. The mean radial position is $8.2281 \pm 0.0002\,\mu\text{m}$.

the oscillation frequency is $\Omega = 2\pi \times 78.3\text{Hz}$ and the modulation frequency is $\omega = 2\pi \times 500\text{Hz}$. The high frequency condition ($\omega \gg \omega_0^2/\gamma_m$) is satisfied since $\omega_0^2/\gamma_m = 2\pi \times 3.8\text{Hz}$. Each point in figure 5.7 is the mean of several trajectories and the errorbars represent the error on the mean. The figure also shows the stability angles predicted by equation (4.32); the agreement with theory is reasonably good. The predicted threshold amplitude, $a_1/L > \sqrt{2}\Omega/\omega_0$ is about 0.087, which is reflected in the data.

By way of demonstrating control over the dynamics of the system through the characteristic frequencies of the system, I made a change to the proper frequency ω_0 and to the oscillation frequency Ω. I then measured the stability angles over the same range of modulation amplitudes. The diamonds in figure 5.7 represent this second set of measured stability angles. For this experiment, the laser power is reduced, leading to a reduction in the value of the proper frequency. The new proper frequency is $\omega_0 = 2\pi \times 806\text{Hz}$ ($\omega_0^2/\gamma_m = 2\pi \times 1.5\text{Hz}$). The stage translation speed is also reduced, to $v_f = 0.75\mu\text{m} \cdot \text{s}^{-1}$. This means the oscillation frequency

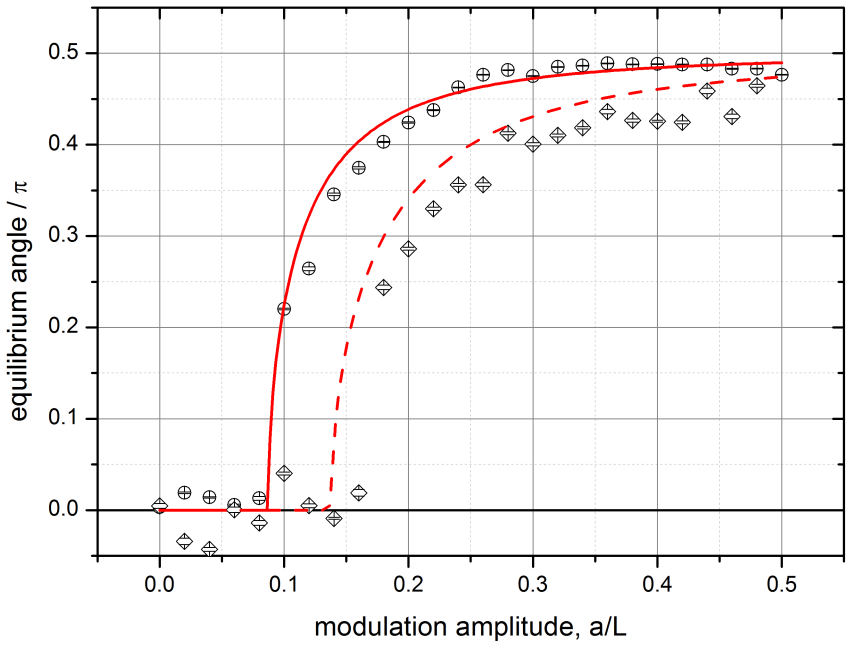

Figure 5.7: Experimental data for stability angle as a function of modulation amplitude in the high frequency regime. Two sets of data are presented here for different values of the pendulum's proper frequency. Diamonds represent stability angles for $\omega_0 = 2\pi \times 806$Hz and circles for $\omega_0 = 2\pi \times 1274$Hz. The solid line indicates the stability angle predicted by equation (4.32) for $\omega_0 = 2\pi \times 1274$Hz; the dashed line applies to $\omega_0 = 2\pi \times 806$Hz.

is increased to $\Omega = 2\pi \times 91$Hz. Equation (4.31) tells us that, with an increase in Ω and a decrease in ω_0, the threshold for stabilisation away from $\psi = 0$ should increase. This is indeed what we see when we compare the results in figure 5.7. The new threshold is predicted to be $a_1/L = 0.14$; reasonable agreement between this prediction (dashed line) and the experimental data can be seen.

The two data sets in figure 5.7 demonstrate the validity of the predictions made in section 4.4.1 of stability angles that are a function of driving amplitude. It can be seen that the threshold for stability away from the 'bottom' of the pendulum can be controlled by tuning the characteristic frequencies of the system.

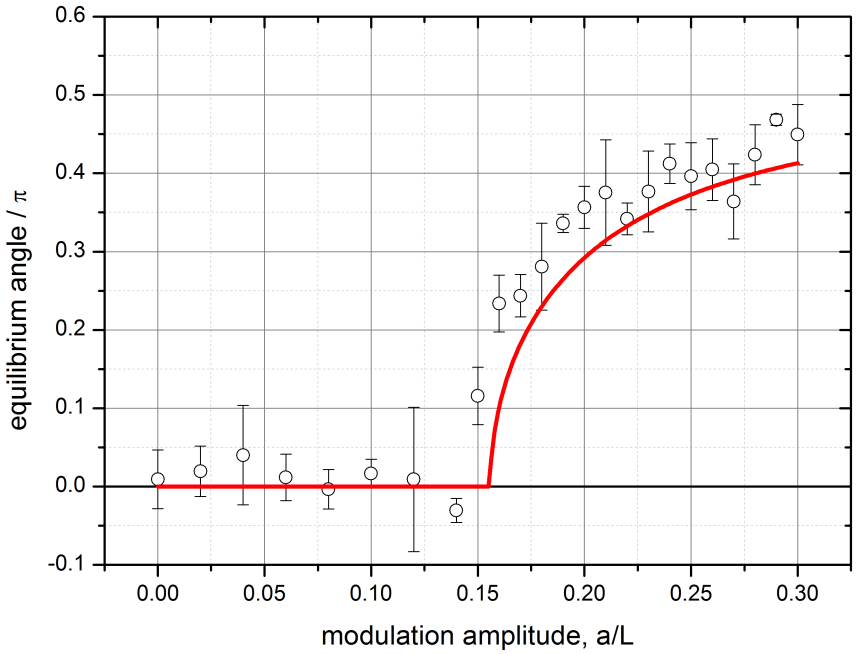

Figure 5.8: Experimental data for stability angle as a function of modulation amplitude in the low-frequency regime ($\omega \ll \omega_0^2/\gamma_m$). In this experiment the modulation frequency is $\omega = 2\pi \times 1\text{Hz}$

5.4.3 Low-frequency regime

By making further changes to the characteristic frequencies of the system we can satisfy the condition $\omega \ll \omega_0^2/\gamma_m$ and move into the low-frequency regime. In order to achieve this, the modulation frequency is decreased to $\omega = 2\pi \times 1\text{Hz}$. The laser power is set such that the proper frequency becomes $\omega_0 = 2\pi \times 757\text{Hz}$. The stage translation velocity is set to $v_f = 0.5\mu\text{m} \cdot \text{s}^{-1}$, giving an oscillation frequency of $\Omega = 64 \times \pi\text{Hz}$. Figure 5.8 shows the measured stability angles as a function of modulation amplitude. The red line represents the stability angles predicted by equation (4.48). The figure demonstrates that the predictions for stability angle as a function of modulation amplitude in the low-frequency regime are supported by experimental data.

It was predicted in section 4.4.2 that in the low-frequency regime the stability angle is dependent on the modulaton frequency as well as the modulation amplitude. To test this, I measured the stability angle over a range of modulation frequencies:

$\omega = 2\pi \times (0 \rightarrow 10)$Hz. I did this for three different proper frequencies: $\omega_0 = 2\pi \times 1591$Hz, $\omega_0 = 2\pi \times 2002$Hz and $\omega_0 = 2\pi \times 2304$Hz. The proper frequency ($\omega_0 = \sqrt{\kappa_\rho / m}$) is modulated via the spring constant, which is itself modulated via the power of the laser. Figure 5.9 shows the measured stability angles and the predictions of equation (4.48). The frequency dependent behaviour is clearly evident at each value of the proper frequency. Increasing the proper frequency increases the threshold frequency, as predicted by equation (4.49).

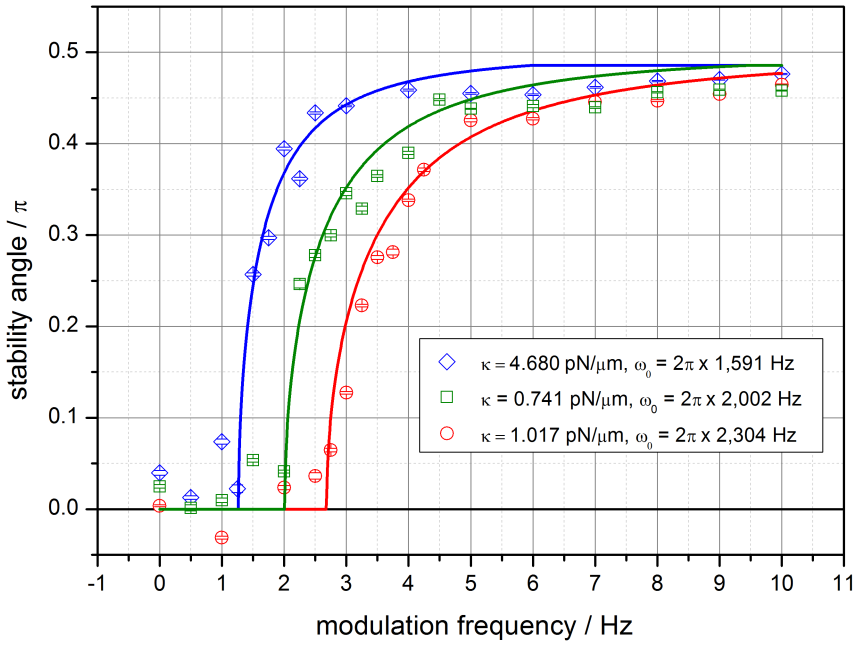

Figure 5.9: Experimental data for stability angle as a function of modulation frequency in the low-frequency regime. In the low-frequency regime, the stability position of the pendulum is dependent on both oscillation amplitude *and* frequency. Three sets of experimental data are shown for different values of the proper frequency, ω_0. The frequency threshold for stability away from the 'bottom' of the pendulum increases with the propoer frequency, as predicted by equation (4.48).

5.5 Summary of part II

In summary, I have presented a theoretical and experimental investigation of the dynamical stability of a pendulum that has a finite stiffness and is subjected to

strong damping. This approach goes beyond the typical assumptions made about the inverted rigid pendulum (infinite stiffness, zero damping) that adopts a stable inverted position if driven at sufficient amplitude and frequency. In the regime of finite stiffness and damping, the pendulum will explore a range of stability positions; the stable position is dependent on a number of tunable characteristic frequencies.

The model presented here is based on a colloidal particle trapped in a ring-shaped optical potential. Fluid flow across the ring causes the particle to move in the direction of flow, towards the 'bottom' of the pendulum. The centre of the ring is sinusoidally modulated in the direction of the fluid flow. Analysis of the model reveals two sub-regimes. If the modulation frequency is significantly larger than the relaxation frequency of the particle in its potential (high-frequency regime), the stability position of the pendulum is dependent only on the modulation amplitude (for a given fluid velocity and trap stiffness). If the modulation frequency is smaller than the relaxation of the particle (low-frequency regime), then the stability position will be dependent on the driving amplitude *and* frequency (again, for a given fluid velocity and trap stiffness).

The predictions of the model have been tested in experiments that use a time-averaged optical tweezers to create a ring shaped potential. Particle trajectories were recorded as the particle moves under the influence of fluid flow from close to the 'top' of the pendulum to a stability position at some point on the ring (dependent on either modulation amplitude or frequency). The stability positions were extracted from the particle trajectories and were found to be in good agreement with those predicted by theory. The experiments illustrate how the tunable dynamics of the system allow for control over the stability position.

One could imagine a particle sorting system based on this concept. Since in the low-frequency regime the stability position is dependent on the friction coefficient, see equation (4.48), particles of different sizes (and hence different friction coefficients) would have different stability positions.

5.5.1 Acknowledgements

The theory work in this part of the thesis was undertaken by a collaborator, David Cubero of the Universidad de Sevilla.

Part III

Deformability of red blood cells in diabetic retinopathy

Chapter 6

Deformability of red blood cells in diabetic retinopathy

In this part of the thesis I will describe an experiment that I have carried out using a dual-beam optical tweezers to measure the deformability of red blood cells from patients with diabetic retinopathy.

6.1 Introduction

Diabetes mellitus (DM) is a chronic disease that occurs when the pancreas does not produce enough insulin or when the body cannot effectively use the insulin it does produce. Insulin is a hormone that regulates blood sugar; if the body is unable to regulate blood sugar hyperglycaemia (a raised blood sugar level) commonly results. Over time, hyperglycaemia can lead to serious damage to many of the body's systems, especially blood vessels and nerves, and is a major cause of morbidity and mortality [**?**].

The damaging effects of hyperglycaemia can be divided into two broad categories: macrovascular complications (coronary artery disease, peripheral arterial disease, and stroke) and microvascular complications (diabetic nephropathy, neuropathy, and retinopathy) [**?**]. Diabetic retinopathy (DR) is a disease of the eye that is caused by hyperglycaemic damage to the microvascular system of the retina. In the early stages of DR, abnormalities due to hyperglycaemia can cause microaneurysms (small

bulges) to develop in the walls of the micro blood vessels which leak red blood cells (RBCs) and serous fluid into the retina. This can induce swelling which obscures the light path to the maculae and causes some loss of vision [**?**, **?**]. In later stages of DR, the blood vessels can become occluded leading to retinal ischemia (a restriction in blood supply to the retina). In response to the ischemia, new blood vessels grow rapidly out of the retinal surface and into the vitreous humour, the clear gel that fills the space between the lens and the retina. The new blood vessels are fragile and tend to bleed into the vitreous humour, obscuring vision. Over time, scar tissue can be formed which may lead to retinal detachment and, ultimately, blindness. In many countries, DR is the most frequent cause of preventable blindness in the working age population [**?**]. The presence of DR also signifies a heightened risk of life-threatening systemic vascular complications.

DM is known to impair the deformability or RBCs [50] and this has been linked to microvascular complications in the kidney [51].

The human red blood cell has a biconcave shape with a typical diameter of $8\,\mu m$ and thickness of $2\,\mu m$. As it travels around the body, it must pass through capilaries with diameters of $3\,\mu m - 5\,\mu m$, requiring the RBC to undergo quite severe deformation. The RBC's ability to undergo such deformation is due to three factors: (i) its large surface-to-volume area, the biconcave disc has a much larger surface area than a sphere of the same volume; (ii) the viscosity of the intracellular fluid; (iii) the viscoelastic properties of the cell membrane [**?**].

A number of experimental methods exist for evaluating the deformability of RBCs. Ektacytometry measures the response or RBCs to shear. RBCs are suspended in a viscous medium between two concentric cylinders. The RBCs undergo elongation due to shear when the inner cylinder begins to rotate. RBC elongation is monitored by the diffraction caused to a laser positioned pependiculrly to the axis of the cylinder [**?**]. Micropipette aspiration (or 'reverse pipetting') records the time taken for a RBC to enter a micropipette at a fixed pressure, allowing the deformability of the RBC to be quantified [**?**]. The process can be automated if cell entry to the pipette is detected as a change in resistance. A similar process occurs in RBC filtration [**?**], when RBCs are passed through a mesh. Mircofluidic techniques

allow real-time characterisation of RBC deformation at rates higher than 100,000 cells/second [**?**, **?**].

Optical tweezers can be used to apply forces that are capable of producing significant deformation of relatively soft RBCs. The cells may be deformed via application of force using attached microbead handles [**?**, **?**], or by applying optical tweezers directly to the RBC to fold [**?**] or stretch RBCs (that are either in the native biconcave shape [**?**] or osmotically swollen into spheres [**?**]). RBCs may even be elongated by counter-propagating beams in the dual-beam optical stretcher [**?**].

6.1.1 Outline of part III

In these experiments I adopt the simple approach of direct trapping using two optical tweezers. The position of one of the tweezers is fixed whilst the other is steerable, allowing me to implement a stretching protocol in which the separation of the two traps is slowly increased. I use video microscopy and post-recording shape analysis to determine the elongation of the cell during the stretch. From a RBC's initial length and maximum elongation I calculate a 'deformability index' for each cycle of the stretching protocol. The average deformability of RBCs from 8 healthy control patients and 7 patients with DR are compared; the results represent a pilot study into the role of RBC deformability in DR using optical tweezers in a direct-trapping configuration.

6.2 Experimental set-up

The experiment is based around a dual-beam optical tweezers. A Nd:YAG 1064nm laser is used to trap the RBCs. The beam passes through a half-wave plate (HWP) and a polarising beamsplitter (PBS) cube. This provides two beams: one beam is linearly polarised in a vertical direction, whilst the other is horizontally polarised. The horizontally polarised beam travels via a pair of orthogonally-mounted galvanometer mirrors (GM) located in a plane conjugate to the back aperture of the aperture. This allows the position of the trap formed by this beam to be steered in two dimensions. Due to the additional reflections from the GM, the beam's po-

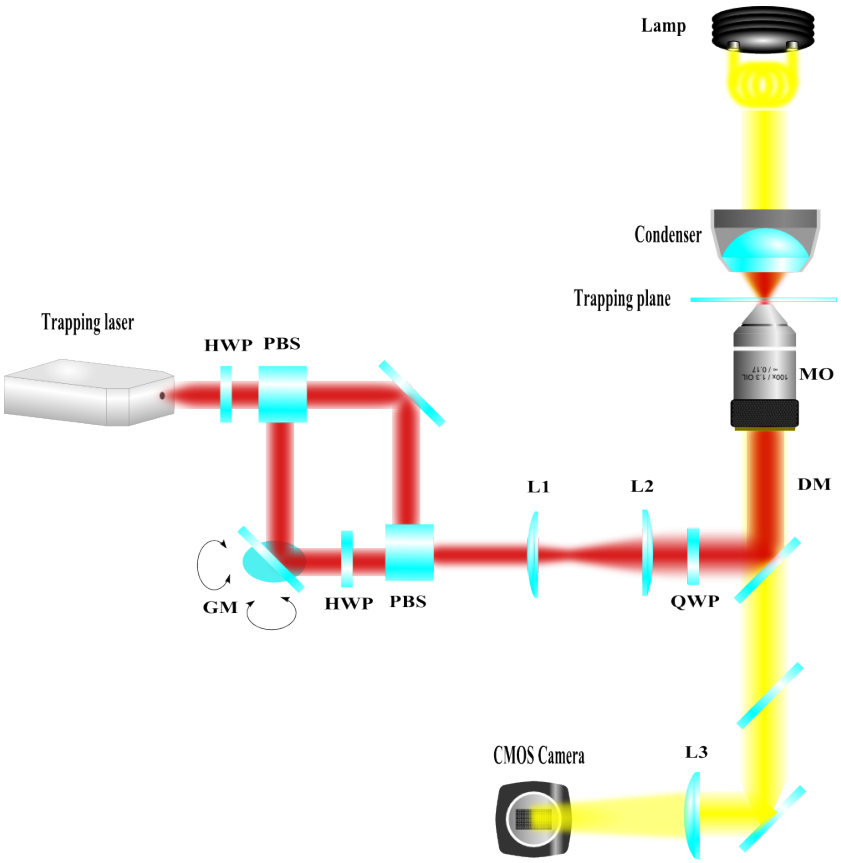

Figure 6.1: RBC deformation experimental set-up. A Nd:YAG 1064nm laser is split into two beams; one of the beams is steered by a pair of perpendicularly mounted galvanometer mirrors. The beams are recombined and injected into the fluorescence port of an inverted microscope. The beams are brought to a focus by a high numerical aperture objective lens.

larisation becomes vertically polarised. In order to maintain two beams of differing polarisation to avoid any interference effects, a second HWP is placed in the path of the beam to return it to a horizontal polarisation. The two beams are then recombined at a second PBS cube. In order to overfill the back aperture of the objective lens, the beams are expanded by a pair of telescoping lenses. Both beams also pass through a quarter-wave plate (QWP). This serves the purpose of circularly polarising the beams. Since the beams have opposite linear polarisations before the QWP the result is two circularly polarised beams of opposite handedness, meaning that the two beams will not interfere with one another. The beams are injected into the fluorescence port of an inverted microscope and brought to a focus at the trapping plane by a 100× 1.3NA oil-immersion objective lens. A glass slide containing RBCs is positioned at the trapping plane. The sample is illuminated by a halogen lamp whose light is gathered by a condenser lens. The light is imaged onto a CCD camera to allow visualisation of the sample. The galvanometer beam steering is controlled by a PC that is connected to the mirror drivers by a data acquisition (DAQ) board.

As figures 6.2a and 6.2c illustrate, the two beams are initially positioned over a RBC lying flat on the glass slide, with a separation less than the RBC diameter. As the RBC is lifted away from the surface it rotates to assume a side-on orientation: see figures 6.2b and 6.2d.

6.3 Sample preparation

Blood samples were collected from the antecubital vein of each patient using a vacutainer. 4 mL samples were transported from Moorfields Eye Hopsital in bio-boxes kept at around 4 °C. The total transfer time was between 30 min and 40 min. Once in the lab, the RBC samples were diluted (6×10^{-4}) with phosphate buffer saline and with 1% bovine serum albumin to prevent formation of aggregates and to prevent cells from adhering to slides. 100 µm − 150 µm of the sample was pipetted onto a glass slide that had been cleaned with ethanol. A glass cover slip (also cleaned with ethanol) was placed on top of the sample and sealed.

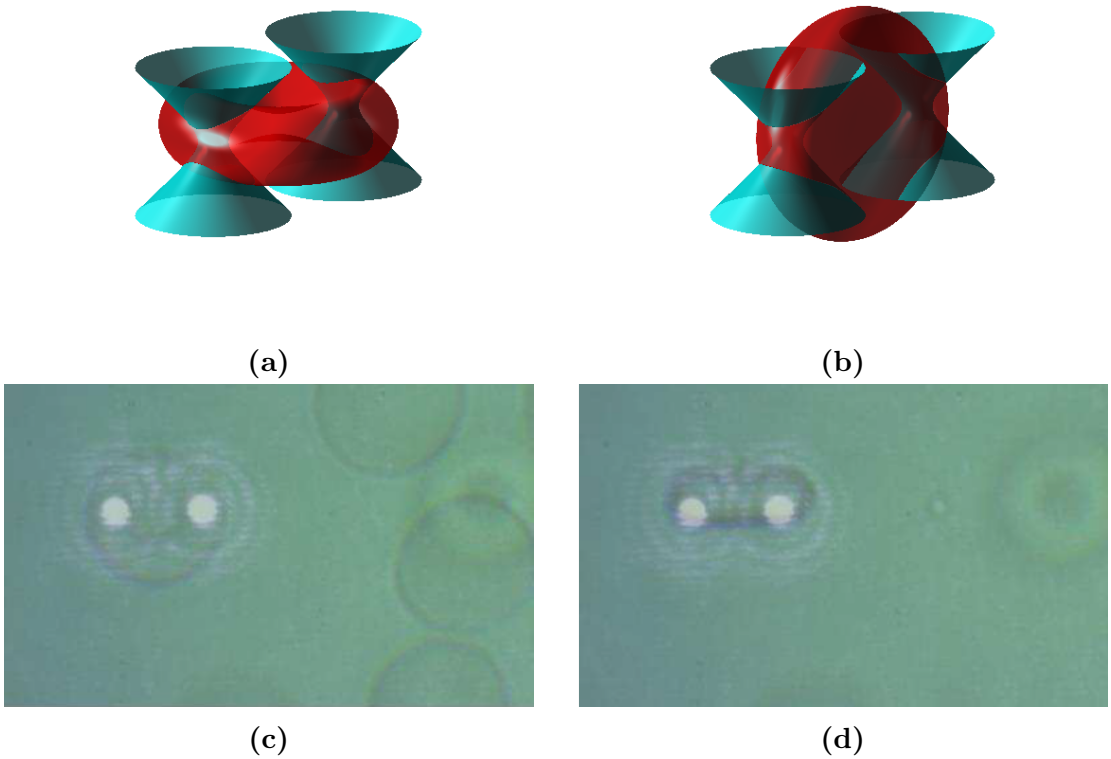

Figure 6.2: Red blood cell trapping. 6.2a illustrates the initial positioning of the two traps over a RBC that is flat on the slide. 6.2b illustrates the rotated RBC after being lifted away from the surface. 6.2c is a micrograph of a RBC lying flat on the glass and 6.2d shows that RBC after being lifted away from the glass.

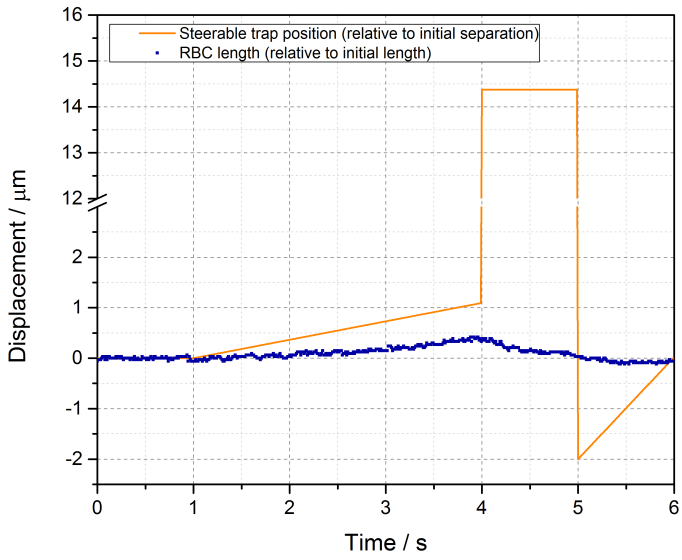

Figure 6.3: Stretching protocol: trap separation and example RBC elongation. The orange line shows the position of the steerable trap relative to the initial separation of the two traps (5.1 µm). The blue dots show the measured length of a RBC during an iteration of the stretching protocol relative to its initial length.

6.4 Stretching protocol

The stretching protocol is designed to slowly stretch the RBC from an initial elongation to a maximal elongation. The initial separation of the two traps is 5.1 µm. Over three seconds the separation is increased to 6.2 µm (see orange trace in figure 6.3). This stretching is repeated up to 30 times for each RBC. To allow the RBC to relax between stretches, the steerable trap is jumped to a separation of 14.4µm and is held there for one second. During this period the RBC relaxes to its equilibrium length. Before repeating the stretching protocol, the RBC must be recaptured by the steerable trap. The steerable trap is jumped to a separation of 3.1 µm and returned to its initial separation of 5.1 µm over a one second interval. Each cell is held in the traps for less than 5 minutes as prolonged trapping of the cells resulted in irreversible damage to the cell, evident in the fact that cells became un-trappable after extended periods of exposure to the laser.

6.5 Shape analysis

Video recordings that capture ten iterations of the stretching protocol are made. In order to extract RBC length data from the videos I implement a shape analysis algorithm written in Matlab. The first step is to convert the frame from a RGB image into a grayscale image and to apply a noise-removal filtering algorithm, see figure 6.4a. The grayscale image is then converted into a binary image: every pixel with an intensity value above a certain threshold is given value 0 whilst every pixel whose intensity is below the threshold is given the value 1. Matlab's `bwboudaries` function [**?**] returns the coordinates of the boundaries in a binary image. The boundary coordinates of the RBC are then sent to Matlab's `regionprops` [**?**] function which characterises the region in terms of some user-defined property such as area, centre-of-mass location or orientation. The major axis of the RBC is aligned with the x-axis of the frame by counter-rotating the frame by the orientation angle. The `bwboudaries` function is applied again to determine the boundary coordinates in the rotated frame. Using these coordinates, the extrema of the region representing the RBC is returned by the `regionprops` function. This constitutes pairs of coordinates that represent the extreme edges of the shape, e.g. top-left, top-right. From these coordinates I find the difference between the left-most and right-most points of the RBC and take this as the RBC's length.

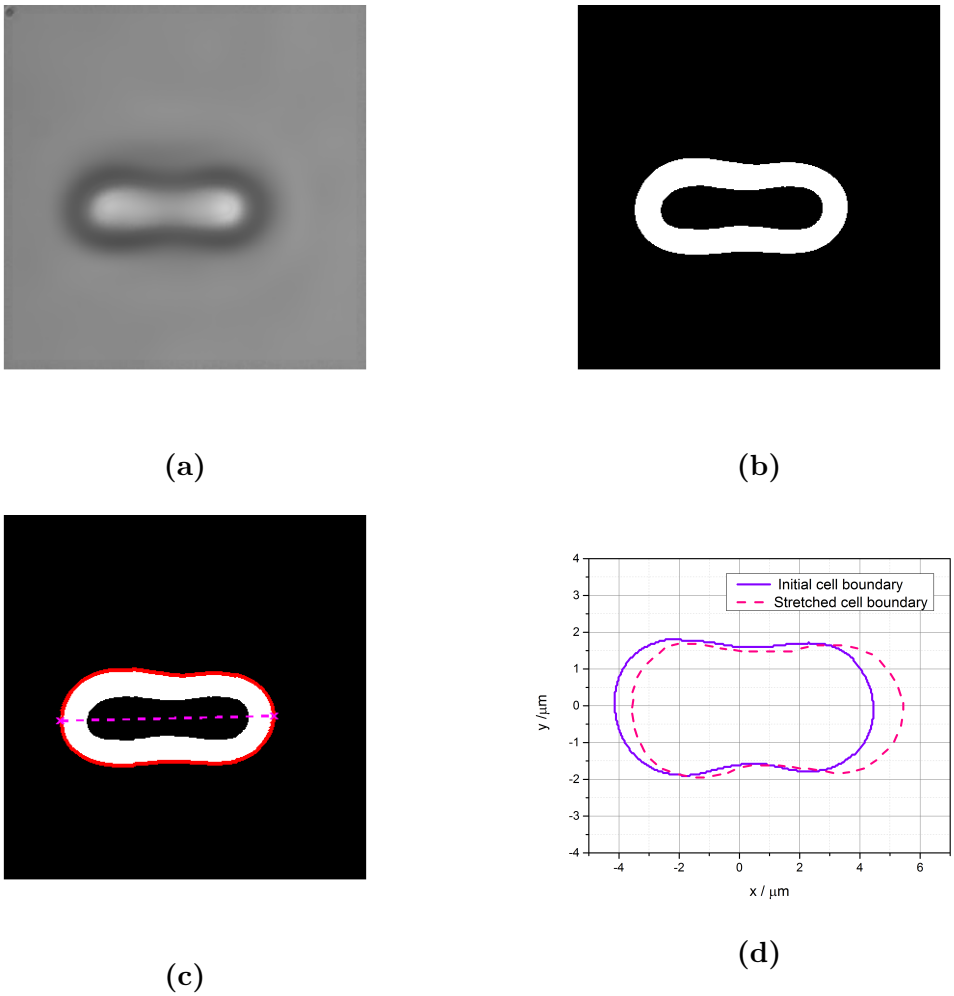

Figure 6.4: Red blood cell shape analysis. Figure 6.4a shows a grayscale image of a RBC held between two optical tweezers. Figure 6.4b shows the same image in a binary form, where white regions represent the dark cell border. In figure 6.4c the calculated boundary and length are marked on the binary image. In the final image, figure 6.4d, the boundaries of the RBC at initial and maximal lengths are shown in comparison.

6.6 Deformability index

The shape analysis algorithm provides the length of the RBC over duration of the stretching protocol. From this length data I calculate a deformability index, DI, that is defined as follows:

$$DI = \frac{L_{\max} - L_{\mathrm{i}}}{L_{\mathrm{i}}}, \tag{6.1}$$

where $L_{\max}$ represent the maximal length of the cell and L_{i} represents the initial length of the cell.

6.7 Results

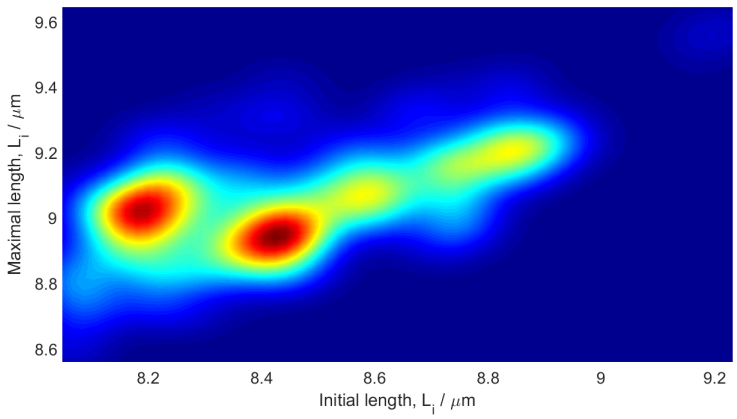

Figure 6.5: Kernel density estimations for pairs of initial and maximal RBC lengths in the control group.

The study compares the mean deformability index of RBCs from 8 control patients (mean age 52.4 years, 5 males, 3 females) and 7 patients with diabetic retinopathy (mean age 54.7 years, 4 males, 3 females). A kernel density estimation for the frequency of pairs of initial and maximal lengths (L_i,L_{max}) are shown for the control group in figure 6.5 and the diabetic retinopathy group in figure 6.6. There are 925 measurement pairs from each group. In both groups there is a linear relationship between initial and maximal lengths. Peaks in the density of pairs are evident in both plots, hinting at a typical initial and maximal lengths. Table 6.1 provides the mean values of L_i, L_{max}, elongation ($L_{max} - L_i$) and the deformability index for both

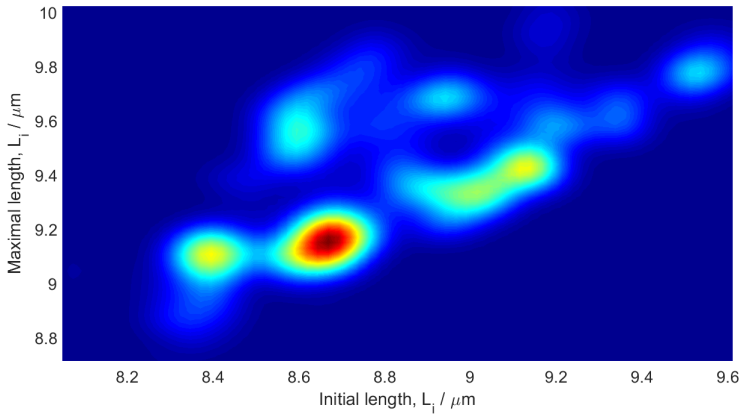

Figure 6.6: Kernel density estimations for pairs of initial and maximal RBC lengths in the diabetic retinopathy group.

groups. The Wilcoxon signed-rank test [**?**] was performed to compare the differences in the means for measurements in the two groups.

The Wilcoxon signed-rank test is a statistical hypothesis test. It takes pairs of data (x_1, x_2) and orders each pair in ascending order by the absolute difference between the two values. In our case, a pair consists of a deformability index measurement from the control group and one from the test group. Each pair is then assigned a rank $(1 \to N)$ and a test statistic is calculated for the set:

$$W = \sum_{i=1}^{N} \mathrm{sgn}(x_{2,i} - x_{1,i}) \cdot R_i, \tag{6.2}$$

where $\mathrm{sgn}(x_{2,i} - x_{1,i})$ is the sign associated with $x_{2,i} - x_{1,i}$ and R_i is the rank assigned to that pair. The idea is that if the two sets of data are identical, the test statistic will equal zero, $W = 0$. If the two sets of data differ, the test statistic will be non-zero, $W \neq 0$. One proposes before the test a null hypothesis: that the two data sets are the same. Given a non-zero test statistic, W, one then looks up the probability (p-value) that the null hypothesis is true, given the value of W. If the value p-value is small (smaller than a pre-determined 'significance value') one can confidently reject the null hypothesis.

The Wilcoxon test was chosen in particular because it can be applied to non-parametric distributions and is this applicable even if our dat does not follow a parametirc distribution. The significance level used for the test was 5%. The p-

	Control	Diabetic retinopathy
Mean initial length $\langle L_i \rangle$	8.449 ± 0.009	8.82 ± 0.01
Mean maximal length $\langle L_{max} \rangle$	9.038 ± 0.005	9.385 ± 0.009
mean elongation $\langle L_{max} - L_i \rangle$	0.589 ± 0.006	0.563 ± 0.008
Mean deformability index $\langle DI \rangle$	0.0703 ± 0.0008	0.065 ± 0.001

Table 6.1: Red blood cell elongation data. All values in micrometres. Mean values are presented with an associated standard error ($\sigma/\sqrt{N}$).

value returned for all tests was well below this value, allowing a rejection of the null hypothesis that there is no significant difference in the mean values of the values in the table. The mean deformability index of the control group is 0.0703 ± 0.0008 and for the group of patients with diabetic retinopathy the mean value is 0.065 ± 0.001. The results suggest a statistically significant decrease in deformability for the patients with DR.

6.8 Discussion

One must be cautious about drawing conclusions from these data about the role of the deformability of RBCs in DR, given the limited sample size of the study. Figure 6.7 illustrates the distribution of measured deformability index values for the two groups and compares this to a normal distribution based on the mean and standard deviation of the measurements. It is evident from the figures that data in neither group is especially well described by a normal distribution. This may simply be down to a lack of data or it may hint at a more complex physiological picture than the one supposed in our analysis. The distributions for both groups could be interpreted as showing multiple peaks and one could hypothesize any number of reasons for such distributions. For example, RBCs are known to become less deformable as they age (a typical RBC lifetime is 120 days). It is possible to separate RBCs by age in a centrifuge [**?**], so to test such a hypothesis in our experimental set-up would be possible. Further study is clearly required to confirm the link between reduced deformability and DR that our experiments hint at.

A significant advantage of this direct trapping approach over the use of microbead handles, in which optical tweezers act on coated microbeads that are bound to the

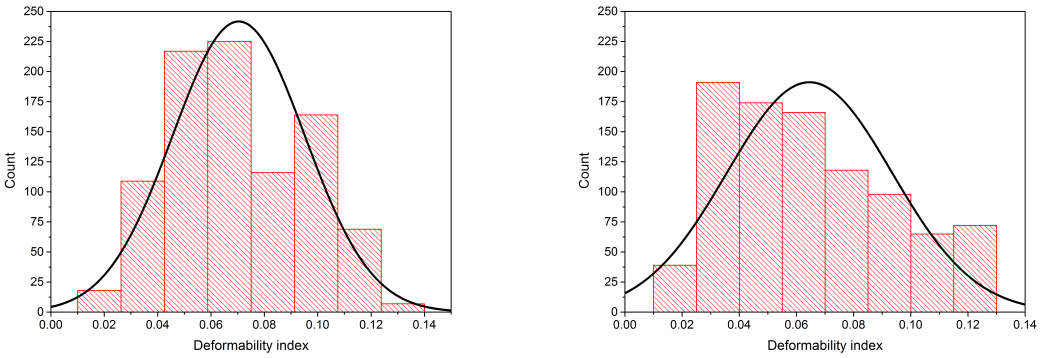

(a) Control group **(b)** Diabetic retinopathy group

Figure 6.7: Histograms and normal distributions for the deformability index in (a) the control group (mean: 0.07, standard deviation: 0.02) and (b) the diabetic retinopathy group (mean : 0.06, standard deviation: 0.03).

membrane of the RBC, is the relative ease and speed at which RBCs can be captured for stretching measurements. There is no need to locate microbeads and to position these on the RBC membrane. If one is interested in obtaining a significant number of measurements then the time taken to obtain them is an important consideration. However, there are several disadvantages to the direct trapping approach. Firstly, unlike with the use of microbead handles, it is difficult to quantify the force applied to the RBC by the optical tweezers: the forces constraining the RBC's centre-of-mass and the stretching force applied when increasing the separation of the pair of tweezers. These forces are easily calibrated if using microbead handles [**?**]. Secondly, the deformation process of the RBC in the direct-trapping approach used here is not trivial. The increase in the separation of the two tweezers is 1.1 µm whilst the average elongation of RBCs (in the control group, for example) is only $\sim 0.6\,\mu m$. It is clear that the positions of the tweezers in relation to the external boundary of the RBC are not fixed and that the increase in the separation of the traps does not directly equate to the elongation of the RBC. Since the tweezers are moving within the body of the RBC during the stretching process, the distribution of stress in the RBC will change as the separation of the two tweezers is increased. This raises questions about the way in which the initial cell length affects the elongation and, therefore, the calculated deformability index of a cell. The boundaries of a larger RBC are necessarily further from the centre of the tweezers in their initial

separation. We do not know how the proximity of the tweezers to the cell boundary affects the force applied to the RBC.

It is possible that as the separation of the two traps increases there is some vertical motion of the RBCs, i.e. that as the traps move apart, the RBC 'sags' downwards. Depending on the position of the imaging plane in relation to the widest part of the RBC (see figure 6.2b) this could either lead to an increase or decrease in the size of the RBC cross-section seen in the microscope objective. If the former were true, this could lead to a false positive in the results: the apparent elongation of the RBCs could in fact be due to a larger cross section moving into the imaging plane. This could be tested by introducing a second imaging system that either allowed a different vertical plane to be imaged or a side-on view of the RBC. A second vertical imaging plane would allow an assesment of the change in cross sections in the two planes, whereas a side-on view would allow for an assessment of the vertical centre of mass.

6.9 Summary of part III

In summary, I have used a pair of optical tweezers to measure the deformability index of red blood cells (RBCs) in a group of healthy patients and a group of patients with diabetic retinopathy (DR). DR is a disease that arises in patients suffering from diabetes mellitus (DM) and affects the microvascular system of the eye. DR, like other microvascular problems linked to DM, is thought to be related to a loss of deformability of RBCs. The aim of these experiments was to investigate this link. The experiment employs a pair of optical tweezers in a direct trapping approach to deform individual RBCs using a defined stretching protocol. A shape analysis algorithm is applied to video recordings of the RBC stretching events to measure elongation. Elongation is normalised by the RBC's initial length to calculate a deformability index. The mean measured deformability index for the control group was found to be 0.0703 ± 0.0008 and for the group of patients with diabetic retinopathy the mean value is 0.065 ± 0.001. A Wilcoxon signed rank test allows a rejection of the null hypothesis that the mean values are equal, suggesting a statistically signifi-

cant decrease in deformability for the patients with DR. Caution must be exercised in drawing conclusions from this study given the limited sample size, but the work demonstrates a promising method for the measurement of deformability in individual red blood cells. The results agree broadly with previously published work [**?**] and an expanded sample size may lead to a stronger association between DR and reduced RBC deformabilty.

6.9.1 Acknowledgements

Dr Rupesh Agrawal was responsible for the recruitment of patients for this study and the transport of samples between Moorfields Eye Hospital and our laboratory at University College London.

Part IV

Work fluctuations in coupled systems

Chapter 7

Work fluctuations: introduction and theory

In this part of the thesis I describe simulations and experiments that I have carried out with the aim of investigating the applicability of the fluctuation theorem to a system of hydrodynamically coupled colloidal particles.

7.1 Introduction

A growing interest in systems that operate on the micro- and nano-scales has driven the development of new concepts in thermodynamics over the last few decades. Classical thermodynamics, which describes energy exchange processes in terms of heat, work and entropy, is largely confined in application to large systems at or close to equilibrium. New approaches have emerged, however, that extend the reach of thermodynamic concepts to small systems far from equilibrium. These approaches refer to quantities such as work in terms of probability distributions, $P(W)$, rather than the exact values that we think of on a macroscopic scale. The probability distribution of applied work represents an ensemble of individual work trajectories collected from many repeats of the same process. Each trajectory is a function of external driving and thermal fluctuations.

The concept of a work trajectory and an associated distribution can be illustrated with the following example. A small aqueously-suspended colloidal particle is held in

a harmonic potential. The position of the potential minimum is held stationary until a certain time, when it is slowly translated at a constant velocity. If we have a means of monitoring the particle's position we will observe that it follows the position of the potential minimum (albeit lagging slightly behind), but that its trajectory is subject to fluctuations due to its Brownian motion. The work applied to the particle is a function of the particle's position in relation to the potential minimum. The position of the potential minimum moves in a steady manner with time. The position of the particle in relation to the minimum, however, is randomly fluctuating. Hence, the applied work must also randomly fluctuate. The implication of this is that if we were to measure the work applied to the particle over a single trajectory and then repeat this measurement over a second trajectory some time later, we would find that the two values of applied work were not equal. If we repeated this process an infinite number of times we would see that the measurements of applied work fit a distribution.

The fluctuating nature of applied work in such a system leads to some novel concepts. Classical thermodynamics tells us that in order to translate the particle-filled potential, work must be done on the system, that is $W > 0$. However, if the energy of the thermal fluctuations of the heat bath is of a similar magnitude to the energy transferred as work, it is possible that a large fluctuation will result in the heat bath providing the work instead, meaning that $W < 0$. This possibility is formalised by a fluctuation theorem (FT):

$$\frac{P(-W_\tau)}{P(W_\tau)} = \exp\left(-W_\tau / k_B T\right). \tag{7.1}$$

The left-hand side of equation (7.1) is the ratio of probabilities that a negative work value occurs over at a time τ to the probability that a positive value of the same magnitude occurs over that time. At short times ($t \sim 0$, $W \sim 0$) the probability of a negative or a positive work value are equal. However, since work is an extensive property (it scales with time and system size) the right-hand side of the fluctuation theorem must decay exponentially with time and/or system size. In order for this to hold, the probability of a negative work value $P(-W_\tau)$ must become vanishingly

small, i.e. there is a growing asymmetry in the probability distribution. This means that we should expect to see fluctuations causing negative work values in small systems over short periods of time, but the chance of doing so for a large system over a long period of time is negligible.

One of the first major works in this field is a paper from 1993 by Evans *et al* [**?**] in which the authors propose a relationship (that has become know as the steady-state fluctuation theorem, SSFT) to predict the symmetry of probability distributions of entropy production in a shear-driven fluid in the steady-state. Their expression relates the probabilities of finding the fluid with an induced shear stress that is in the direction of, or opposite to, the externally imposed shear rate. The following year Evans and Searles [52] proposed a similar relationship that could be applied to systems that relaxed towards the steady-state, known now as the transient fluctuation theorem (TFT). It is worth noting here that although the FTs were originally developed to describe the probability distributions of entropy production, they equally describe other thermodynamic properties such as work and heat (see equation (7.1)). In 1997, Jarzynski outlined a relationship (now known as the Jarzynski relation) which linked the free energy difference between two equilibrium states and the average work required to drive the system in a non-equilibrium process from one state to the other [**?**, **?**]. Later, Crooks proposed an extension to the Jarzynski relation that considered the ratio of probabilities of observing entropy production in 'time-forward' and 'time-reversed' versions of the same process. This has become know as the Crooks fluctuation theorem [**?**].

Many of these theoretical predictions are supported by experiments that have used optical traps to apply small amounts of work to systems operating in noisy environments such as microscopic colloidal particles or biomolecules (DNA, RNA). For example, in 2002 Wang *et al* [28] carried out an experiment in which an optical tweezers dragged a colloidal particle through an aqueous environment, just as described in the example above. By sampling the particle's position at intervals along many different trajectories, they calculated the work applied to the particle and showed that the work distribution obeyed the TFT (or at least an integrated version of the TFT). The Jarzynski relation and Crooks fluctuation theorem were tested

by Bustamante and co-workers [**?**, **?**] by measuring the work applied to stretch RNA molecules using optical tweezers. Blickle *et al* also applied the Jarzynski relation to the work applied to a colloidal particle in an optical potential [**?**].

7.1.1 Outline of part IV

In part IV of this thesis, which contains chapters 7 and 8, I present an investigation into the applicability of the fluctuation theorem to a system of hydrodynamically coupled colloidal particles. More specifically, a system consisting of two micro-particles held in adjacent optical tweezers, separated by a distance of several micrometres. Work is applied directly to one of the particles (particle 2) by changing the position of its trap, dragging the particle through its viscous environment. The trap is moved in an arc around the stationary trap (containing particle 1). The motion of particle 2 creates a fluid flow which causes particle 1 to also be displaced from its equilibrium position, thus indirectly applying work to particle 1.

There have been several papers in recent years in which the authors have investigated heat transfer in coupled fluctuating systems: firstly, for a pair of coupled capacitors [**?**]; secondly, for a pair of optically-trapped hydrodynamically-coupled colloidal particles [**?**]. In the second of these systems, one of the particles is held at an elevated effective temperature by virtue of the fact that its trap is randomly and rapidly changing position. The authors calculate the heat flux between the particles (heat is transferred via the hydrodynamic coupling) and develop a mathematical framework to describe the heat transfer, starting from the coupled particle Langevin equation. Here, in order to assess the work in the system, I decompose the equations of motion of the two particles to find the constituent normal modes. Since work is directly applied to both modes, and the modes are not coupled, it is more straightforward to calculate the work applied to each mode. The value of this approach lies in the fact that it allows the energy in a complicated system to be analysed quite straightforwardly. However, one does not get information on the transfer of energy between the constituent parts of the system.

As our ability to build micro- and nano-machinery advances, it will become important to have an understanding of the thermodynamics that underpin the op-

eration of such machinerey. For example, if one wanted to build a nano-machine with multiple moving parts, it is likely that the motion of those parts would be coupled by the medium in which in the machine operates. The experiment described here is an example of a very simple system that is easily controlled and could be used as a test bed for the fluctuatin work in such a system.

In the remaining sections of chapter 7 I introduce the concept of stochastic energetics, which allows for a stochastic version of the Second Law of Thermodynamics that can be applied to a single trajectory, then I outline mathematically the coupled particle model and show how the normal modes are derived for a two particle system. In chapter 8, I present simulated and experimental data from the system.

7.2 Stochastic energetics

The first law of thermodynamics, $\delta W = \delta Q + dE$, tells us that the change in internal energy of a system, dE, is equal to the difference in the work applied to the system, δW, and the heat dissipated into the environment by the system, δQ (*N.B.* we are using the convention that work applied to the sytem and heat dissipated into the environment are positive). Sekimoto [**?**] has suggested that the first law can be applied to a single trajectory by endowing the Langevin equaton with a thermodynamic interpretation. As we saw in chapter 3, the Langevin equation for a trapped particle in an overdamped system can be written

$$0 = -\gamma \dot{\boldsymbol{x}} + \boldsymbol{\xi}(t) - \frac{dU}{dx}, \tag{7.2}$$

where x is the system's dynamical variable (e.g. the position of a colloidal particle), γ is the friction coefficient, U is the potential energy for the variable x and $\xi(t)$ is the thermal noise from the heat bath with the properties described in equations (3.3) and (3.12). Since the Langevin equation represents the balance of forces on a system, the dynamics it describes must conserve the energy of the system plus the surrounding heat bath. That is, if the system changes by an amount dx, then multiplication of the forces in equation (7.2) by $(-dx)$ yields the energy balance of

the system:

$$0 = -\left[-\gamma\dot{\boldsymbol{x}} + \boldsymbol{\xi}(t)\right] dx + \frac{dU}{dx}dx. \tag{7.3}$$

The first term on the right hand side of equation (7.3) represents the reaction force of the system to the heat bath. The remaining term is the change of the potential energy. The work done by the reaction force can be identified as the heat discarded by the system into the environment:

$$\delta Q = [-\gamma\dot{\boldsymbol{x}} + \boldsymbol{\xi}(t)]dx. \tag{7.4}$$

We can therefore symbolically express the energy balance equation as

$$0 = \delta Q + dU. \tag{7.5}$$

We can extend this formulation by allowing for the possibility that the potential energy depends not only on the system's dynamical variable x but also on a control parameter λ, which represents the effect of an external agent: $U(x, \lambda)$. This could, for example, represent a change in the spring constant of the potential. Our Langevin equation becomes

$$0 = -\gamma\dot{\boldsymbol{x}} + \boldsymbol{\xi}(t) - \frac{\partial U(x,\lambda)}{\partial x}. \tag{7.6}$$

Multiplying through by $(-dx)$ yields another energy balance equation,

$$0 = -\left[-\gamma\dot{\boldsymbol{x}} + \boldsymbol{\xi}(t)\right] dx + \frac{\partial U(x,\lambda)}{\partial x}dx. \tag{7.7}$$

The final term of equation (7.7) can equivalently be written

$$\frac{\partial U(x,\lambda)}{\partial x}dx = dU(x,\lambda) - \frac{\partial U(x,\lambda)}{\partial \lambda}d\lambda. \tag{7.8}$$

This allows us to write the energy balance in equation (7.7) as

$$\frac{\partial U(x,\lambda)}{\partial \lambda}d\lambda = \delta Q + dU. \tag{7.9}$$

The left-hand side of this equation can be identified as the work applied to the dynamical variable by a change in the potential energy due to a change of the control parameter λ:

$$\delta W = \frac{\partial U(x,\lambda)}{\partial \lambda} d\lambda. \tag{7.10}$$

We finally write the energy balance as

$$\delta W = \delta Q + dU. \tag{7.11}$$

Assuming that the internal energy of the system is zero $dE = 0$, as is the (ideal) case for a Brownian particle, equation (7.11) can be identified as a stochastic version of the first law of thermodynamics.

7.2.1 Frame invariance

In the example described in section 7.1.1, of a particle dragged through a fluid by an optical tweezers, the potential energy of the system is

$$U(\boldsymbol{x}, t) = \frac{\kappa}{2}[\boldsymbol{x} - \boldsymbol{\nu} t]^2, \tag{7.12}$$

where the centre of the potential moves at constant velocity $\boldsymbol{\nu}$. The control parameter of the system is time, i.e. $\lambda \equiv t$. Therefore, the incremental work performed on the system is (from equation (7.10))

$$\delta W = \frac{\partial U(x,t)}{\partial t} dt = -\kappa \boldsymbol{\nu}(\boldsymbol{x} - \boldsymbol{\nu} t) dt. \tag{7.13}$$

However, in a reference frame that moves with the trap centre, $\boldsymbol{x}' = \boldsymbol{x} - \boldsymbol{\nu} t$, the potential energy is

$$U(\boldsymbol{x}') = \frac{\kappa}{2}[\boldsymbol{x}']^2, \tag{7.14}$$

and, according to equation (7.10), the incremental work applied to the system is zero:

$$\delta W = \frac{\partial U(\boldsymbol{x}')}{\partial t} = 0. \tag{7.15}$$

We know that this cannot be the case. In the co-moving reference frame, the particle is subjected to a steady fluid flow, of velocity $\boldsymbol{\nu}$, which does work against the potential $U(\boldsymbol{x}')$. In order to account for this oversight, we add a term to the definition of the work increment, equation (7.10) [**?**]:

$$\delta W = \left(\frac{\partial}{\partial \lambda} + \boldsymbol{\nu}\frac{d}{dx}\right) U(\boldsymbol{x}, \lambda) d\lambda. \tag{7.16}$$

7.2.2 Integrated stochastic second law

An integrated version of the stochastic second law, equation (7.11), can be written by integrating the work and heat over a time τ,

$$W_\tau = \int_0^\tau \dot{W} dt = \int_0^\tau \left[\left(\frac{\partial}{\partial \lambda} + \boldsymbol{\nu}\frac{d}{dx}\right) U(\boldsymbol{x}, \lambda)\dot{\lambda}\right] dt, \tag{7.17}$$

$$Q_\tau = \int_0^\tau \dot{Q} dt = \int_0^\tau \Big[\big(-\gamma\dot{\boldsymbol{x}} + \xi(t)\big)\dot{\boldsymbol{x}}\Big] dt, \tag{7.18}$$

leading to

$$W = Q + \Delta U, \tag{7.19}$$

where $\Delta U = U(x_\tau, \lambda_\tau) - U(x_0, \lambda_0)$. Equation (7.19) illustrates that the total work applied to the system is shared into heat Q (i.e. dissipated work) and mechanical work, ΔU (i.e. work associated with a change in the potential energy). It is worth noting that only the work dissipated by the system will contribute to a change in the system's entropy. In the Wang experiment [28], the authors divide the quantity W by $k_B T$ and call this the entropy production. But, as argued by van Zon and Cohen [**?**], this quantity is in fact the total dimensionless work applied to the particle since it includes both the dissipated heat Q *and* the work ΔU required to translate the particle-filled potential. That is not to say that the work of Wang *et al* is invalid, only that the authors have demonstrated the experimental validity of the fluctuation theorem for the work done, as opposed to the entropy production as they claim. In order to measure the heat, and thus entropy production, one would need to be able to monitor the instantaneous velocity of the particle, $\dot{\boldsymbol{x}}$, and this has only been

possible since 2010 [**?**].

7.3 Coupled particle model

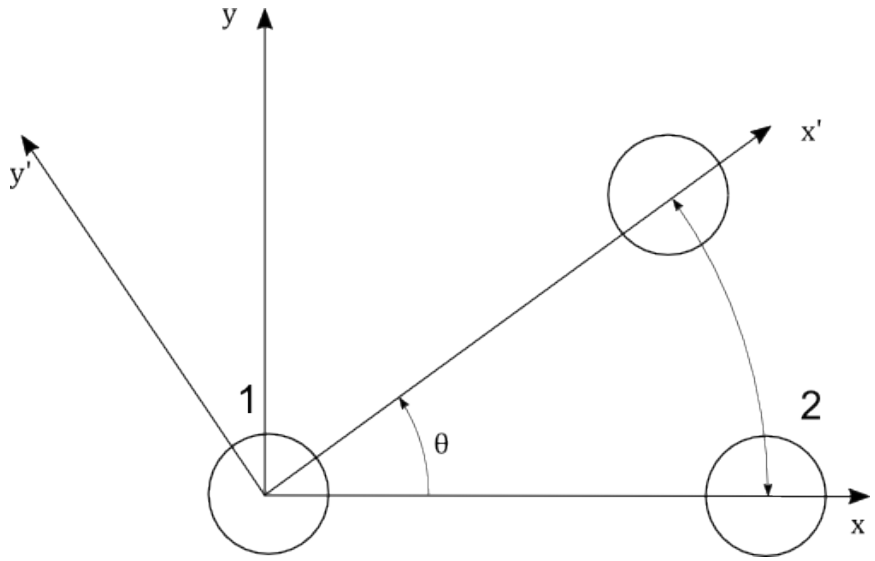

Figure 7.1: Illustration of the coupled particle system. In the inertial (lab) frame, trap 2 moves along an arc segment centred on trap 1, which is positioned at the origin of the axes. The non-inertial reference frame rotates with trap 2.

Our system consists of two colloidal particles held in adjacent optical traps (see fig 7.1). The position of trap 2 is slowly displaced through an angle θ along an arc segment that is centred on trap 1. This geometry was chosen as it allows us to probe both modes of the system whilst keeping the partile separation, in the radial direction, constant.

As outlined in section 3.7, we can describe the over-damped multiple-particle system, in two dimensions, with the following equations of motion:

$$\dot{\boldsymbol{x}}_i = \sum_{j=1}^{2} \boldsymbol{H}_{ij}^{||} \left[-\partial U_j / \partial x_j + \boldsymbol{\xi}_j(t) \right] ; \tag{7.20}$$

$$\dot{\boldsymbol{y}}_i = \sum_{j=1}^{2} \boldsymbol{H}_{ij}^{\perp} \left[-\partial U_j / \partial y_j + \boldsymbol{\xi}_j(t) \right] . \tag{7.21}$$

The noise terms have the following mean and covariance:

$$\langle \boldsymbol{\xi}_i(t) \rangle = 0; \qquad \langle \boldsymbol{\xi}_i(t) \boldsymbol{\xi}_j(t') \rangle = 2k_B T \boldsymbol{H}_{ij}^{-1} \delta(t - t'). \tag{7.22}$$

The potential energy of each particle in the trap, $U_j(\boldsymbol{x}, \boldsymbol{y})$, is dependent on the position relative to the centre of that trap:

$$U_j(\boldsymbol{x}, \boldsymbol{y}) = \frac{\kappa}{2} \left([\boldsymbol{x}_j - \boldsymbol{x}_{0,j}(\theta)]^2 + [\boldsymbol{y}_j - \boldsymbol{y}_{0,j}(\theta)]^2 \right), \tag{7.23}$$

where the positions of the traps are given by

$$(\boldsymbol{x}_{0,j}(\theta), \boldsymbol{y}_{0,j}(\theta)) = (\boldsymbol{r}_j \cos\theta, \boldsymbol{r}_j \sin\theta) \tag{7.24}$$

and $\boldsymbol{r}_j$ are the radial distances from the origin to the centre of each trap. We assume that the two traps have equal spring constants, κ. $\boldsymbol{H}^{||}$ and $\boldsymbol{H}^{\perp}$ are the parallel and perpendicular components of the Oseen tensor. In the nomenclature of the previous section, the trap position represents the control parameter of the system, i.e. $\lambda = \boldsymbol{x}_{0,j}$.

To simplify the mathematics of our system, we move to a reference frame that rotates with θ using the following transformation:

$$\begin{pmatrix} \boldsymbol{x}_i' \\ \boldsymbol{y}_i' \end{pmatrix} = \begin{pmatrix} \cos\theta & \sin\theta \\ -\sin\theta & \cos\theta \end{pmatrix} \begin{pmatrix} \boldsymbol{x}_i - \boldsymbol{x}_{0,i}(\theta) \\ \boldsymbol{y}_i - \boldsymbol{y}_{0,i}(\theta) \end{pmatrix}, \tag{7.25}$$

where we first subtract the trap position then rotate the coordinates by the rotation angle θ using a rotation matrix. In this reference frame, the coordinate $\boldsymbol{x}'$ lies along the axis connecting the two trap centres, whilst $\boldsymbol{y}'$ is perpendicular to this axis. We are most concerned with the perpendicular coordinates, since it is these coordinates to which work is applied by the rotation of trap 2. The equations of motion for the perpendicular coordinates in the rotating frame are

$$\dot{\boldsymbol{y}}_i' + \boldsymbol{\nu}_i = \sum_{j=1}^{2} \boldsymbol{H}_{ij}^{\perp} \left[-\partial U_j' / \partial y_j' + \boldsymbol{\xi}_j(t) \right], \tag{7.26}$$

where U'_j is the potential energy of each trap in the rotating frame,

$$U'_j(\boldsymbol{y}') = \frac{\kappa}{2}(\boldsymbol{y}'_j)^2, \tag{7.27}$$

and $\boldsymbol{\nu}_i$ is the velocity of the fluid flow experienced by each particle (in the rotating frame),

$$\boldsymbol{\nu}_i = \boldsymbol{r}_i\dot{\theta}. \tag{7.28}$$

The properties of the thermal noise are invariant under the rotation. Assuming, as we did in section 3.7, that the fluctuations of the particles' positions are small in comparison with the separation of the traps, we can approximate the components of the perpendicular Oseen tensor as:

$$\boldsymbol{H}^{\perp}_{11} = \boldsymbol{H}^{\perp}_{22} = \frac{1}{\gamma}; \qquad\qquad \boldsymbol{H}^{\perp}_{12} = \boldsymbol{H}^{\perp}_{21} = \frac{1}{\gamma}\frac{3a}{4L}, \tag{7.29}$$

where a is the radius of the particle and L is the separation of the particles.

7.3.1 Normal modes

Equations (7.26) represent a pair of coupled equations. To further simplify the mathematics of the system we will de-couple the equations with a change of basis that diagonalises the matrix $\boldsymbol{H}^{\perp}$. To better illustrate the procedure let us first write equation (7.26) in matrix form:

$$\begin{pmatrix} \dot{\boldsymbol{y}}'_1 + \boldsymbol{\nu}_1 \\ \dot{\boldsymbol{y}}'_2 + \boldsymbol{\nu}_2 \end{pmatrix} = \begin{pmatrix} \boldsymbol{H}^{\perp}_{11} & \boldsymbol{H}^{\perp}_{12} \\ \boldsymbol{H}^{\perp}_{21} & \boldsymbol{H}^{\perp}_{22} \end{pmatrix} \begin{pmatrix} -\kappa\boldsymbol{y}'_1 + \boldsymbol{\xi}_1(t) \\ -\kappa\boldsymbol{y}'_2 + \boldsymbol{\xi}_2(t) \end{pmatrix}. \tag{7.30}$$

In order to change the basis of our system we first need to find an appropriate transformation matrix $\boldsymbol{S}$. Once we know $\boldsymbol{S}$, we can transform any matrix, e.g. $\boldsymbol{y}'$, to the new basis by multiplying it by the inverse of $\boldsymbol{S}$: $\boldsymbol{S}^{-1}\boldsymbol{y}'$ [38]. We can also transform a linear operator, such as $\boldsymbol{H}^{\perp}$, into the new basis with the following transform:

$$\boldsymbol{S}^{-1}\boldsymbol{H}^{\perp}\boldsymbol{S}. \tag{7.31}$$

We can ensure that in our new basis the linear operator is a diagonal matrix if our transformation matrix $\boldsymbol{S}$ has the eigenvectors of $\boldsymbol{H}^{\perp}$ as its columns:

$$\boldsymbol{S} = \begin{pmatrix} \boldsymbol{Y}_1 & \boldsymbol{Y}_2 \end{pmatrix} = \frac{1}{\sqrt{2}} \begin{pmatrix} 1 & 1 \\ 1 & -1 \end{pmatrix}. \tag{7.32}$$

The eigenvectors $\boldsymbol{Y}_1$ and $\boldsymbol{Y}_2$ represent the modes of the system (see section 3.7). In recognition of respective particle motions we will refer to $\boldsymbol{Y}_1$ as the correlated mode and $\boldsymbol{Y}_2$ as the anti-correlated mode.

The linear operator $\boldsymbol{H}^{\perp}$ becomes a diagonal matrix $\boldsymbol{D}$ in the new basis, $\boldsymbol{D} = \boldsymbol{S}^{-1}\boldsymbol{H}^{\perp}\boldsymbol{S}$:

$$\begin{aligned} \boldsymbol{D} &= \frac{1}{2} \begin{pmatrix} 1 & 1 \\ 1 & -1 \end{pmatrix} \begin{pmatrix} \boldsymbol{H}^{\perp}_{11} & \boldsymbol{H}^{\perp}_{12} \\ \boldsymbol{H}^{\perp}_{21} & \boldsymbol{H}^{\perp}_{22} \end{pmatrix} \begin{pmatrix} 1 & 1 \\ 1 & -1 \end{pmatrix} \\ &= \begin{pmatrix} \Lambda_1 & 0 \\ 0 & \Lambda_2 \end{pmatrix}. \end{aligned} \tag{7.33}$$

The diagonal elements of $\boldsymbol{D}$ are the eigenvalues corresponding to eigenvectors $\boldsymbol{Y}_{1,2}$ and are given by

$$\Lambda_{1,2} = \boldsymbol{H}^{\perp}_{11} \pm \boldsymbol{H}^{\perp}_{12}. \tag{7.34}$$

The equations of motion (7.30) in the new basis describe the dynamics of the modes:

$$\boldsymbol{S}^{-1}(\dot{\boldsymbol{y}}' + \boldsymbol{\nu}) = \boldsymbol{D}\boldsymbol{S}^{-1}(-\kappa \boldsymbol{y}' + \boldsymbol{\xi}(t)); \tag{7.35}$$

or

$$\begin{pmatrix} \dot{\boldsymbol{Y}}_1 + \boldsymbol{\mu}_1 \\ \dot{\boldsymbol{Y}}_2 + \boldsymbol{\mu}_2 \end{pmatrix} = \begin{pmatrix} -\kappa\Lambda_1 \boldsymbol{Y}_1 + \boldsymbol{\Phi}_1(t) \\ -\kappa\Lambda_2 \boldsymbol{Y}_2 + \boldsymbol{\Phi}_2(t) \end{pmatrix}, \tag{7.36}$$

with

$$\boldsymbol{Y} = \boldsymbol{S}^{-1}\boldsymbol{y}', \qquad \boldsymbol{\mu} = \boldsymbol{S}^{-1}\boldsymbol{\nu}, \qquad \boldsymbol{\Phi}(t) = \boldsymbol{D}\boldsymbol{S}^{-1}\boldsymbol{\xi}(t). \tag{7.37}$$

The noise terms $\mathbf{\Phi}_i(t)$ have the following mean and co-variance:

$$\langle \mathbf{\Phi}_i(t) \rangle = 0; \qquad \langle \mathbf{\Phi}_i(t) \mathbf{\Phi}_j(t') \rangle = 2k_B T \Lambda_i \delta_{ij} \delta(t - t'). \tag{7.38}$$

It is important to note that terms $\mathbf{\Phi}_{1,2}$ have units of velocity, in contrast with $\boldsymbol{\xi}_{1,2}$, which are forces.

7.3.2 Work applied to the normal modes

The potential energy acting on each mode is

$$U_i(\boldsymbol{Y}) = \frac{\kappa}{2} \boldsymbol{Y}_i^2. \tag{7.39}$$

In the rotating reference frame the potential is not dependent on the control parameter λ. Therefore, according to equation (7.17), the work performed on each mode is

$$W_i = \kappa \int_0^t \boldsymbol{\mu}_i \boldsymbol{Y}_i dt. \tag{7.40}$$

Several papers have derived equations that describe the time evolution of the probability distribution for the work performed on a dragged particle [**?**, **?**, **?**]. Equation (7.40) illustrates that the work is a linear function of the position of the mode. We know, from equation (3.34) in section 3.6 of the introductory part of this thesis, that the probability of the mode being in position $\boldsymbol{Y}_t$ at time t, given that it was in equilibrium at position $\boldsymbol{Y}_0$ at time $t = 0$, is given by

$$P(\boldsymbol{Y}_0, \boldsymbol{Y}_t) = P_B(\boldsymbol{Y}, \kappa) G(\boldsymbol{Y}0, \boldsymbol{Y}_t; t, \kappa), \tag{7.41}$$

where P_B is the Boltzmann distriubtion and G is the Green's function. Now, given the Gaussian nature of both the Boltzmann distribution and the Green's function, we can assume that the probability distribution of the work at time t will have a Gaussian shape:

$$P(W_i, t) = \frac{1}{\sqrt{2\pi\sigma_{W_i}^2}} \exp\left\{ -\frac{W_i - \langle W_i \rangle}{2\sigma_{W_i}^2} \right\}, \tag{7.42}$$

where $\langle W_i \rangle$ is the mean of the i^{th} mode and $\sigma^2_{W_i}$ is the variance. It is shown in reference [**?**] that the mean of the work is given by

$$\langle W_i \rangle = \boldsymbol{\mu}_i^2 \tau_i^2 \kappa [e^{-t/\tau_i} - 1 + t/\tau_i] \tag{7.43}$$

and the variance is equal to twice the mean, $\sigma^2_{W_i} = 2\langle W_i \rangle$. Plugging these values into equation (7.42) gives

$$P(W_i, t) = N \exp\left[-\beta \frac{(W_i - \boldsymbol{\mu}_i^2 \tau_i^2 \kappa [e^{-t/\tau_i} - 1 + t/\tau_i])^2}{4\boldsymbol{\mu}_i^2 \tau_i^2 \kappa [e^{-t/\tau_i} - 1 + t/\tau_i]} \right], \tag{7.44}$$

where

$$N^{-1} = 4\pi\beta \boldsymbol{\mu}_i^2 \tau_i^2 \kappa [e^{-t/\tau_i} - 1 + t/\tau_i]^{1/2}, \tag{7.45}$$

and $\beta = 1/k_B T$. We can also show that the work distribution conforms to the fluctuation theorem (equation (7.1)):

$$\begin{aligned} \frac{P(-W_i)}{P(W_i)} &= \exp\left\{ \beta \frac{-(-W_i - \langle W_i \rangle)^2 + (W_i - \langle W_i \rangle)^2}{4\overline{W_i}} \right\} \\ &= \exp\left\{ \beta \frac{-4W_i \langle W_i \rangle}{4\overline{W_i}} \right\} = \exp\{-\beta W_i\}. \end{aligned} \tag{7.46}$$

An integrated version of the fluctuation theorem can be a useful indicator of the time evolution of the distribution:

$$\frac{P(W_i < 0)}{P(W_i > 0)} = \langle \exp(-W_i) \rangle_{W>0}, \tag{7.47}$$

where

$$P(W_i < 0) = \int_{-\infty}^{0} P(W_i) dW, \tag{7.48}$$

$$P(W_i > 0) = 1 - P(W_i < 0), \tag{7.49}$$

and the right-hand side of equation (7.47) is the average of $\exp(-W_i)$ over positive W_i. Predictions of the time evolution of the left-hand side of the IFT can be found

in the literature [**?**, **?**]:

$$\frac{P(W_i < 0)}{P(W_i > 0)} = \frac{1 - \text{erf}\left(\frac{1}{2}\sqrt{\omega(t)}\right)}{1 + \text{erf}\left(\frac{1}{2}\sqrt{\omega(t)}\right)}, \tag{7.50}$$

where

$$\omega(t) = \frac{\gamma^2 \boldsymbol{\mu}^2}{\kappa k_B T}\left(\frac{t}{\tau} - (1 - \exp(-t/\tau))\right) \tag{7.51}$$

and erf is the error function,

$$\text{erf} = \frac{2}{\sqrt{\pi}}\int_0^x \exp(-t^2)dt. \tag{7.52}$$

To avoid confusion, henceforth, the fluctuation theorem in equation (7.1) will be referred to as the detailed fluctuation theorem. With the detailed fluctuation theorem and integrated fluctuation theorem we have two tools with which to analyse the work applied to the modes of our coupled system of colloidal particles.

Chapter 8

Work fluctuations: simulations, experiments and discussion

In this chapter I present data from simulations and experiments designed to test the model outlined in the previous chapter. The general experimental procedure is as follows. The two particles are held in stationary traps for sufficient time that they reach thermal equilibrium. At time $t = 0$ the position of trap 2 is moved along an arc centred on the position of trap 1 for a short period of time. In the simulations, this process is simply repeated N number of times. In the experiments, once the position of trap 2 reaches the end of its arc, the two particles are again allowed to relax to equilibrium in their respective traps. Trap 2 is then moved in reverse, back along the arc. Thus, from this cyclical process we have two individual trajectories for analysis. The cyclical process is repeated $N/2$ times.

8.1 Simulations

Presented here are finite-difference simulations (see section 3.8) of equations (7.36) with the following (laboratory achievable) parameters.

- Particle radius: $a = 0.75\mu\text{m}$.
- Particle separation: $L = 3\mu\text{m}$.
- Spring constant: $\kappa = 0.3\text{pN} \cdot \mu\text{m}^{-1}$.

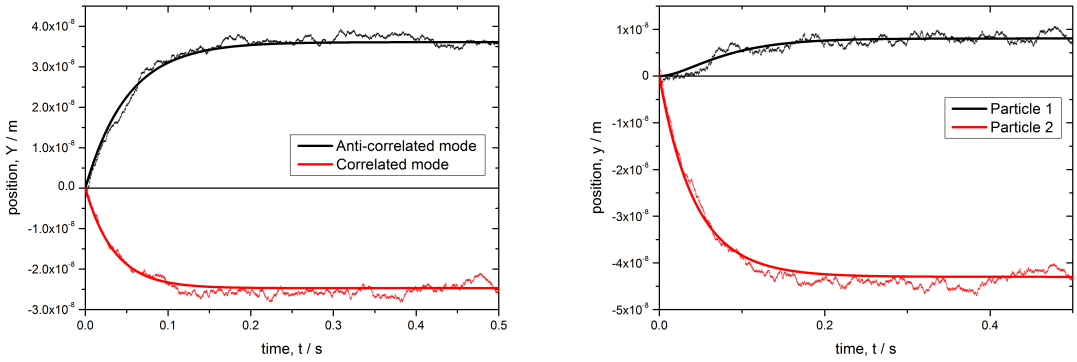

(a) Mode trajectories **(b)** Particle trajectories

Figure 8.1: (a) Ensemble average of simulated mode trajectories, with prediction given by equation (3.19): $\langle Y_i \rangle = \tau_i \boldsymbol{\nu}_i (1 - \exp(-t/\tau_i))$. **(b)** Ensemble average of simulated particle trajectories (in rotating reference frame), $\boldsymbol{y}' = \boldsymbol{SY}$. At first glance it may appear that the particles are moving in opposite directions in figure 8.1b. This is not the case, however. The particle positions are shown relative to their respective trap centres. Trap 2 is always ahead of particle 2, resulting in a negative relative coordinate. Trap 1 is always stationary, so as particle 1 is dragged in the wake of particle 2 the relative coordinate is positive.

- Fluid viscosity: $\eta = 8.8 \times 10^{-4}\text{Pa} \cdot \text{s}$.
- Fluid velocity (rotating reference frame): $\boldsymbol{\nu}_1 = 0\mu\text{m} \cdot \text{s}^{-1}$; $\boldsymbol{\nu}_2 = 1\mu\text{m} \cdot \text{s}^{-1}$.
- Temperature: $T = 293\text{K}$.

The ensemble average of the mode and particle (in the rotating frame) trajectories can be seen in figure 8.1. Particle trajectories are found by multiplying the simulated mode trajectories by the transformation matrix $\boldsymbol{S}$. Each of the 5×10^3 trajectories consist of 5×10^3 points with a time step of 10^{-4}s, giving a duration of 0.5s. The duration of each trajectory is significantly longer than the relaxation period of either mode, allowing the modes ample time to relax to their new equilibrium positions:

$$\tau_{corr} = \frac{1}{\kappa\Lambda_1} = 0.0349\text{s}; \qquad \tau_{anti} = \frac{1}{\kappa\Lambda_2} = 0.0510\text{s}.$$

The particle coupling is clearly illustrated in 8.1b. Particle 2 is directly displaced by an externally generated fluid drag (in the rotating frame). The motion of particle 2 then creates a movement of fluid around particle 1, causing it to be dragged in the

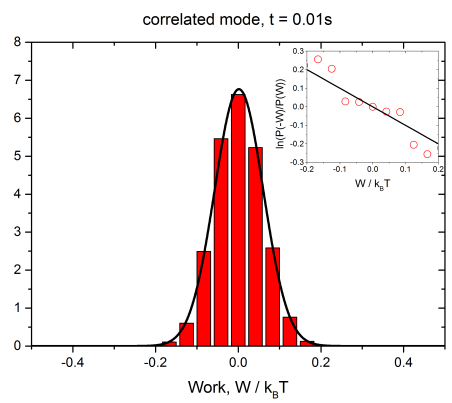

(a) Work distribution, t = 0.01s

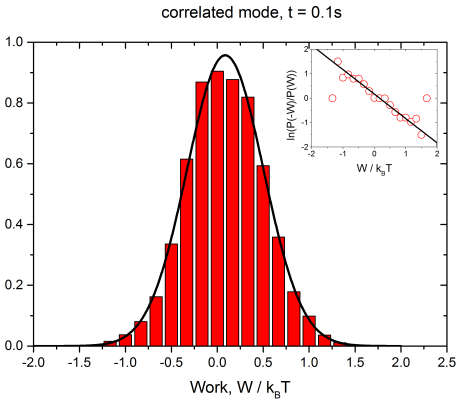

(b) Work distribution, t = 0.1s

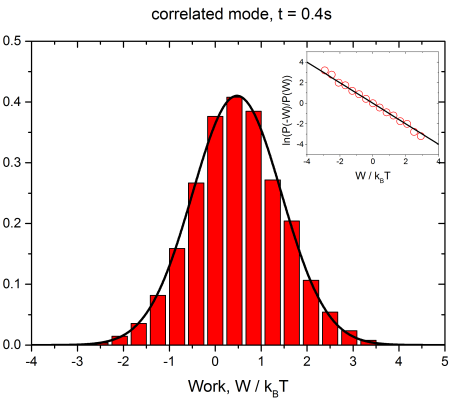

(c) Work distribution, t = 0.4s

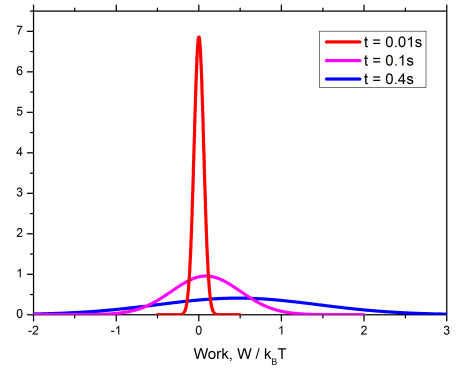

(d) Time evolution of work distribution

Figure 8.2: Correlated mode. Figures **(a)** - **(c)** show the histograms of the work on simulated correlated mode at the times indicated (all histograms are normalised by area). The black lines indicate the prediction of equation (7.44). Insets illustrate the fluctuation theorem: $\ln(P(-W)/P(W)) = -W/k_BT$. Red circles illustrate ratios and black line indicates the expected curve. Figure **d** illustrates the time evolution of the work distribution.

wake of particle 2. This behaviour is as expected from the form of the Oseen tensor.

8.1.1 Correlated mode

Figures 8.2a - 8.2c are histograms of the work (i.e. the work values at a given time from all trajectories are collected and sorted into histogram bins) on the simulated correlated mode at $t = 0.01$s ($t < \tau_{corr}$), $t = 0.1$s ($t > \tau_{corr}$) and $t = 0.4$s ($t >> \tau_{corr}$) respectively. The work applied to the modes is calculated along each of the 5×10^3

trajectories via equation 7.40,

$$W_i = \kappa \boldsymbol{\mu}_i \int_0^t \mathbf{Y}_i dt, \tag{8.1}$$

where the constant velocity $\boldsymbol{\mu}_i$ has been pulled out of the integral. In practice, the integral of position $\mathbf{Y}_i$ in equation (8.1) is approximated via the trapezoidal method:

$$\int_{t_1}^{t_2} \mathbf{Y}_i dt \simeq (t_2 - t_1) \left[\frac{\mathbf{Y}_i(t_1) + \mathbf{Y}_i(t_2)}{2} \right]. \tag{8.2}$$

The first distribution (8.2a) is calculated at a time smaller than the relaxation period of the mode, τ_{corr}, whilst the other distributions are from longer times. The black lines in the figures illustrate the probability distribution given by equation (7.44).

The insets illustrate the detailed fluctuation theorem (equation (7.1)) by plotting the natural log of the left-hand side against the natural log of the right-hand side of equation (7.1), i.e.

$$\log \left(\frac{P(-W_1)}{P(W_1)} \right) = -\frac{W_1}{k_B T}. \tag{8.3}$$

Red circles are calculated by taking the natural log of the ratio of the count in the bin centred at $-W_i/k_BT$ to the count in the bin centred at W_i/k_BT. The black line represents the expected curve with a gradient of negative one. Good agreement is seen between the histograms and the predictions of equation (7.44). The detailed fluctuation theorem holds up well, although at shorter times there is deviation from the prediction at the larger positive and negative work values. This is likely due to poor statistics; there are few counts in the histogram bins away from the mean value.

Figure 8.2d illustrates the time evolution of the work distribution. It is clear that the mean has shifted towards positive work values and that the distribution has broadened. This agrees with the qualitative description of the work distribution described earlier (section 8); the probability of observing negative work values is diminishing with time.

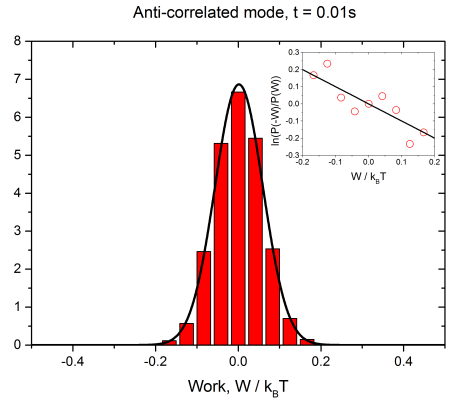

(a) Work distribution at time t = 0.01s

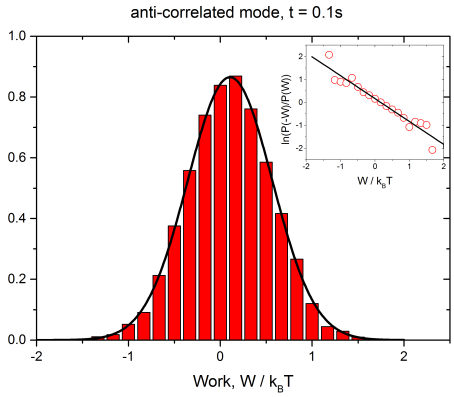

(b) Work distribution at time t = 0.1s

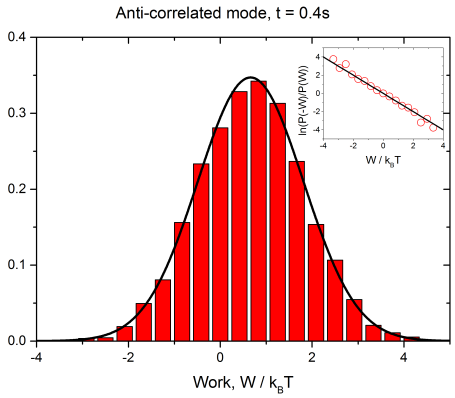

(c) Work distribution at time t = 0.4s

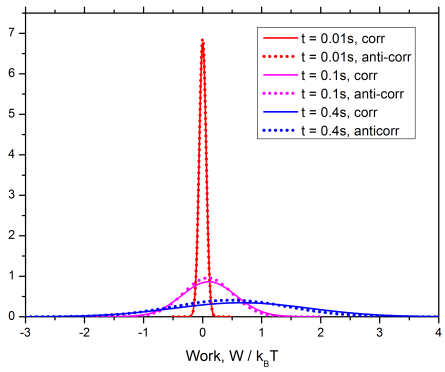

(d) Time evolution of work distribution

Figure 8.3: Anti-correlated mode. Figures **a** - **c** show the distribution of work on the simulated anti-correlated mode at the times indicated. The black lines indicate the prediction of equation (7.44). Insets illustrate the detailed fluctuation theorem: $\ln(P(-W)/P(W)) = -W/k_BT$. Red circles illustrate ratios and black line indicates the expected curve. Figure **d** illustrates the time evolution of the work distribution for the anti-correlated mode (soild lines) and compares this with the correlate mode (dashed lines) at the same time steps.

8.1.2 Anti-correlated mode

Similarly to the work distributions for the correlated modes shown in figure 8.2, figure 8.3 shows the work distributions for the anti-correlated modes at 0.01s, 0.1s and 0.5s. Again, we see that the data conforms to the predictions of the detailed fluctuation theorem (equation (7.1)) and the distribution prediction (equation (7.44)). Figure 8.3d compares the shapes of the work distribution for the anti-correlated and correlated modes at time $t = 0.01$s, $t = 0.1$s and $t = 0.4$s. One can see that the correlated mode evolves faster than the anti-correlated mode, i.e. the mean shifts to positive values and distribution broadens faster. We can attribute this behaviour to the different eigenvalues of the modes. The correlated mode relaxes faster than the anti-correlated mode, meaning the rate of work is larger for the correlated mode.

8.1.3 Integrated fluctuation theorem comparison

Figure 8.4 illustrates the integrated fluctuation theorem at different times along the trajectories for the correlated and anti-correlate modes. The left-hand side of the IFT is evaluated by taking the ratio of the number of positive to negative work values at every time time step, dt, across all simulated trajectories. The right-hand side is the mean of the exponential of all positive work values at each time. For clarity, only every 50th point of the left-hand sides of the IFTs are shown in the figure. Clearly, there is good agreement between the left- and right-hand sides of the IFT. This should not be a surprise since we have already seen good agreement between the left- and right-hand sides of the detailed fluctuation theorem in figures 8.3 and 8.2. The agreement with the prediction of equation 7.50 is not perfect but is still reasonably good. Improved statistics, i.e. additional trajectories, may improve the agreement with theory.

This figure nicely illustrates the difference in the rates of work for the two modes; the rate of work for the correlated mode is faster, as we have already seen in figure 8.3d. In order for the ratio $P(W_i < 0)/P(W_i > 0)$ to decay faster, the probability of positive work values $P(W_i)$ must grow more quickly. The faster decay rate of the IFT for the correlated mode in figure 8.4 tells us that the mean work value is

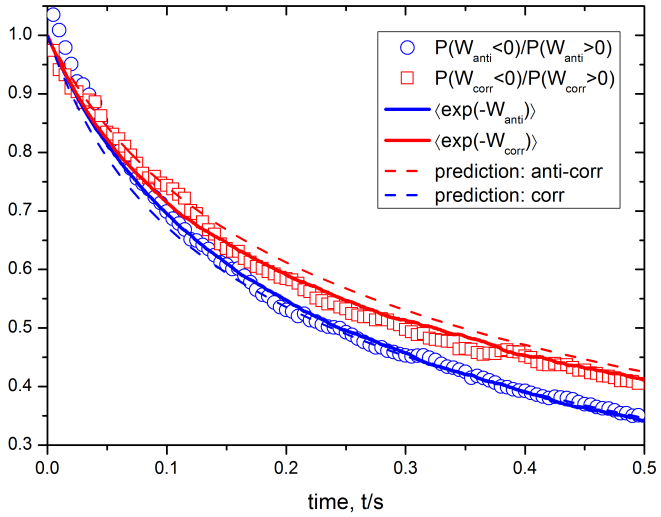

Figure 8.4: Integrated fluctuation theorems (IFTs) for the correlated and anti-correlated modes - simulated data. Blue circles represent the left-hand side of the IFT (equation (7.47)) for the anti-correlated mode; the ratio of negative work values to positive work values for the correlated mode at times $t = 0 \rightarrow 0.5\,\mathrm{s}$. The blue line represents the right-hand side of the IFT; the mean of the exponential of all work positive work values. The dashed blue lines represent the prediction of the time evolution of the IFT in equation (7.50). The red squares, solid red line and dashed red lines represent the left- and right-hand side of the IFT and prediction for the correlated mode. For the sake of clarity only every 50th point of the left-hand side is shown.

shifting towards the positive faster than the anti-correlated mode. This is due to the shorter relaxation time of the correlated mode, as was pointed out in the section 8.1.2.

8.2 Experiments

The simulations presented above demonstrate that the stochastic dynamics of a coupled particle system can be probed and measured using parameters that are achievable in the laboratory. In this section I present several figures that illustrate the progress I have made in my attempts to produce the simulated results in the laboratory. I used an experimental set-up identical to that described in section 6.2. A pair of optical tweezers are formed by splitting a single Gaussian beam into two individual beams with a polarising beam splitter. One of the beams travels via a pair of orthogonally mounted galvanometer mirrors, allowing the position of that trap to be steered.

The mirrors are positioned by sending a voltage from a PC to the mirror drivers. In these experiments I needed control of the separation between the two traps so it was necessary to calibrate the mirror driver voltage values, allowing me to separate the traps by a known distance. This was achieved with the following procedure. The reflections from a glass slide of the two laser beams were aligned by adjustment of the driver voltage and the required voltage was recorded. Next, the traps were separated by some arbitrary input voltage and a particle was trapped in the steerable trap. The steerable beam was then stepped through a number of positions in x and y whilst video frames were captured on the digital camera. The positions of the two particles are extracted from the recorded videos by a particle tracking algorithm (see section 5.2 for a description of algorithm). The voltage values associated with each step were also recorded and compared with tracking results from the video. Comparison of the voltage and the spatial measurements allowed the calculation of voltage-to-separation calibration factors. With this knowledge I could position trap 2 at a given distance from trap 1 and by sending a cosine wave to the mirror controlling the x position of the trap and a sine wave to the mirror controlling the

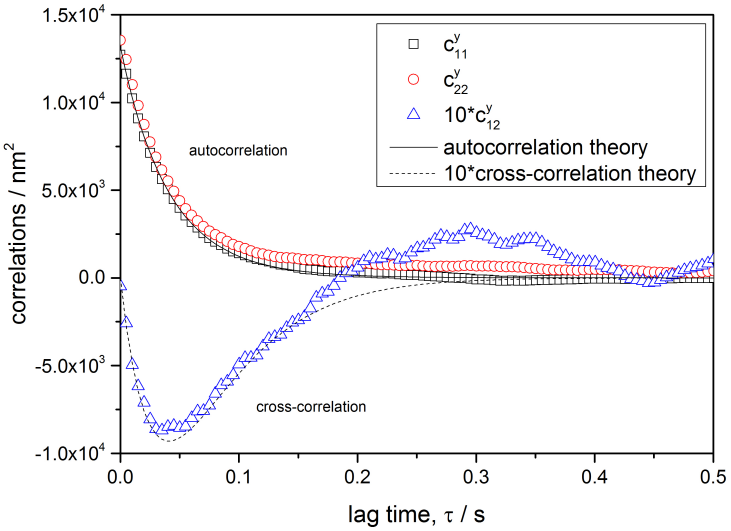

Figure 8.5: Correlation data. Two silica particles of 1.5µm diameter are held in individual optical tweezers separated by 3µm in the x direction. The figure shows the autocorrelation of the two particles (black squares, red circles) and their cross-correlation (blue triangles) in the direction perpendicular to their separation, y. Also shown are the correlation predictions of equations (3.27) and (3.48). *N.B.* the auto-correlation data has been multiplied by a factor of 10 in this figure.

y position, I could move trap 2 along the circumference of a circle centred on trap 1.

A first test of the experimental set-up was to see whether the coupling of the particles could be observed and whether the split in the mode decay times could be resolved. I tested this by measuring the cross-correlation in the position of two particles in stationary adjacent traps using parameters close to those used in the simulations. The particles had a 1.5µm diameter are were held in individual optical tweezers, with the following measured spring constants:

- $\kappa_{1,x} = 0.310 \pm 0.003\,\mathrm{pN}\cdot\mu\mathrm{N}^{-1}$;
- $\kappa_{1,y} = 0.296 \pm 0.003\,\mathrm{pN}\cdot\mu\mathrm{N}^{-1}$;
- $\kappa_{2,x} = 0.267 \pm 0.003\,\mathrm{pN}\cdot\mu\mathrm{N}^{-1}$;
- $\kappa_{2,y} = 0.309 \pm 0.003\,\mathrm{pN}\cdot\mu\mathrm{N}^{-1}$.

The traps were separated by $2.908 \pm 0.001\,\mu\mathrm{m}$ along the x axis. I recorded 2×10^4 frames at a rate of 200Hz of the two particles performing Brownian motion in their

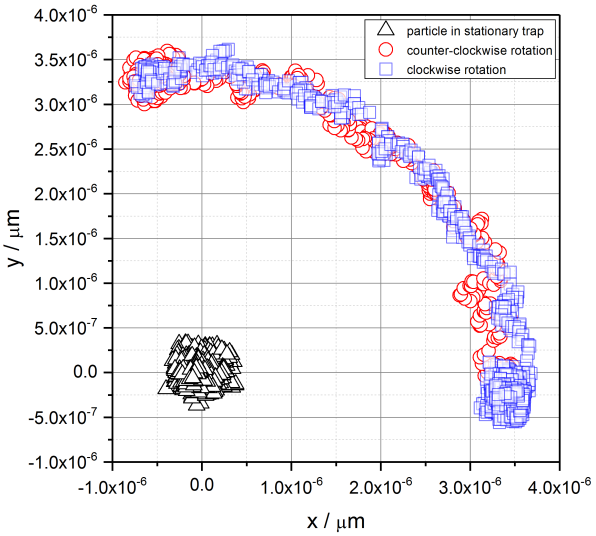

Figure 8.6: Particle trajectories during a counter-clockwise, then clockwise, rotation of the trap 2 about trap 1. The spread of points at the end of each rotation indicate a period of time when the particle is free to diffuse in its temporarily stationary trap.

traps. Figure 8.5 shows the auto- and cross-correlation calculated from the positional data. The correlation predictions of equations (3.27) and (3.48) are also shown; there is good agreement between theory and experiment here. As discussed in section 3.7, the time-delayed dip in the cross-correlation of the two particles is evidence of the difference in decay constants of the two modes. It is this difference in decay times that leads to the different rates of work evident in the simulations, see figure 8.4.

The next step was to perform the experiment in which the position of trap 2 is moved in an arc around trap 1. The parameters for this experiments were as follows.

- Spring constants:
  - $\kappa_{1,x} = 0.307 \pm 0.003\,\mathrm{pN} \cdot \mu\mathrm{m}^{-1}$;
  - $\kappa_{1,y} = 0.323 \pm 0.003\,\mathrm{pN} \cdot \mu\mathrm{m}^{-1}$;
  - $\kappa_{2,x} = 0.328 \pm 0.003\,\mathrm{pN} \cdot \mu\mathrm{m}^{-1}$;
  - $\kappa_{2,y} = 0.293 \pm 0.003\,\mathrm{pN} \cdot \mu\mathrm{m}^{-1}$.
- Particle radius: $a = 0.75\mu\mathrm{m}$.

- Particle separation: $L = 3.3722 \pm 0.0003\,\mu\text{m}$.
- Fluid viscosity: $\eta = 8.8 \times 10^{-4}\text{Pa} \cdot \text{s}$.
- Trap displacement velocity: $\dot{\theta} = 0.84\,\text{rad} \cdot \text{s}^{-1}$.
- Fluid velocity (rotating reference frame):
  - $\boldsymbol{\nu}_1 = 0\,\mu\text{m} \cdot \text{s}^{-1}$;
  - $\boldsymbol{\nu}_2 = 2.819 \pm 0.003\,\mu\text{m} \cdot \text{s}^{-1}$.
- Temperature: $T \sim 293\text{K}$.
- Sampling frequency (camera frame rate): 200 Hz

For the region of interest (i.e. the number of pixels) required to capture the trajectories in these experiments, a frame rate of 200 Hz is at the limit of the camera's capability.

As outlined above, the particles are initially at equilibrium in their traps. At time $t = 0$ trap 2 begins to move in an anti-clockwise direction around trap 1 at a fixed radius, L. The duration of each trajectory was 2 s, which resulted in an angular displacement of trap 2 of ~ 1.8 rad. After this 2 s trajectory the particles were held in their stationary traps for 4 s, a time that greatly exceeds the relaxation time of the modes:

$$\tau^{ex}_{corr} = \frac{1}{\kappa\Lambda_1} = 0.0336 \pm 0.0001\,\text{s}; \qquad \tau^{ex}_{anti} = \frac{1}{\kappa\Lambda_2} = 0.0578 \pm 0.0006\,\text{s},$$

with the superscripts on τ simply indicating that these are experimental values and are not to be confused with the values given for simulations above. After the 4 s relaxation period, trap 2 is moved in reverse along the arc at the same velocity to return it to its initial position. After a further relaxation period, the cyclical process is repeated. An example of particle trajectories from the anti-clockwise and subsequent clockwise rotation of trap 2 can be seen in figure 8.6. The spread of points at the end of each rotation illustrates how particle 2 is able to relax during the time between trap rotations. From five videos each containing ten cyclical trap translations I am able to extract 100 individual trajectories.

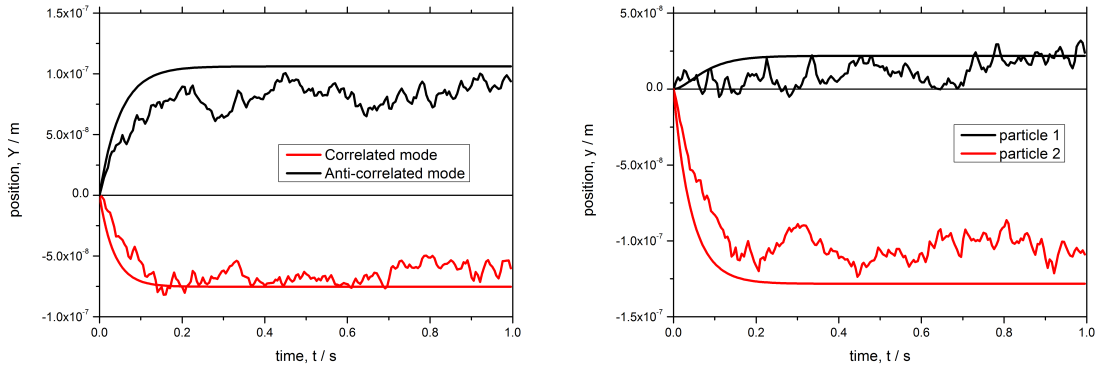

(a) Average mode trajectories **(b)** Average particle trajectories

Figure 8.7: **(a)** Ensemble average of the mode trajectories, with expected line given by equation (3.19). **(b)** Ensemble average of particle positions in rotating reference frame.

The fluid velocity (at particle 2 in the rotating frame) is large in comparison with the simulations. An advantage of a larger fluid velocity is that displacement of the particles from their initial equilibrium will be larger, meaning that for a relatively small number of trajectories the mode trajectories are more likely to stand out against the thermal noise when the ensemble average is taken. This will be useful in these preliminary experiments, where I will need to assess whether the mode trajectories are behaving as I predict. A disadvantage is that the rate at which work is applied to the modes is larger and subsequently the work distributions will move more quickly to positive mean values, meaning that the number of samples (e.g. video frames) within the transient portion of the trajectory is reduced. This is significant, bearing in mind that the camera is already operating at the limit of its frame rate.

Since the conversion factors that allow the voltage applied to the mirror drivers to be converted to a trap position are known, I could calculate the trap position in each frame of the video. Equipped with the particle and mirror positions, it was possible to convert the particle positions to the rotating frame (given the angle of trap 2, which is easily derived from position) and to calculate the correlated and anti-correlated modes.

Figures 8.7a and 8.7b show the ensemble average of the mode and particle tra-

jectories from the 100 individual trajectories. The trajectories from the clockwise rotations of trap 2 have been reversed so that the clockwise and anti-clockwise trajectories can be averaged together. Also shown are the expected trajectories given by equation (3.19). There is broad agreement between the measured mode and particle trajectories and the expected trajectories. However, it is noticeable than the rates at which the modes and particles are displaced are slower and the final displacements are smaller than expected. Various explanations can be proposed for this divergence from the predicted behaviour. It may be the case that, with only 100 trajectories in the ensemble average, the signal-to-noise ratio is small enough that the apparent behaviour of the system is skewed by the noise. This could be remedied by simply recording more trajectories. It may also be the case that there are inaccuracies in the conversion factors for the mirror-voltage to position coordinates, meaning that my assumed knowledge of the trap positions is incorrect. This would skew the data for the position of the particles relative to the trap centres. A flaw in my knowledge of the relative trap positions may also mean that the alignment of the arc on the centre of trap 1 is awry. A small misalignment of the position of trap 2 could result in a path that does not maintain a fixed distance from trap 1, which would affect the assumed angle of trap 2, θ.

Despite the trajectories of the modes not appearing quite as anticipated, I proceeded to calculate the work applied to each mode along every trajectory, using the method described above for the simulated data. Work distributions for both modes at times $t = 0.025\,\mathrm{s}$ and $t = 0.1\,\mathrm{s}$ are shown in figure 8.8. The agreement between the histograms and the predicted probability distributions is good, although figure 8.8b does illustrate the fact that with a limited number of trajectories a few outliers are liable to skew the distribution. As we saw in the distributions for the simulated work, these distributions broaden and the mean value moves in the positive direction with time. The probability of observing a negative work diminishes as time proceeds.

I have not included plots to illustrate the detailed fluctuation theorem (DFT) as I did for the simulated data in figures 8.2 and 8.3. With few points in each histogram bin, the value of the ratio $P(-W_i)/P(W_i)$ at each bin position is susceptible to

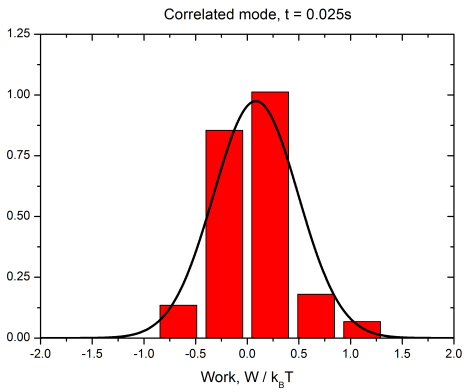

(a) Correlated mode, t = 0.025 s

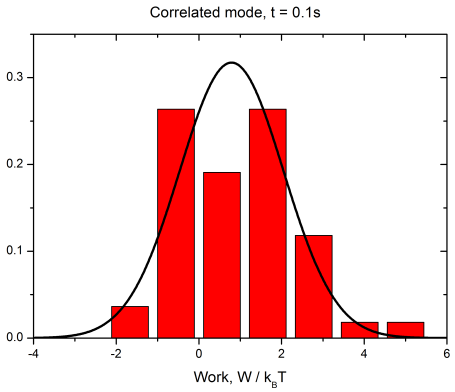

(b) Correlated mode, t = 0.1 s

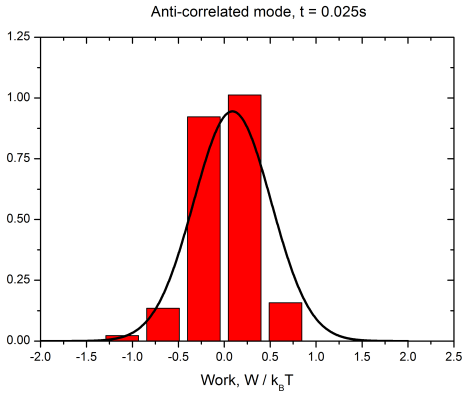

(c) Anti-correlated mode, t = 0.025 s

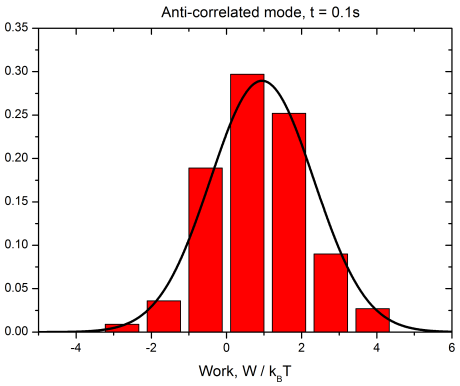

(d) Anti-correlated mode, t = 0.1 s

Figure 8.8: Experimental work distributions. Figures **(a)** and **(b)** show histograms of the work on the correlated mode from the experiment at times $t = 0.025\,\mathrm{s}$ and $t = 0.1\,\mathrm{s}$ respectively. Also shown are the probability distributions predicted by equation (7.44). Figures **(c)** and **(d)** are the corresponding plots for the anti-correlated mode.

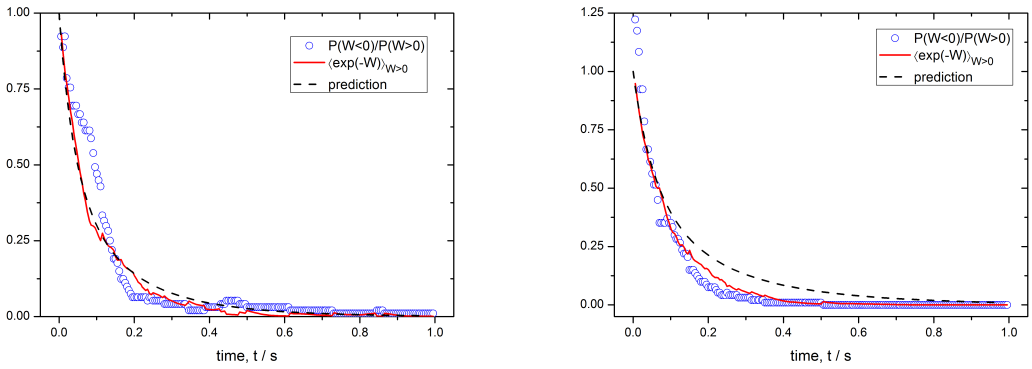

(a) Correlated mode **(b)** Anti-correlated mode

Figure 8.9: Integrated Fluctuation theorem (IFT) for the modes. In figures **(a)** and **(b)**, blue circles represent the left-hand side of equation (7.47), the ratio of positive to negative work values, whilst the red line represents the right-hand side, the mean of the negative exponential for the positive work values. Perfect alignment of the blue dots and red line would indicate perfect satisfaction of the IFT. The dashed black line is the prediction given by equation (7.50).

large deviation from the expected value of $\exp(-W_i/k_BT)$. Subsequently it is not possible to observe agreement between the left- and right-hand sides of the DFT for this data.

Figure 8.9 illustrates that the work on the modes does, to a reasonable extent, satisfy the integrated fluctuation theorem (IFT). The method for producing such plots was outlined in section 8.1.3. Also shown are the predictions of equation 7.50. The agreement with theory for the correlated mode is quite good, although agreement is less clear for the anti-correlated mode. This can be linked to the plots in figure 8.7a. The correlated mode follows the expected trajectory much more closely than the anti-correlated mode. The slower rate of displacement of the anti-correlated mode results in a slower rate of work and subsequently a faster decay in the IFT than is expected, which is what can be seen in figure 8.9b.

Despite these slight discrepancies, the figures shown above are encouraging. With a limited number of trajectories, we can see the trends in the data that we expect from theory and the simulated data. In the following section I will summarise the work presented here and suggest some improvements to the experimental set-up.

8.3 Summary of part IV

In summary, I have presented an investigation into the applicability of fluctuation theorems (FTs) to a system of hydrodynamically coupled colloidal particles.

FTs describe the ratio of the probability of observing positive to negative work values in a system where thermal fluctuations are of a comparable size to the work applied to that system. In such systems the work, heat and entropy do not have exact values. Rather, these quantities are described by probability distributions. FTs describe the asymmetry of these distributions as they evolve in time.

FTs have been shown, experimentally, to apply to many difference systems [**?**, **?**]. An influential early experiment demonstrated how the work applied to a particle when dragged through its viscous environment by an optical tweezers is described by a FT [28]. Here, I have investigated the applicability of a FT to a system of two particles that are hydrodynamically coupled.

I have described a model in which two particles are held in close proximity by a pair of optical tweezers. Work is applied directly to one of the particles by moving its trap slowly in an arc around the other stationary particle. The motion of the first particle induces a flow of fluid that displaces the particle in the stationary trap. In order to assess the work applied to the system, I decouple the particle's equations of motion into their associated normal modes. Each mode obeys an uncoupled Langevin equation, to which we can apply stochastic thermodynamic principals in order to calculate the work applied to the modes over a trajectory.

I then used finite-difference simulations to show that the distribution of work applied to each mode is described accurately by a detailed FT as well as integrated version of the FT. Due to the different relaxation times of the two modes, the rate of work is different for the two modes and the IFTs subsequently evolve at different rates. Furthermore, I have shown experimentally that the work applied to the modes obeys the integrated FT, although the data is insufficient to show that the work also obeys the detailed FT.

8.3.1 Future work

Future work on this project should aim to identify the cause of the discrepancy between the expected trajectories and those produced by the experiment. Greater care may be needed in the calculation of the calibration factor between the voltage applied to the mirror drivers and the spatial configuration of the traps. As was mentioned above, it may also be the case that an ensemble made up of a larger number of trajectories would show closer agreement with the expected trajectories.

Improvements to the experimental set-up could also be made. Figure 8.10 shows a proposed modification. The set-up is similar to that described above, and shown in figure 6.1, but added to the set up is a pair of quadrant photodiodes (QPDs). Light scattered by trapped particles is collected by the pair of QPDs, allowing tracking of the particles in each trap. QPDs would allow a greater temporal resolution in measuring the positions of the particles. This is important because I am interested in assessing the work applied to the modes of the system during the transient part of their trajectories - the TFT is applicable during the initial transient and latter stationary sections of a trajectory. The maximum sampling frequency achievable with the digital camera is $\sim$ 200Hz, which is of a similar order to the relaxation frequency of the modes. It will be useful to sample the trajectory frequently during its transient duration, i.e. while $t < \tau$.

Furthermore, the signals from the QPDs can straightforwardly be converted to a spatial coordinate. When compared to video capture and the subsequent video analysis, the use of QPDs would have the significant advantage of being less time consuming and computationally-demanding.

In figure 8.10, the tracking laser is scattered by particles in each trap and the scattered light is collected by the condenser. A dichroic mirror rejects the illumination light and transmits the scattered trapping light. The light scattered by particles in the two traps are separated by another PBS and the two subsequent beams are focussed onto individual QPDs.

This set-up was installed in the lab but due to an unidentified source of noise on the QPD signals, I was unable to make the set-up operational under the time constraints of this project.

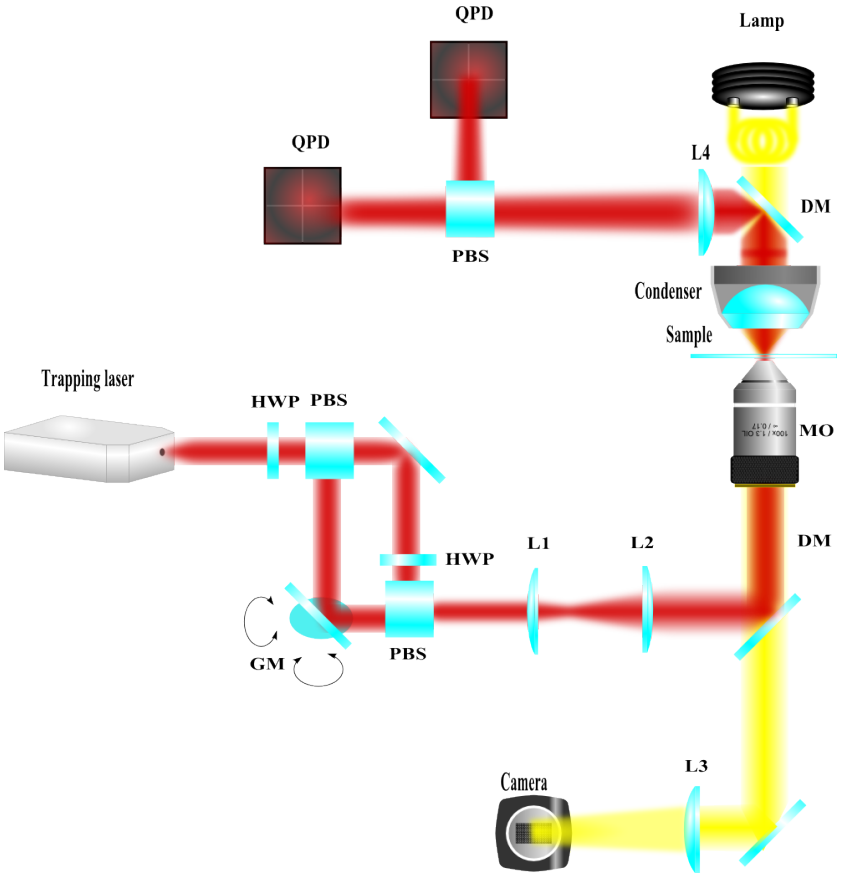

Figure 8.10: Proposed experimental set-up for high sampling-frequency measurement of mode trajectories. The light scattered by particles in the two traps are collected by a condenser lens and the beams are separated by a polarising beam splitter (PBS). The subsequent beams are directed onto one of two quadrant photo diodes (QPD). (Key: HWP - half wave plate; PBS - polarising beam splitter; L - lens; MO - microscope objective; QPD - quadrant photodiode)

Beyond the work on two particle systems, one could test the ideas presented here in systems of increasing complexity. An obvious next step would be to add a third trapped particle to the system. This would also allow an added degree of configurational complexity. One could also introduce additional coupling forces such as magnetic or electrostatic fields.

Part V

Conclusions

Chapter 9

Conclusions

In this thesis I have pesented research on three topics related to the dynamics of microscopic systems: the dynamical stabilisation of a microscopic pendulum that is finitely rigid and subject to strong damping; the deformability of red bllod cells from patients suffering from diabetic retinopathy; and the thermal fluctuations of a hydrodynamically coupled system of colloidal particles. The three strands of research are further linked by the common application of optical tweezers as an investigatory tool.

The thesis is split into five parts. Part I contains a brief historical overview of the development of optical tweezers, an introduction to the forces that underlie the operation of optical tweezers, the typical apparatus used in an optical tweezers experiment, and an overview of the particle dynamics concepts that are referred to later in the thesis.

Part II contains the work on dynamical stabilisation. Dynamical stabilisation refers to the introduction of stability into an unstable system by the application of an oscillatory force. The archetype of dynamical stabilisation is the inverted pendulum, also known as the Kapitza pendulum after the man who developed an analytical model of the pendulum. The Kapitza pendulum is a simple rigid pendulum whose suspension point is vertically oscillated in such a way as to induce stability in the inverted position. The physical reason for this inverted stability was outlined in section 4.2; it was shown that at an acute angle to the upright position, while the force averaged over a cycle of the driving oscillation is zero, the net torque

acts towards the upright position. The work presented here goes beyond the usual assumptions of a typical Kapitza pendulum by explicitly considering the rigidity of the pendulum and damping due to the pendulum's environment. A model is presented based on a colloidal particle that is trapped at the circumference of a ring shaped optical potential. Fluid flow across the ring drives the particle in the direction of flow, towards the 'bottom' of the ring. The centre of the ring is then oscillated sinusoidally in the direction of the fluid flow. It is found theoretically that in this regime the pendulum will explore a range of induced stability positions. Within this regime there are at least two sub-regimes. If the frequency of the oscillation is much larger than the relaxation frequency of the particle in the potential, the stability position of the particle is dependent on the driving amplitude but independent of the driving frequency. If, however, the driving frequency is smaller than the particle relaxation frequency the stability position will be dependent on both the driving amplitude *and* frequency. These theoretical predictions are tested with the simulations and experiments in chapter 5. Very good agreement is found between theory and experiment.

Part III contains the work on deformability of red blood cells (RBCs) in patients with diabetic retinopathy (DR). DR is a common side effect of diabetes mellitus (DM). It is a disease of the eye that is caused by hyperglycaemic damage to the microvascular system of the retina. The effects of DR can lead to a leakage of blood into the retina, which can obscure vision. Eventually, the deleterious effects of DR can lead to retinal detachment and blindness. It has been established that DM leads to an impairment in the deformability of RBCs and this has been linked to problems in the microvascular system of the kidney. However, it remains unclear if there is a link between reduced deformability of RBCs and DR. In this part of the thesis I aimed to investigate this link by using optical tweezers to measure the deformability of RBCs from patients with and without DR. I first present the experimental set-up and explain how optical tweezers are used to measure RBC deformability. In short, RBCs are trapped between two optical tweezers that are separated in x by 5.1 µm. The RBC assumes a side-on orientation in the traps. One of the traps, that is steerable via a pair of computer-positioned galvanomter mirrors, is moved slowly

away from the stationary trap, thus elongating the RBC. The RBC is allowed to relax back to its initial length before the process is repeated. For each such process a 'deformability index' is calculated, which is a normalised subtraction of the intial length from the maximum length of the RBC. In section 6.9.1 I present the measured deformabilty indices from 8 healthy patients and 7 patients with DR. A statistically significant reduction in the deformability of RBCs from patients with DR is found. The data presented here is from a small sample and significant additional data is required before a link between DR and reduced RBC deformability can be claimed. However, this work does represent promising progress in the use of optical tweezers as a tool for investigating the deformability of RBCs.

Finally, part IV contains the work on thermal fluctuations in a hydrodynamically coupled system. Thermal fluctuations begin to have a material effect on the thermodynamics of a sytem when the heat and work associated with that system are of a comparable energy to the thermal fluctuations in the system. For this to be the case, we must consider a small sytem over a short period of time. Classical thermodynamics, however, is not applicable to such a case. Classical thermodynamics holds in the case of large systems over long periods of time. Therefore, a new formulation is required to describe the transfer of energy in a small system that is influenced by thermal fluctuations. In recent decades, as interest in systems that operate on the micro-scale has grown, a new framework has emerged in which thermodynamic quantities such as work and heat are treated as probability distributions, rather than exact values. With this framework rules have been derived to describe the evolution of these distributions. One such rule is the fluctuation theorem (FT), which describes the shape of the probability distribution for thermodynamic quantities as time evolves. A seminal paper in this emerging field experimentally proved the validity of the FT by measuring the work applied to a colloidal particle as it was dragged through an aqueous environment by an optical tweezers. The authors showed that the work applied to the particle obeyed the predictions of the FT [28]. In the work presented here, I have carried out an investigation into the applicability of the fluctuation theorem to a system of coupled colloidal particles. The model presented consists of two particles that are held in individual optical tweezers and

whose motion is coupled by their aqueous environment. Work is applied to the system by moving one of the traps in an arc about the centre of the other trap; work is directly applied to the particle in the moving trap whereas work is applied to the particle in the stationary trap via the particle coupling. In order to assess the work applied to the system, the equations of motion for the two particles are de-coupled into their normal modes. The normal modes obey simple Langevin equations and it is a quite straightforward calculation to find the work applied along a trajectory. I have presented results from simulations and experiments. The simulations show that the work on the modes satisfies a detailed fluctuation theorem (DFT) as well as an integrated fluctuation theorem (IFT). Experimentally, I had insufficient data to prove that the work satisfied the DFT but could demonstrate satisfaction of the IFT.

Taken as a whole, the work presented in this thesis illustrates the wide scope of application for optical tweezers in scientific research. The great strength of optical tweezers as a research tool lies in their ability to accurately manipulate and probe microscopic systems. I have made repeated use of that ability in this work to study the dynamics of three distinct systems and each system has yielded richly interesting results.

Bibliography

[1] J. C. Meiners and S. R. Quake. Direct measurement of hydrodynamic cross correlations between two particles in an external potential. *Physical Review Letters*, 82(10):2211–2214, 1999.

[2] J. C. Maxwell. *Treatise on Electricty and Magnetism*, volume 2. Clarendon Press, Oxford, 1873.

[3] P. Lebedev. Experimental examination of light pressure. *Annalen der Pysik*, 6:433–458, 1901.

[4] A. Ashkin. Acceleration and trapping of particles by radiation pressure. *Physical Review Letters*, 24(4):156–159, 1970.

[5] A. Ashkin and J. Dziedzic. Optical levitation by radiation pressure. *Applied Physics Letters*, 19(8):283–285, 1971.

[6] A. Ashkin, J. Dziedzic, J. Bjorkholm, and S. Chu. Observation of a single-beam gradient force optical trap for dielectric particles. *Optics Letters*, 11(5):288–290, 1986.

[7] P. H. Jones, O. M. Marago, and G. Volpe. *Optical Tweezers: Principles & Applications*. Cambridge University Press, 2015.

[8] A. Ashkin, J. M. Dziedzic, and T. Yamane. Optical trapping and manipulation of single cells using infrared laser beams. *Nature*, 330(6150):769–771, 1987.

[9] K. C. Neuman, E. H. Chadd, G. F. Liou, K. Bergman, and S. M. Block. Characterization of photodamage to escherichia coli in optical traps. *Biophysical Journal*, 77(5):2856–2863, 1999.

[10] A. Ashkin and J. M. Dziedzic. Optical trapping and manipulation of viruses and bacteria. *Science*, 235:1517–1520, 1987.

[11] K. Svoboda, C. F. Schmidt, B. J. Schnapp, and S. M. Block. Direct observation of kinesin stepping by optical trapping interferometry. *Nature*, 365(6448):721–727, 1993.

[12] J. T. Finer, R. M. Simmons, and J. A. Spudich. Single myosin molecule mechanics: Piconewton forces and nanometre steps. *Nature*, 368(6467):113–119, 1994.

[13] J. E. Molloy, J. E. Burns, J. Kendrick-Jones, R. T. Tregear, and D. C. S. White. Movement and force produced by a single myosin head. *Nature*, 378(6553):209–212, 1995.

[14] M.D. Wang, H. Yin, R. Landick, J. Gelles, and S.M. Block. Stretching dna with optical tweezers. *Biophysical Journal*, 72(3):1335–1346, 1997.

[15] M. D. Wang, M. J. Schnitzer, H. Yin, R. Landick, J. Gelles, and S. M. Block. Force and velocity measured for single molecules of rna polymerase. *Science*, 282(5390):902–907, 1998.

[16] G. Jiang, G. Giannone, D. R. Critchley, E. Fukumoto, and M. P. Sheetz. Two-piconewton slip bond between fibronectin and the cytoskeleton depends on talin. *Nature*, 424(6946):334–337, 2003.

[17] D. G. Grier and Y. Roichman. Holographic optical trapping. *Applied Optics*, 45(5):880–887, 2006.

[18] K. Dholakia and T. Cizmar. Shaping the future of manipulation. *Nature Photonics*, 5(6):335–342, 2011.

[19] A. Curran, M. P. Lee, M. J. Padgett, J. M. Cooper, and R. Di Leonardo. Partial synchronization of stochastic oscillators through hydrodynamic coupling. *Physical Review Letters*, 108(24):240601–1 – 240601–4, 2012.

[20] M. Polin, D. G. Grier, and S. R. Quake. Anomalous vibrational dispersion in holographically trapped colloidal arrays. *Physical Review Letters*, 96(8):088101–1, 2006.

[21] R. Di Leonardo, S. Keen, J. Leach, C. D. Saunter, G. D. Love, G. Ruocco, and M. J. Padgett. Eigenmodes of a hydrodynamically coupled micron-sized multiple-particle ring. *Physical Review E*, 76(6):061402–1, 2007.

[22] M. Padgett and R. Bowman. Tweezers with a twist. *Nature Photonics*, 5(6):343–348, 2011.

[23] H. He, M. Friese, N. R. Heckenberg, and H. Rubinsztein-Dunlop. Direct observation of transfer of angular momentum to absorptive particles from a laser beam with a phase singularity. *Physical Review Letters*, 75(5):826–829, 1995.

[24] L. I. McCann, M. Dykman, and B. Golding. Thermally activated transitions in a bistable three-dimensional optical trap. *Nature*, 402(6763):785–787, 1999.

[25] H. A. Kramer. Brownian motion in a field of force and the diffusion model of chemical reactions. *Physica*, 7(4):284–304, 1940.

[26] A. Berut, A. Arakelyan, A. Petrosyan, S. Ciliberto, R. Dillenschneider, and E. Lutz. Experimental verification of landauers principle linking information and thermodynamics. *Nature*, 483(7388):187–189, 2012.

[27] R. Landauer. Irreversibility and heat generation in the computing process. *IBM J. Res. Dev.*, 5(3):183–191, 1961.

[28] G. M. Wang, E. M. Sevick, E. Mitagtag, D. J. Searles, and D. J. Evans. Experimental demonstration of violations of the second law of thermodynamics for small systems and short time scales. *Physical Review L*, 89(5):010601–1, 2002.

[29] D. J. Evans and D. J. Searles. The fluctuation theorem. *Advances in Physics*, 51(7):1529–1585, 2002.

[30] P. H. Jones. *Optical Tweezers*. Taylor & Francis, 2013.

[31] B. T. Draine and P. J. Flatau. Discrete-dipole approximation for scattering calculations. *Journal of the Optic*, 11(4):1491–1499, 1994.

[32] S. Albaladejo, M. I. Marques, M. Laroche, and J. J. Saenz. Scattering forces from the curl of the spin angular momentum of a light field. *Physical Review Letters*, 102(11):113602–1 – 113602–4, 2009.

[33] R. Bowman and M. Padgett. Optical trapping and binding. *Reports on progress in physics*, 76(2), 2013.

[34] R. Brown. A brief account of microscopical observations made in the months of june, july and august, 1827, on the particles contained in the pollen of plants; and on the general existence of active molecules on organicc and inorfanic bodies. *Phil. Mag*, 4:161–173, 1828.

[35] D. S. Lemons and A. Gythiel. Paul langevins 1908 paper on the theory of brownian motion. *American Journal of Physics*, 65:1079, 1997.

[36] N. G. van Kampen. *Stochastic Process in Physics and Chemistry*. Elsevier, 2007.

[37] M. Doi and S. F. Edwards. *The Theory of Polymer Dynamics*. Oxford University Press, 1988.

[38] K. F. Riley, M. P. Hobson, and S. J. Bence. *Mathematical Methods for Physics and Engineering*. Cambridge University Press, 1998.

[39] Y. Roichman, B. Sun, A. Stolarski, and D. Grier. Influence of nonconservative optical forces on the dynamics of optically trapped colloidal spheres: The fountain of probability. *Physical Review Letters*, 101:128301–1 – 128301–4, 2008.

[40] F. Merenda, G. Boer, J. Rohner, G. Delacretaz, and R.-P. Salathe. Escape trajectories of single-beam optically trapped micro-particles in a transverse fluid flow. *Optics E*, 14(4):1685–1699, 2006.

[41] G. Pesce, G. Volpe, A. C. De Luca, G. Rusciano, and G. Volpe. Quantitative assessmanet of non-conservative radiation forces in an optical trap. *Europhysics Letters*, 86:38002–1 – 38002–6, 2009.

[42] S. J. Blundell and K. M. Blundell. *Concepts in Thermal Physics*. Oxford University Press, 2009.

[43] C. Pozrikidis. *Boundary Integral and Singularity Methods for Linearized Viscous Flow*. Cambridge University Press, 1992.

[44] J. Dhont. *An Introduction to Dynamics of Colloids (Studies in Interface Science)*. Elsevier Science, Amsterdam, 1996.

[45] G. M. Cicuta, E. Onofri, M. C. Lagomarsino, and P. Cicuta. Patterns of synchronizationin the hydrodynamic coupling of active colloids. *Physical Review E*, 85(1):016203–1, 2012.

[46] P. Bartlett, S. I. Henderson, and S. J. Mitchell. Measurement of the hydrodynamic fforce between two polmer-coated spheres. *Philosophical Transactions of the Royal Society A: Mathematical, Physical and Engineering Sciences*, 359(1782):883–895, 2001.

[47] G. Volpe and G. Volpe. Simulation of a brownian particle in an optical trap. *American Journal of Physics*, 81(3):224–230, 2012.

[48] *https://uk.mathworks.com/help/matlab/ref/randn.html*, September 2017.

[49] P. L. Kapitza. Dynamic stability of the pendulum with vibrating suspension point. *Soviet Physics, Journal of Experimental and Theoretical Physics*, 21(5):588–597, 1951. (in Russian).

[50] D. E. McMillan, N. G. Utterback, and J. La Puma. Reduced erythrocyte deformability in diabetes. *Diabetes*, 27(9):895–901, 1978.

[51] C. D. Brown, H. S. Ghali, Z. Zhao, L. L. Thomas, and E. A. Friedman. Association of reduced red blood cell deformability and diabetic nephropathy. *Kidney International*, 67(1):295–300, 2005.

[52] D. J. Evans and D. J. Searles. Equilibrium microstates which generate second law violating steady states. *Physical Review E*, 50(2):1645–1648, 1994.

Appendices

Appendix A

Equations of motion for a pendulum in polar coordinates

What follows is a Lagrangian derivation of the equations of motion for the pendulum described in part II in polar co-ordinates.

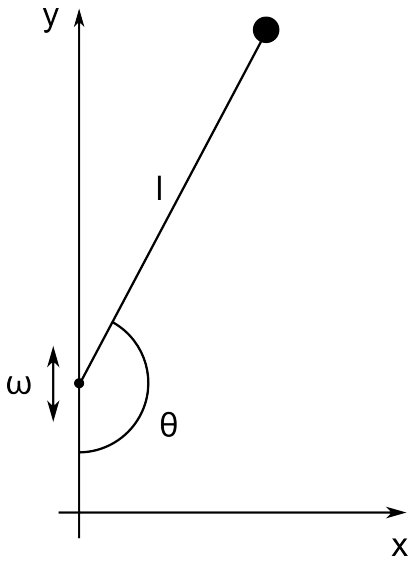

Figure A.1: Pendulum of mass m with equilibrium length l. The 'rod' is light and has a finite rigidity. The pivot point is subjected to a harmonic oscillation with frequency ω in the vertical direction.

Let us assume a pendulum of mass m with an equilibrium length l. The suspension point is subjected to a vertical oscillation with amplitude a and frequency ω that we will denote $y_s(t) = -a\cos(\omega t)$. We can describe the system as having two degrees of freedom: a radial co-ordinate $r(t)$ that changes with time since the

'rod' of the pendulum is not infinitely rigid; and an angular co-ordinate $\theta(t)$ that is measured from the downward position. We use a quartic potential to describe the radial potential of the pendulum,

$$V(r) = -\frac{V_0 r^2}{l^4}(r^2 - 2l^2), \tag{A.1}$$

as it is has a simple form that captures the important physics of a mathematical pendulum. We can form equations of motion for both co-ordinates from Lagrange's equation:

$$\frac{d}{dt}\frac{\partial L}{\partial \dot{q}_i} - \frac{\partial L}{\partial q_i} = Q_i, \tag{A.2}$$

where $q = (q_1, ..., q_n)$ are generalised co-ordinates, L is the Lagrangian defined as

$$L = K - U, \tag{A.3}$$

where K is the kinetic energy of the system and U is the potential energy, and Q_i represents any forces not arising from a potential. In our system, the force not arising from a potential is the force due to friction, in which case Q_i can be defined as

$$Q_i = -\frac{\partial \mathcal{F}}{\partial \dot{q}_i}, \tag{A.4}$$

where $\mathcal{F}$ is *Rayleigh's dissipation function*,

$$\mathcal{F} = \frac{\gamma}{2}(\dot{x}_i^2 + \dot{y}_i^2), \tag{A.5}$$

and γ is the friction coefficient. In terms of the horizontal and vertical positions of the pendulum $x(t)$ and $y(t)$, $\theta(t)$ and $r(t)$ are defined as

$$\begin{aligned} x(t) &= r(t)\sin[\theta(t)], \\ y(t) &= r(t)\cos[\theta(t)] - y_s(t). \end{aligned} \tag{A.6}$$

The kinetic and potential energies are given by $K = \frac{1}{2}m(\dot{x}^2 + \dot{y}^2)$ and $U = V - Fy$, where F is a constant force (e.g. gravity in the conventional inverted pendulum or

the force due to fluid flow in our system). Hence, the kinetic energy is

$$K = \frac{1}{2}m\left[r^2\dot{\theta}^2 + \dot{r}^2 + 2r\dot{\theta}\dot{y}_s\sin\theta - 2\dot{r}\dot{y}_s\cos\theta + \ddot{y}_s\right], \tag{A.7}$$

the potential energy is

$$U = \frac{V_0 r^2}{l^4}(r^2 - 2l^2) - F(r\cos\theta - y_s), \tag{A.8}$$

and the Lagrangian is

$$L = \frac{1}{2}mr^2\dot{\theta}^2 + \frac{1}{2}m\dot{r}^2 + mr\dot{\theta}\dot{y}_s\sin\theta - m\dot{r}\dot{y}_s\cos\theta + \frac{1}{2}m\ddot{y}_s - \frac{V_0 r^2}{l^4}(r^2 - 2l^2) + Fr\cos\theta - Fy_s. \tag{A.9}$$

A.1 Angular equation of motion

The differential terms in Lagrange's equation, equation (A.2), with respect to coordinate $\theta(t)$, are as follows:

$$\frac{\partial L}{\partial\theta} = mr\dot{\theta}\dot{y}_s\cos\theta + m\dot{r}\dot{y}_s\sin\theta - Fr\sin\theta; \tag{A.10}$$

$$\frac{\partial L}{\partial\dot{\theta}} = mr^2\dot{\theta} + mr\dot{y}_s\sin\theta; \tag{A.11}$$

$$\frac{d}{dt}\frac{\partial L}{\partial\dot{\theta}} = 2mr\dot{r}\dot{\theta} + mr^2\ddot{\theta} + m\dot{r}\dot{y}_s\sin\theta + mr\ddot{y}_s\sin\theta + mr\dot{\theta}\dot{y}_s\cos\theta. \tag{A.12}$$

The dissipative force Q_i term, with respect to $\theta(t)$, is

$$\begin{aligned} Q_i &= -\frac{\gamma}{2}\frac{\partial}{\partial\dot{\theta}}(\dot{x}_i^2 + \dot{y}_i^2) \\ &= -\gamma(r^2\dot{\theta} + r\dot{y}_s\sin\theta). \end{aligned} \tag{A.13}$$

The Lagrange equation corresponding to $\theta(t)$ is, therefore,

$$mr^2\ddot{\theta} + 2mr\dot{r}\dot{\theta} + mr\ddot{y}_s\sin\theta + Fr\sin\theta = -\gamma(r^2\dot{\theta} + r\dot{y}_s\sin\theta). \tag{A.14}$$

A.2 Radial equation of motion

The differential terms in Lagrange's equation, equation (A.2), with respect to coordinate $r(t)$, are as follows:

$$\frac{\partial L}{\partial r} = mr\dot{\theta}^2 + m\dot{\theta}\dot{y}_s \sin\theta + F\cos\theta + \frac{4V_0 r}{l^4}(r^2 - l^2); \tag{A.15}$$

$$\frac{\partial L}{\partial \dot{r}} = m\dot{r} - m\dot{y}_s \cos\theta; \tag{A.16}$$

$$\frac{d}{dt}\frac{\partial L}{\partial \dot{r}} = m\ddot{r} - m\ddot{y}_s \cos\theta + m\dot{y}_s\dot{\theta}\sin\theta. \tag{A.17}$$

The dissipative force Q_i term, with respect to $r(t)$, is

$$\begin{aligned} Q_i &= -\frac{\gamma}{2}\frac{\partial}{\partial \dot{r}}(\dot{x}_i^2 + \dot{y}_i^2) \\ &= -\gamma(\dot{r} + \dot{y}_s \cos\theta). \end{aligned} \tag{A.18}$$

The Lagrange equation corresponding to $r(t)$ is, therefore,

$$m\ddot{r} - m\ddot{y}_s\cos\theta - mr\dot{\theta}^2 - F\cos\theta + \frac{4V_0 r}{l^4}(r^2 - l^2) = -\gamma(\dot{r} + \dot{y}_s\cos\theta) \tag{A.19}$$

Appendix B

Solution to the radial equation of motion

The equation of motion for the radial coordinate, as given in equation (4.35), is

$$\ddot{r} + \gamma\dot{r} + \omega_0^2 r = \omega_0^2 L + r\dot{\theta}^2 + \frac{F}{m}\cos\theta + \ddot{y}_s \cos\theta + \gamma\dot{y}_s \cos\theta, \tag{B.1}$$

which, if $y_s = -a\cos(\omega t)$, is equivalent to

$$\ddot{r} + \gamma\dot{r} + \omega_0^2 r = \omega_0^2 L + r\dot{\theta}^2 + \frac{F}{m}\cos\theta + a\omega^2 \cos\theta\cos(\omega t) + a\gamma\omega\cos\theta\sin(\omega t). \tag{B.2}$$

If we assume that θ changes over a much longer timescale than r, we can make the approximation that θ is constant over the timescale in which r changes ($\dot{\theta} \to 0$). Equation (B.2) thus represents a driven harmonic oscillator.

The general solution to driven harmonic motion consists of two parts, a transient response and a driven response:

$$r(t) = r_t(t) + r_d(t). \tag{B.3}$$

The transient response, r_t, is given by the solution to the homogeneous part of the equation of motion e.g. $\ddot{r} + \gamma\dot{r} + \omega_0^2 r = 0$. Depending on the damping conditions, the transient response will either be an exponential decay towards equilibrium or an oscillation about equilibrium [**?**]. The driven response, r_d, persists beyond the

transient response and is given by the complimentary solution to the equation of motion. Here we will only concern ourselves with finding the driven response to equation (B.2); since the transient response quickly dies away, we can neglect this contribution without much loss of accuracy, $r(t) \approx r_d(t)$.

Let us begin by proposing a solution of the form

$$r_d(t) = A + B\cos(\omega t) + C\sin(\omega t), \tag{B.4}$$

where A, B, C are constants to be found. If we substitute (B.4) into (B.2) we find

$$\begin{aligned}\left\{-B\omega^2 + C\gamma\omega + B\omega_0^2\right\}\cos(\omega t) + \left\{-C\omega^2 - B\gamma\omega + C\omega_0^2\right\}\sin(\omega t) + \omega_0^2 A \\ = \omega_0^2 L + \frac{F}{m}\cos\theta + a\omega^2\cos\theta\cos(\omega t) + a\gamma\omega\cos\theta\sin(\omega t).\end{aligned} \tag{B.5}$$

By matching the coefficients of $\sin(\omega t)$ and $\cos(\omega t)$ we find:

$$-B\omega^2 + C\gamma\omega + B\omega_0^2 = a\omega^2\cos\theta; \tag{B.6}$$

$$-C\omega^2 - B\gamma\omega + C\omega_0^2 = a\gamma\omega\cos\theta; \tag{B.7}$$

$$A\omega_0^2 = \omega_0^2 L + \frac{F}{m}\cos\theta. \tag{B.8}$$

From equation (B.8) we have

$$A = L + \frac{F}{m\omega_0^2}\cos\theta. \tag{B.9}$$

Rearranging equations (B.6) and (B.7) for B and C respectively, we find

$$B = \frac{1}{\omega_0^2 - \omega^2}\left(a\omega^2\cos\theta - C\gamma\omega\right) \tag{B.10}$$

$$C = \frac{1}{\omega_0^2 - \omega^2}\left(a\gamma\omega\cos\theta + B\gamma\omega\right) \tag{B.11}$$

Substitution of (B.11) into (B.10) leads us to

$$B = \frac{a\omega^2\cos\theta(\omega_0^2 - \omega^2 - \gamma^2)}{(\omega_0^2 - \omega^2)^2 + \gamma^2\omega^2}. \tag{B.12}$$

And substitution of (B.10) into (B.11) leads us to

$$C = \frac{a\gamma\omega\omega_0^2 \cos\theta}{(\omega_0^2 - \omega^2)^2 + \gamma^2\omega^2}. \tag{B.13}$$

Inserting these values for coefficients A, B, C into our trial solution, equation (B.4), we have

$$\begin{aligned} r(t) = L &+ \frac{F}{m\omega_0^2}\cos\theta \\ &+ \frac{a\omega^2\cos\theta(\omega_0^2 - \omega^2 - \gamma^2)}{(\omega_0^2 - \omega^2)^2 + \gamma^2\omega^2}\cos(\omega t) \\ &+ \frac{a\gamma\omega\omega_0^2\cos\theta}{(\omega_0^2 - \omega^2)^2 + \gamma^2\omega^2}\sin(\omega t). \end{aligned} \tag{B.14}$$

In the limit $\omega_0 \to \infty$, the solution $r(t)$ can be approximated in the leading orders as

$$r_d(t) = L + \frac{a\omega^2\cos\theta\cos(\omega t)}{\omega_0^2} + \frac{a\gamma\omega\cos\theta\sin(\omega t)}{\omega_0^2}, \tag{B.15}$$

which is equivalent to

$$r_d(t) = L + \frac{\ddot{y}_s + \gamma\dot{y}_s}{\omega_0^2}\cos\theta. \tag{B.16}$$

Appendix C

Time averaging of equation (4.40)

In this appendix I show the steps involved in moving from equation (4.40) to equation (4.41) in section 4.4.2. Equation (4.40) is given by

$$\begin{aligned}\ddot{\psi} + \gamma_m \dot{\psi} = -\Omega^2 \sin\psi - \left(\gamma_m \frac{\dot{y}_s}{L} + \Omega^2 + \frac{\ddot{y}_s}{L}\right)\delta\cos\psi \\ - \left(\frac{\gamma_m}{\omega_0}\right)^2 \frac{\dot{y}_s}{L}(\dot{\psi} + \dot{\delta})(\cos\psi - \delta\sin\psi).\end{aligned} \tag{C.1}$$

The term y_s and its first two time derivatives are:

$$\begin{aligned} y_s &= -a\cos(\omega t); \\ \dot{y}_s &= a\omega\sin(\omega t); \\ \ddot{y}_s &= a\omega^2\cos(\omega t). \end{aligned}$$

The term δ and its first time derivative are:

$$\begin{aligned} \delta &= -\frac{y_s}{L}\sin\psi = \frac{a}{L}\cos(\omega t)\sin\psi; \\ \dot{\delta} &= -\frac{\dot{y}_s}{L}\sin\psi = -\frac{a\omega}{L}\sin(\omega t)\sin\psi. \end{aligned}$$

Substituting these terms into equation (C.1) gives

$$\ddot{\psi} + \gamma_m \dot{\psi} = -\Omega^2 \sin\psi - \left(\frac{\gamma_m a\omega}{L} \sin(\omega t) + \Omega^2 + \frac{a\omega^2}{L} \cos(\omega t) \right) \frac{a}{L} \cos(\omega t) \sin\psi \cos\psi$$
$$- \left(\frac{\gamma_m}{\omega_0} \right)^2 \frac{a\omega}{L} \sin(\omega t)(\dot{\psi} - \frac{a\omega}{L} \sin(\omega t) \sin\psi)(\cos\psi - \frac{a}{L} \cos(\omega t) \sin^2\psi). \tag{C.2}$$

Expanding the brackets in equation (C.2) and taking the time average $\langle \cdots \rangle$ over the period of the fast compnent δ gives

$$\begin{aligned} \ddot{\psi} + \gamma_m \dot{\psi} = & -\Omega^2 \sin\psi - \frac{\gamma_m a^2 \omega}{L^2} \sin\psi \cos\psi \langle \sin(\omega t) \cos(\omega t) \rangle \\ & - \frac{a\Omega^2}{L} \sin\psi \cos\psi \langle \cos(\omega t) \rangle - \frac{a^2\omega^2}{L^2} \sin\psi \cos\psi \langle \cos^2(\omega t) \rangle \\ & - \left(\frac{\gamma_m}{\omega_0} \right)^2 \left\{ \frac{a\omega}{L} \dot{\psi} \cos\psi \langle \sin(\omega t) \rangle - \frac{a^2\omega}{L^2} \dot{\psi} \sin^2\psi \langle \sin(\omega t) \cos(\omega t) \rangle \right. \\ & \left. - \frac{a^2\omega^2}{L^2} \sin\psi \cos\psi \langle \sin^2(\omega t) \rangle + \frac{a^3\omega^2}{L^3} \sin^3\psi \langle \sin^2(\omega t) \cos(\omega t) \rangle \right\}, \end{aligned} \tag{C.3}$$

bearing in mind that we are assuming that ψ is constant over the period in which δ changes. The following are the values of the terms within angular brackets in equation (C.3):

$$\langle \cos(\omega t) \rangle = 0; \qquad \langle \sin(\omega t) \rangle = 0; \tag{C.4}$$

$$\langle \cos^2(\omega t) \rangle = \frac{1}{2}; \qquad \langle \sin^2(\omega t) \rangle = \frac{1}{2}; \tag{C.5}$$

$$\langle \cos^2(\omega t) \sin(\omega t) \rangle = 0; \qquad \langle \sin(\omega t) \cos(\omega t) \rangle = 0. \tag{C.6}$$

Substituting these terms into equation (C.3), we find

$$\ddot{\psi} + \gamma_m \dot{\psi} = -\Omega^2 \sin\psi - \frac{a^2\omega^2}{2L^2} \sin\psi \cos\psi + \left(\frac{\gamma_m}{\omega_0} \right)^2 \frac{a^2\omega^2}{2L^2} \sin\psi \cos\psi. \tag{C.7}$$

Finally, making use of the identity $\frac{1}{2} \sin\psi \cos\psi = \sin 2\psi$, we have

$$\ddot{\psi} + \gamma_m \dot{\psi} = -\Omega^2 \sin\psi - \frac{a^2\omega^2}{4L^2} \sin 2\psi \left(1 - \frac{\gamma_m^2}{\omega_0^2} \right), \tag{C.8}$$

which is, as we set out to show, equation (4.40) in section 4.4.2.